Nonlinear Random Vibration of Planetary Gear Trains with Elastic Ring Gear

A Thesis for Doctoral Research in the Faculty of Engineering and Applied Science

by

Jalal Taheri Kahnamouei

Supervisory Committee

Geoff Rideout (Supervisor)

Stephen Butt

Sam Nakhla

Submitted to

The Ph.D. Comprehensive Examination Committee

Department of Engineering and Applied Science

Memorial University of Newfoundland

February 2021

St. John's Newfoundland

Abstract

Planetary gear trains (PGT) are widely used in the field of renewable energy, especially in wind turbines. A wind turbine uses planetary gearboxes to transfer wind torque to a generator, and even though gearboxes are designed according to sound engineering practices, they fail much sooner than their design life estimates. Unexpected PGT failures are costly, and it is vital to detect these failures early. This thesis proposes proper methods and analyses that help the wind turbine industry to prevent future failure by enlightening the nonlinear dynamic behavior of PGT under random force. This thesis will investigate one of the main factors in PGT failure: random vibration caused by wind turbulence. In this thesis, a hybrid dynamic model was proposed to model the stochastic nonlinear dynamics of a PGT with an elastic ring gear, and then the statistical linearization method (SL) was introduced to linearize the model. A new criterion of the SL is introduced to linearize the stochastic nonlinear dynamic model of a gear pair. The stochastic response of a thin-walled ring gear PGT under three equally-spaced random moving loads was also investigated. A series of parametric studies was conducted, and the obtained results revealed that the proposed model for the PGT accurately represented the dynamic behavior of the PGT with an elastic ring gear, and the SL gave acceptable accuracy. Also, the energy-based SL was enough accurate and valid to apply to stochastic nonlinear gear pairs under heavy load conditions, and the accuracy of the SL decreased for light load conditions. Finally, analysis on the effect of random moving loads on the ring gear

showed that the mean of displacement was affected by the critical speeds, and random loads' speed does not influence the standard deviation of displacement. Monte Carlo simulations (MCS) were conducted to verify the proposed model and method, and MCS proved the accuracy of the proposed model and process.

Letter of Transmittal

I, Jalal Taheri Kahnamouei, certify that my PhD thesis is prepared in accordance with the Faculty of Engineering and Applied Science guidelines for thesis and I am fully responsible for its contents.

I am ready to proceed to have my evaluated by my supervisory committee.

Jalal Taheri Kahnamouei

Acknowledgment

My sincere gratitude goes out to my Ph.D. supervisor, Dr. Geoff Rideout, for supporting and trusting me; His immense support guided me to finish this dissertation; I will forever be thankful to my former supervisor Dr. James Yang. I express gratitude to the members of my Ph.D. committee, Professors Stephen Butt, and Dr. Sam Nakhla for their helpful advice and suggestions.

Exceptional gratitude also goes out to Dr. Danine Farquharson and Dr. Faisal Khan for their encouragement and support. My sincere thanks go out to the Internationalization Office, especially Juanita Hennessey, for their unfailing support. I am also grateful to the following engineering department staff: Tina Dwyer, Colleen Mahoney, and Nicole Parisi for their support and assistance. My thanks go to Pesident's Doctoral Student Investment Fund (PDSIF) at Memorial University of Newfoundland and the Natural Sciences and Engineering Research Council (NSERC), Newfoundland and Labrador for financial support this Ph.D. research.

I gratefully acknowledge my parents, siblings, friends for all their love and encouragement. This dissertation would not have been possible without their warm love, continued patience, and endless support.

Thanks for all your encouragement!

Contents

List of Tables

List of Figures

Abbreviations

PGT	Planetary Gear Trains
SL	Statistical Linearization
CVT	Continuously Variable Transmission
FEM	Finite Element Model
LPM	Lumped Parameters Model
MCS	Monte Carlo Simulation
PDF	Probability Density Function
MW	Megawatt

Nomenclature

A_b	swept area of the rotor
B	white noise intensity matrix
b	backlash
b_{sp}	backlash between sun gear and planet gear
b_{rp}	backlash between ring gear and planet gear
$\bar{b}$	white noise intensity
C	damping matrix
C_p	power coefficient
c	damping
E	elasticity module
F	force
F_d	deterministic force vector
F_e	deterministic force vector of equalized force function
$F_r(t)$	radial component of moving load
$F_\tau(t)$	tangential component of moving load
F_{in}	internal meshing force vector
F_{ex}	represents the external force vector
f	nonlinear meshing force function

f_0	deterministic force part of equalized force function
f_e	equivalent linear force function
f_{sp}	nonlinear meshing force function between sun gear and planet gear
f_{rp}	nonlinear meshing force function between ring gear and planet gear
I	moment of inertia
K	stiffness matrix
K_s	bearings' stiffness matrix
K_e	equivalent stiffness matrix
k	stiffness
k_h	gear pair mesh stiffness
k_{sp}	mesh stiffness between sun gear and planet gear
k_s	sun bearing stiffness in transitional direction
k_{su}	sun bearing stiffness in rotational direction
k_c	carrier bearing stiffness in the transitional direction
k_p	planet bearing stiffness
k_{rp}	mesh stiffness between rp mesh
k_r	bolt radial stiffness
k_τ	bolt tangential stiffness
k_θ	bolt torsional stiffness
k_l	stiffness matrix of the l^{th} element of ring
k_e	equivalent stiffness

l	number of element
L	total number of elements
M	mass matrix
m	mass
m_l	mass matrix of the l^{th} element of ring
N	total number of planets
n	number of planet
P	potential energy
q_0	mean value of displacement vector of gear pair
$\hat{q}$	zero-mean displacement vector of gear pair
R_b	rotor radius
R_c	radius of the carrier
R_r	ring mean radius
R_s	base radius of the sun gear
r	gear pitch radius
rp	ring-planet gear pairs
sp	sun-planet gear pairs
T_{in}	input torque
T_{out}	output torque
t	time
t_r	ring thickness

U	generalized coordinate vector
u	displacement vectors at the point of the moving force
u_c	rotational displacement of carrier
u_s	rotational displacement of sun gear
u_n	rotational displacement of nth planet gear
$u_{l,r}$	radial displacement of node l at the contact point
$u_{l,\tau}$	tangential displacement of node l at the contact point
$u_{l,\theta}$	rotational displacement of node l at the contact point
V_0	mean wind velocity
V_t	turbulence wind velocity
$W(t)$	white noise
x_c	transverse displacement of carrier on x-axis
x_s	transverse displacement of sun gear on x-axis
y_c	transverse displacement of carrier on y-axis
y_s	transverse displacement of sun gear on y-axis
Δt	time interval
θ	angular coordinate
θ_l	angular coordination of node (l) of the element
μ	mean
σ	standard deviation
ρ	density of the ring material

ρ_a	air density
λ_0	tip speed ratio
ω_{r0}	rotation speed of the rotor
ψ_n	angle of the nth planet toward x axis
ω	meshing frequency
ω_c	constant angular velocity of moving load
δ	relative displacement
δ_{sp}	relative displacement between sun gear and planet gear
δ_{rp}	relative displacement between ring gear and planet gear
α	pressure angle
α_s	pressure angle of the sun gear
α_r	pressure angle of the planet gear
ξ_n	transverse displacements of nth planet gear on ξ-axis
η_n	transverse displacements of nth planet gear on η-axis
χ	displacement vector of filter

Chapter 1

Introduction

1.1 Background

The process of converting the kinetic energy of wind into other types of energy has been used by humankind for centuries. It is believed that the first windmills were designed 2000 years ago by Persia and China to grind corn [1, 2]. Over time wind energy has been harvested and used to make life easier for humankind, such as power boats across the ocean or pumping water throughout farmlands. In the 20th century, millions of small wind turbines had been installed in rural and remote areas to provide electricity. The need for greater energy resources has increased because of industrial development and the unstable cost of fossil fuels, and as a result, wind energy development has grown exponentially. In addition, wind power is a preferred source of renewable energy because of its sustainability, reliability, cleanness, cost-stability, and competitiveness in comparison to other energy sources.

Energy extraction from wind is considered one of the fastest growing sources of electricity in the world. For example, the total capacity of Canadian installed wind power grew from 444 MW in 2004 to 12,817 MW in 2018 (see Figure 1.1)[3]. This rapid

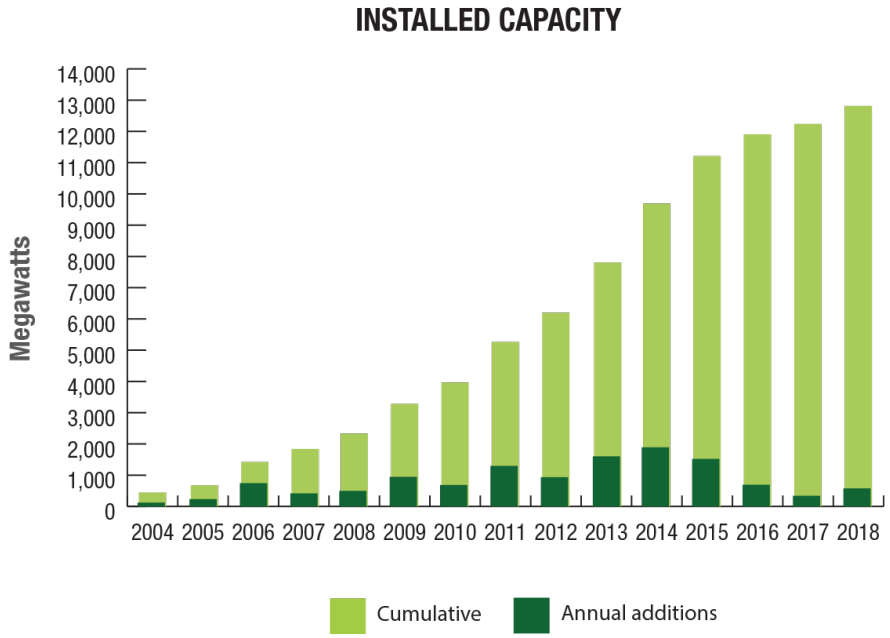

Figure 1.1: Installed Wind Power Capacity in Canada (in MW)[3]

development was because of the design and optimization of modern wind turbines.

Different types of wind turbines have been designed based on their capacity, environmental conditions, and remoteness. Among modern wind turbines, the design most commonly believed to be the most efficient is the horizontal axis wind turbine which has high efficiency and capacity for producing electricity at different wind speeds. The kinetic energy of the wind is transferred through the blades to the gearbox, and then from the gearbox to the generator, as shown in Figure 1.2 [4]. The generator creates electricity and transfers it to the consumer through a grid connection system. Because the wind turbine works at a low rotational speed, the primary purpose of the gearbox is to increase the low input rotational speed into a high output

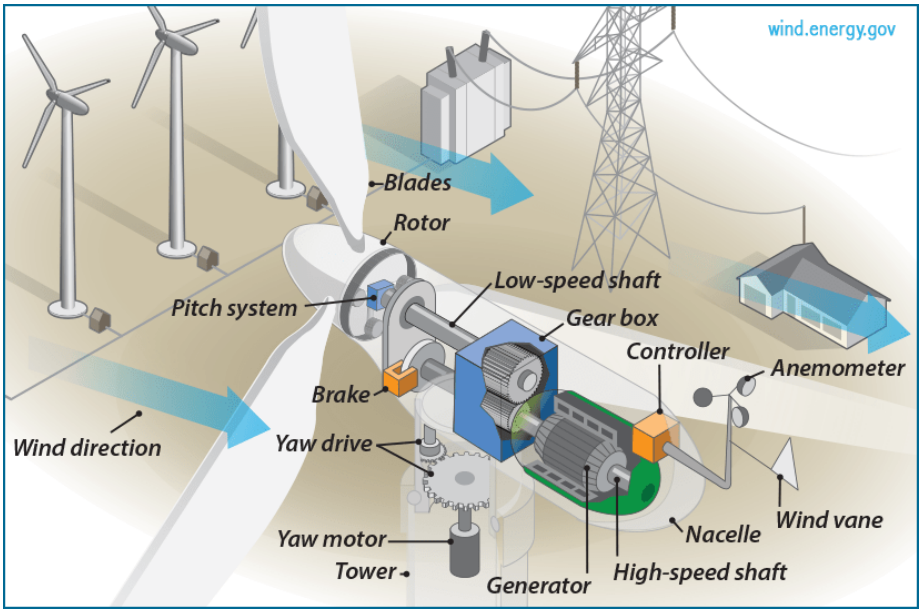

Figure 1.2: Wind turbine [4]

rotational speed.

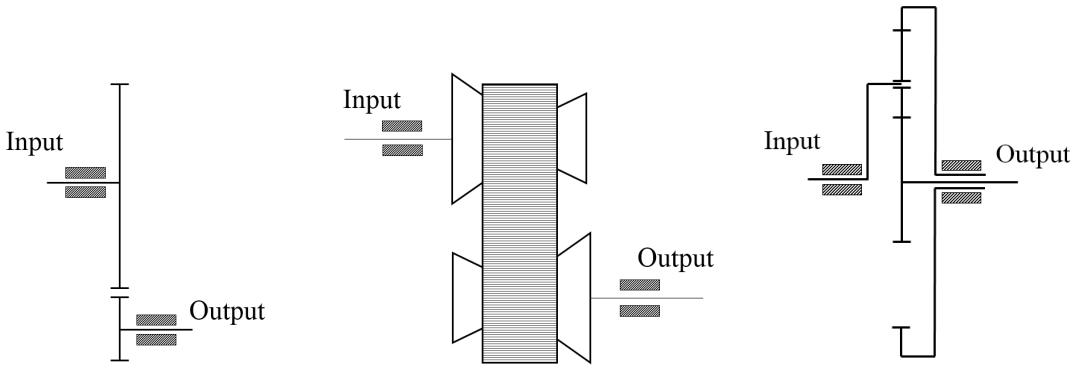

(a) Direct drive (b) CVT (c) PGT

Figure 1.3: Types of gearboxes are used in wind turbines

Depending on the capacity and geometrical size of the wind turbine, different

Figure 1.4: Planetary gear transmission [5]

types of drive trains are used, such as direct drive, simple gear transmission, reverted gear transmission, continuously variable transmission (CVT), and planetary gear transmission (PGT) (see Figure.1.3). Among these, planetary gear transmission is the most common transmission in wind turbines because of its unique properties. These include the number of speed ratios, high power-to-volume ratios, compactness, and high efficiency. Planetary gearboxes include a sun gear, a ring gear, a carrier, and three or more planet gears, depending on the design, as shown in Figure 1.4. The planet gears are mounted on the carrier, and they are enmeshed with both the sun gear and the ring gear. The planets rotate around the sun gear, while the ring gears are either fixed or spinning.

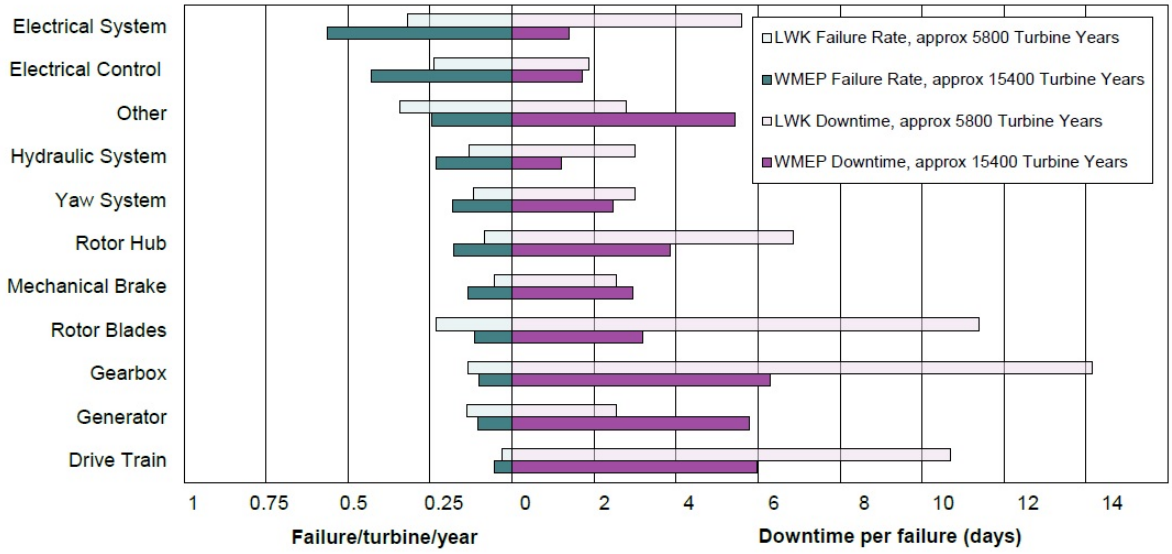

Figure 1.5: Surveys of land-based European wind turbines over 13 years [6]

1.2 Problem Statement

Despite all the advantages of wind turbines, there are significant challenges associated with harnessing their energy. One of the main challenges of extracting energy from wind turbines is component failure. Wind turbines are often installed in places where accessing them for maintenance and repair is difficult, therefore, any failure results in high repair and replacement costs. The failure and downtime of the components of two different types of land-based wind turbines, over 13 years, is shown in Figure 1.5. The components analyzed in the survey include: electrical systems, electrical controls, hydraulic systems, rotor hubs, mechanical brakes, rotor blades, gearboxs, generator, drive trains, and yaw systems.

Figure 1.5 shows that gearbox, drive train, and rotor blades have the highest

downtime per failure in comparison with other components. These parts are the main section of the mechanical part of the wind turbine, which is directly exposed to wind and transfers the generated torque from blades to the generator. In addition, wind continually fluctuates based on its nature, and these fluctuations cause vibration in the mechanical part and is a significant factor in planetary gearboxes' failure.

Among these mechanical parts, the gearbox is the largest contributor to turbine downtime and the costliest to repair per failure when compared to other components, as shown in Figure 1.5. Wind turbine gearboxes are designed to last at least 20 years, however, since they are continuously subjected to fluctuating torques caused by wind speed variation, they fail considerably earlier than intended. They are also one of the most expensive parts of the wind turbine. Thus, their failure is the primary concern in wind turbine design.

1.3 Research Overview

A significant factor in planetary gearboxes' failure is vibration. A significant problem of calculating vibration is that the unpredictability of wind, which makes wind turbine vibration more complicated. This thesis systematically investigates the vibration of PGT in a wind turbine under both deterministic and random loads.

Despite the significance of planetary gearboxes in different industries, the lack of proper methods and analysis has created gaps in procedure. This project creates an occasion for the advancement of this significant scientific topic. The dynamic model

examined in this research, and its analysis, will be useful for analyzing wind turbine gearboxes. The significance of this research, and then findings and developed methods go well beyond the wind power industry. All the methods and analysis developed in this project will be applicable not only for wind turbines, but also for the automation and aviation industries.

Although much research has been conducted in the dynamic behavior of planetary gear trains of a wind turbine, there are research gaps that are essential to analyze the dynamics of wind turbines PGTs deeply. These gaps are mainly in comprehensive modeling of PGTs, solving nonlinear stochastic dynamics of a complex system such as PGT, and applying the effects of elasticity and random moving loads. This thesis focuses on finding the proper model and method to cover these research gaps in modeling wind turbine planetary gear trains.

1.4 Research Contributions

The goal of this project is to investigate the dynamic behavior of planetary gearboxes in wind turbines. More specifically, the research focus is placed on 1) the effect of moving gear meshing loads; 2) the elastic deformation of the ring and 3) the backlash non-linearity. Accordingly, this project's contributions to the state of the art are:

1. A stochastic nonlinear dynamic model of the planetary gear transmission (PGT), taking the elastic ring gear, the elastic supports, nonlinear moving mesh, and multi-backlash into consideration.

2. Develop the nonlinear backlash equation with variables from the finite element-lumped parameter model of PGT.

3. Apply statistical linearization technique on the nonlinear moving mesh of planet-ring pair by considering ring gear elasticity and sun-planet pair of PGT.

4. Developed an energy-based criterion of statistical linearization technique for nonlinear stochastic dynamic gear systems.

5. Developed an accurate model to represent the elastic ring gear.

6. A method for investigating the random moving load effects on the ring gears and analyze the effect of the moving random load speeds on the dynamics of the rings.

Beyond the aforementioned contributions, this project is to provide more insight into the dynamics of planetary gear transmission. Even though the following listed items are not the main contributions, thorough work is to be conducted on them through this project. The following is a list of these items which includes:

- Create a comprehensive list of literature surrounding dynamic behavior of planetary gearboxes in wind turbines.

- A comprehensive model to analysis the random vibration of PGTs, including random load, backlash, and elastic ring gear.

- Develop methods and analysis of the PGTs well beyond the wind power industry.

- Increase the accuracy of analysis and decrease the complexity of the nonlinear random vibration of PGTs.

1.5 Organization of Thesis

The thesis is organized as below:

Chapter 1 (the current chapter) includes the background, research overview, research objectives and organization of this dissertation.

Chapter 2 reviews prior studies of the dynamics of planetary gears, and focuses on the literature of the following topics: PGT dynamics models, solution methods of dynamic equations, the nonlinear dynamics of the PGT, the flexibility of ring gears, moving load of ring gears, and random factors. These point out gaps in the literature.

Chapter 3 creates a model of PGT dynamics that includes a flexible ring gear, backlash, and multi-mesh under random excitation. The hybrid model, which is finite element-lumped parameter modeling, is used in this chapter. The backlashes between sun-planet pairs and ring-planet pairs are represented by a nonlinear function, and this nonlinear equation is then treated with the statistic linearization method. Finally, the response statistics of the PGT model are represented. This chapter is a manuscript of one full journal paper, and one presented conference paper.

Chapter 4 introduces a new version of the statistical linearization method to solve the nonlinear system for a single gear pair. The method is based on energy. The obtained results for a single gear pair are compared with the results of the Monte Carlo Simulations. This chapter is a manuscript of a full research article.

Chapter 5 proposes two models developed to compute the natural frequencies and mode shapes of a ring gear. The first model represents the ring gear as a smooth ring, and the second model represents the ring gear modeled as a smooth ring with attached masses. The obtained results are compared with the results from ANSYS. This chapter is a manuscript of a conference paper.

Chapter 6 provides vibration analysis of the elastic ring gear under a random moving load. The ring gear of the PGT is subjected to a moving load caused by the planets' movement throughout the inside of the ring gear. Therefore, the dynamic responses of the ring gear under random-moving loads are analyzed here. For this purpose, only the ring gear with applied meshing force will be modeled. The obtained results are compared with the results of the Monte Carlo Simulations. This chapter is a manuscript of a full research article.

Chapter 7 provides the general conclusions of this research. Contributions of this work, as well as future research directions, are clearly explained.

Table 1.1: List of Publication

	Chapter	Paper Title	List of Authors	Conference or Journal	Status
1	3	Statistical Linearization of Nonlinear Stiffness Matrix of Planetary Gear Train	Jalal Taheri Kahnamouei, Jianming Yang	ASME 2017 International Mechanical Engineering Congress and Exposition November 3–9, 2017	Accepted, Full paper, 2017
2	3	Development and Verification of a Computationally Efficient Stochastically Linearized Planetary Gear Train Model with Ring Elasticity	Jalal Taheri Kahnamouei, Jianming Yang	Journal of Mechanism and Machine Theory	Submitted, 25th April, 2020 Revision
3	4	Random Vibration of A Nonlinear Gear Pair Using Energy-Based Statistical Linearization	Jalal Taheri Kahnamouei, Jianming Yang	Journal of Acta Mechanica Solid Sinica	Submitted, 10th July, 2020 Under review
4	5	Free Vibration Properties of Ring Gears	Jalal Taheri Kahnamouei, Jianming Yang	CSME-CFDSC Congress 2019, Western University, London, ON, June 2-5, 2019	Accepted, June, 2019 Full paper
5	6	Random Vibration Analysis of Thin-Walled Elastic Rings under Multiple Moving Loads	Jalal Taheri Kahnamouei, Jianming Yang	Proceedings of the Institution of Mechanical Engineers, Part C: Journal of Mechanical Engineering Science	Submitted, 29th October 2019, Under review

References

[1] Letcher TM. WIND energy engineering: a handbook for onshore and offshore wind turbines. Academic Press; 2017 May 11.

[2] Mathew S. Wind energy: fundamentals, resource analysis and economics. Springer; 2006.

[3] Renewable energy facts — Natural Resources Canada [Internet]. Available from: https://www.nrcan.gc.ca/energy/facts/renewable-energy/20069.

[4] How does a wind turbine work? Office of Energy Efficiency & Renewable Energy. https://www.energy.gov/eere/wind/inside-wind-turbine.

[5] Wind Turbine Planetary Gear Trains https://mechanical-engg.com/gallery/image/1219-giant-industrial-planetary-gearboxjpg/.

[6] Sheng S. Report on wind turbine subsystem reliability-a survey of various databases (presentation). National Renewable Energy Lab.(NREL), Golden, CO (United States); 2013 Jul 1.

Chapter 2

Literature Review

2.1 Introduction

Planetary gear trains (PGT) have application in a wide range of industries from energy to aviation because of their unique properties, such as number of speed ratios, high power-to-volume ratio, compactness, and high efficiency. There are many concerns regarding design and operation: one such concern is vibration, especially for some high speed and heavy load applications. For example, PGT in wind turbines have severe dynamic problems, which affect turbine reliability and fatigue life. Extensive research has been conducted to investigate the dynamic performance of PGT [1-3]. Some prominent subjects of existing research include natural frequencies and vibration modes [1, 3-5], mesh phasing [6, 7], instability [6-8], nonlinear dynamics [9, 10], elasticity effect [11, 12], and gear backup ratio [11, 12] in the condition of time-variant mesh stiffness. In addition, review papers have also been published [13, 14] that presented the research has been done in PGT dynamics.

In heavy load applications, some parameters and items are more critical than others, and they include random excitation, nonlinear phenomena, and deformation

of the ring gear. For example, in the PGTs of wind turbines, the deformation of the ring gear becomes non-negligible. Thus, some researchers focus on these phenomena and carry out analyses of their effects on the dynamic response of the PGT [12, 15, 16].

Section 2.2 discusses the main three models used representing the PGT dynamics. Section 2.3 focuses on methods used for solving the dynamic equations. Section 2.4 presents an overview of the nonlinear dynamics of the planetary gear system. Section 2.5 provides a summary of the literature regarding the flexibility of ring gears and offers a brief analysis of the studies. Section 2.6 reviews the literature on random factors. Finally, section 2.7 focuses on the effect of moving load on the elastic ring's dynamic responses.

2.2 Models of Dynamics

Experts utilize dynamic modeling to simulate and analyze the dynamic response of geared systems. Generally, there are three main types of models that demonstrate the dynamic modeling of PGTs: the lumped parameter model (LPM), the finite element model (FEM), and the finite element-lumped parameter models. Thus, the simplification level of a real system, the boundary conditions, and the degrees of freedom each determine the accuracy of the results obtained from each model. The use of each model depends on the purpose and complexity of the research.

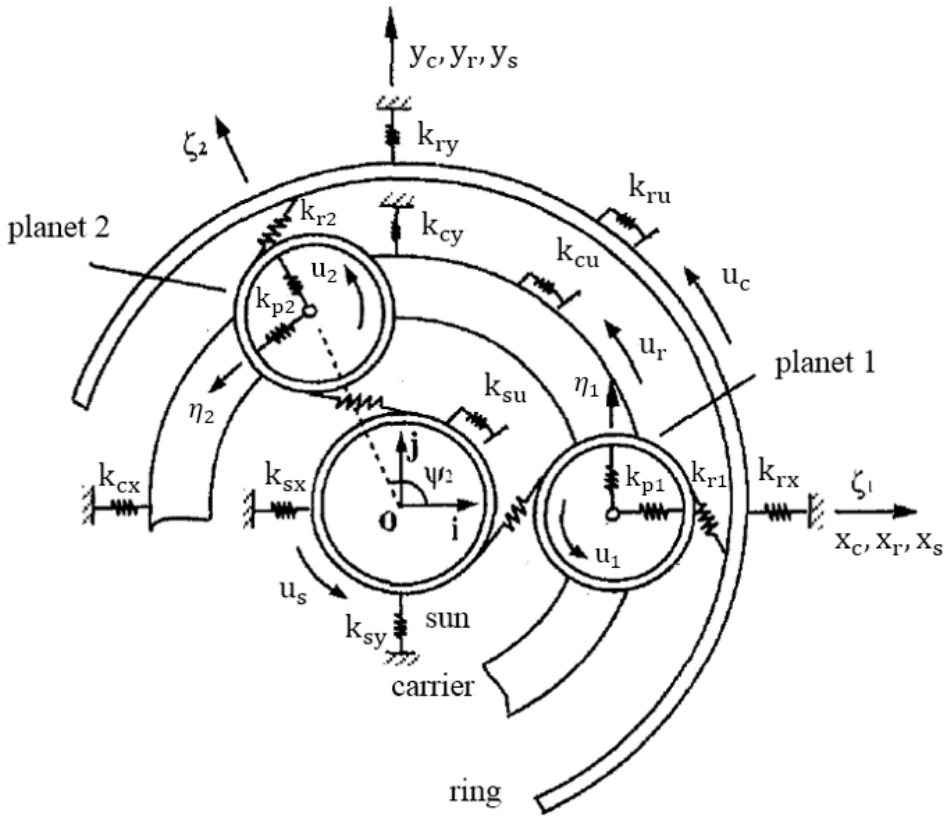

Figure 2.1: Lumped parameter modeling of planetary gear transmission [4]

2.2.1 Lumped parameter modeling

Research has been conducted on the dynamics of PGTs using the lumped-parameter model. Lin and Parker [4] studied the dynamic responses of the PGTs using the typical LPM shown in Figure 2.1. In this model, the carrier and each gear have three degrees of freedom: two transverse motions and one rotational motion. A spring represents each gear mesh between the sun-planet and ring-planet pairs. In addition, each bearing was modeled by springs. Kahraman [17] used the LPM to study the natural frequency of the PGTs. He computed the natural frequencies obtained from

a purely torsional model against a torsional transverse model.

Kahraman [18] applied the LPM to study the influence of the planet meshing phase on dynamic response. In this model, helical gears were considered. Therefore, to represent the three-dimensional model, six degrees of freedom, including three rotational and three transnational, were allocated for each component. In addition, static transmission error was considered an excitation in the LPM.

The LPM is relatively simple and accurate when the flexibility of the system's components is negligible. However, in some applications, the flexibility of gears is important and should be considered to obtain accurate results; for example, the ring gear of PGT is applied in wind turbines. Therefore, an alternative modeling method needs to model the PGT with greater detail.

2.2.2 Finite element modeling

PGTs are a complicated system and oversimplifying them may not give accurate results. Thus, it is necessary to apply more detail, such as the geometry or contact forces through teeth in the model. The lumped parameter model is unable to model all of these details. On the other hand, the finite element model gives us the possibility of applying more detail in the model with high fidelity and accuracy.

Parker *et al.* [19] investigated the dynamic behavior of PGTs under a wide range of operating torques and speeds using semi-analytical finite element modeling. They studied the torque and speed sensitivity of dynamic responses modeled with greater

details of tooth geometry and contact forces between gears. They found a strong agreement between the natural frequencies obtained from the finite element modeling and analytical eigensolution [4].

Ambarisha and Parker [20] examined the dynamics of PGTs with both the finite element and lumped parameter models. Tooth contact loss and mesh stiffness variation were considered as nonlinear springs in the LPM. The finite element model intrinsically considered tooth contact loss and mesh stiffness in the analysis. The obtained result from finite element model were compared to the obtained results from lumped-parameter analytical model. The comparisons showed that the spectra in both sets of results agreed well, and both methods can be used to analyze the dynamic behavior of PGTs.

Although the finite element model gives accurate results, some of the details of transmission, such as sun gear, or planet gears' elastic behavior are not significant and based on the analysis, can be neglected. In addition, FEM often requires significant computational time. Also, in some modeling, the elastic behavior of components should be ignored except the ring gear. Thus, researchers may benefit from a model that combine the speed of the LPM and the accuracy of the FEM.

2.2.3 Finite element-lumped parameter modeling

In order to overcome the high computations of the finite element model, and the lack of reliability of the lumped parameter model, alternative approaches have been

introduced. Finite element-lumped parameter modeling gives the complexity and accuracy of the finite element model for critical components, as well as the simplicity and quickness of the LPM for non-primary components.

Abousleiman and Velex [15, 21] developed the finite element-lumped parameter model to study the dynamics of PGTs and the elastic behavior of ring gear. They modeled the PGT by assembling the finite element model of the flexible ring with the lumped parameters of other components. Therefore, the LPM shows that ring gear deformation influences the general dynamic response of the PGT, and the proposed model can consider the deformation without unnecessarily increasing the complexity of the model. Because brick elements with two nodes were used in modeling the ring, a high number of elements were needed to achieve accurate results. Thus, this model requires greater computational time. In order to describe the circular nature of the ring gear, a curved beam element will be used in this thesis to give a more accurate result with fewer elements.

2.3 Solution of nonlinear dynamic planetary gear trains

The dynamic equation of planetary gears is complex, and if nonlinearity or randomness is added to the equation, the equation becomes more difficult to solve. In the meantime, researchers have introduced various solution methods to solve the dynamic

equation of the PGTs. They were used based on the complexity of the dynamic equations and the required accuracy.

Wu and Parker [1] used a perturbation method, which gives the approximate solution of the nonlinear problems based on assuming a small parameter as a perturbation parameter, to solve dynamic equations of the PGTs with an elastic ring gear. In this study, the results showed that all vibration modes were fitted into four modes, which were rotational, translational, planetary, and purely ring modes. Xun *et al.* [22] solved the dynamic equation of the PGT using the same perturbation method, as mentioned above. The obtained results demonstrated that proper tooth profile modification decreases the system vibration amplitudes.

Sun and Hu [23] used the harmonic balance method, which provides the periodic solutions of nonlinear ordinary differential equations, to solve the dynamics of the PGT system with consideration of the nonlinearity caused by multiple backlashes and time-varying mesh stiffness. They used numerical simulation to verify the proposed method, and the obtained results showed that the variation of stiffness ratio and transmission error have an important role in the nonlinear dynamic behavior of the PGTs. Guo and Parker [24] studied the nonlinear dynamic behavior of the PGTs of wind turbines under simultaneous excitation using the extended harmonic balance method. Numerical integration and finite element modeling were applied to validate the results. Bahk and Parker [9] utilized both the perturbation and harmonic balance methods to solve the nonlinear dynamics of PGTs. They evaluated the accuracy of

both methods with finite element and numerical integration simulations.

Kahraman [18] employed the modal summation method to solve the dynamic responses of the PGTs. For this purpose, he neglected the time-varying meshing stiffness due to the changing number of teeth in the mesh. In addition, Sondkar and Kahraman [25] found the dynamic responses of the double-helical PGT by solving the dynamic equation with the summation method. Sondkar and Kahraman [25] used the same solution method to solve the dynamics of the double-helical PGT. They considered the model with a linear, time-invariant meshing between the gear pairs, as well as any number of planets and supports.

The numerical method is one of the common methods to solve the dynamic equations, mainly when the equations include the nonlinear part. Wei *et al.* [26] applied the numerical precise integration method to solve the multistage planetary gears dynamic equation. They established that this method was more accurate and suitable for solving the equations with a high degree of freedom. Qiu *et al.* [27] analyzed the dynamic response of the PGT under pitching base movements with the Runge-Kutta method. The authors found that when the base movement was considered in the model, it caused the rich parametric exaction beside the parametric excitation due to mesh stiffness variation. Kim, *et al.* [28] used the Newmark time integration method to solve the nonlinear dynamic equation of planetary gears with time-varying pressure angles and contact ratio. The authors applied the Newton Raphson method at each time step defined by the Newmark algorithm. Yang and Yang [29] applied

the stochastic Newmark scheme to solve the PGT dynamic equation under both random and deterministic excitation. The authors analyzed the effect of the white noise intensity on the dynamic responses of the PGT.

All these presented methods have limitations when the model includes nonlinearity and randomness parameters.These methods are not able to solve the stochastic problems, and they can only provide the mean value of results; on the other hand, mean value, variance, and higher-order moments of results are essential for analyzing the systems under random excitation. Thus, it is necessary to introduce a new approach to evaluate the nonlinear PGTs' nonlinear stochastic dynamic behavior. This thesis will present a useful solution method to solve the nonlinear stochastic vibration of PGT with statistical linearization technique.

2.4 Nonlinearity

Due to the existence of nonlinear phenomena such as backlash, manufacturing errors, and mesh stiffness variation, nonlinearity is an inevitable part of a gear system. These nonlinear sources have different effects on the dynamic behavior of the PGTs. Among them, tooth backlash has strong nonlinearity because of the unexpected loss of contact. Mesh stiffness variation is caused by changing the number of teeth in mesh contact. Significant research has been undertaken regarding the nonlinear dynamics of the planetary gear.

Kahraman [2] developed a nonlinear dynamic model of planetary gearboxes, which

included contact loss, manufacturing errors, and mesh stiffness variation. He defined dynamic load sharing factors and analyzed the influence of design parameters on dynamic load sharing factors. Sun *et al.* [23] attempted to model a nonlinear dynamic system for the planetary gear by considering multiple backlashes, error excitation, and mesh stiffness variation. They solved it using the harmonic balance method and conducted a parametric study. The analysis demonstrated that the increase of mesh stiffness variation and static transmission errors intensified the nonlinearity of the system.

Ambarisha *et al.* [20] employed a lumped-parameter model and a finite element method to investigate the nonlinear dynamic behavior of planetary transmissions. They considered the gear meshes as nonlinear due to tooth separation, and the system showed high nonlinear dynamic responses, such as chaotic motions. Bahk *et al.* [9] studied the nonlinear dynamic response of planetary gearboxes by considering the mesh stiffness variation. They conducted the parametric analysis for the operating range of the mesh frequencies. The analysis demonstrated that the tooth separation exists at large external torque.

Guo and Parker [30, 31] studied the dynamic behavior of the planetary gear of a wind turbine. They extended the nonlinear dynamic equations, which included contact loss, mesh stiffness variation and bearing clearance. They found that excitation, due to the clearance, caused chaos. Furthermore, Guo [24] had researched nonlinear dynamics of wind turbines' planetary transmissions, which were affected by gravity.

The results showed that the nonlinearity of the system was enhanced because of tooth wedging and bearing-raceway contacts caused gravity.

Kim [28] developed a nonlinear dynamic model, which included time-varying pressure angles and contact ratios for the planetary gearboxes. He found that this model had higher radial displacements and greater mesh deformations in comparison to constant pressure angle and contact ratios. Li *et al.* [32] used a numerical method to solve the nonlinear equations of motion on multi-stage planetary gear. They also studied bifurcation and chaos, which were influenced by backlash, damping coefficient, and excitation frequency. The results show that these parameters caused different nonlinear dynamic responses to the system.

Considering nonlinearity alongside the random load and ring gear, elasticity makes the PGT's model more complicated. There is no precise method to solve the nonlinear random vibration of complicated systems. All these works of literature studied the nonlinear dynamic behavior of the PGT with rigid ring gear under deterministic excitation.

2.5 Flexibility of the Ring Gear

Ring gears are considered rigid bodies in many studies. In real PGT systems, to maintain a high torque-to-weight ratio, the ring gear is designed with thin rims. However, the thin ring gear elastic deformation under operating conditions has become an important issue. This elastic behavior has a significant effect on the dynamic behavior of

the gearbox. Therefore, the elastic behavior of the ring gear is necessary to consider because the rigid body model cannot sufficiently assess an accurate dynamic response of the system.

Tanna and Lim [33] studied the free vibration characteristics of elastic ring gear. They compared the results obtained from smooth ring and ring gear models with experimental results to establish the more accurate method to model the ring gear, and they found that the ring gear model considering the effect of teeth was more accurate. Kahraman *et al.* [11, 12] analyzed the influence of the flexibility of inner gears on the dynamic behavior of a planetary gearbox using the finite element/semi-analytical model. They investigated the influence of rim thickness on ring gear stress, ring gear deflection, and the planet sharing load. The results indicated that elastic ring gear had a significant impact on increasing the bending stress of the teeth on all ring gear and on balancing the planet load sharing.

Abousleiman *et al.* [15] present finite element and lumped parameter models to analyze the three-dimensional dynamic response of PGT with deformable ring gear. The results found that elastic ring gears helped improve load distributions on ring-planet pair meshes. They [21] developed the model to incorporate finite element models of both the elastic ring and the carrier, and realized that the elastic deflection of the ring gear was more critical than the carrier in their case study.

Wu *et al.* [1] studied the modal properties and natural frequencies of a planetary gearbox with thin flexible ring gear. They concluded that rotational, translational,

planet, and purely ring modes were the vibration modes of equally-spaced PGTs with flexible ring gear. Wu [34] also investigated the vibration of flexible ring gear fixed with elastic supports. They found that the natural frequencies affected by stiffness of springs, angle of supports, number and location of the springs. Later, they [35] studied the effects of unequally spaced planets on the dynamic characteristics of planetary gearboxes with flexible inner gears. In addition, they investigated the relation between the modal properties of PGTs.

Chen, and Shao [16, 36] utilized a curved Timoshenko beam to model a flexible ring gear. They assumed the tooth was rigid and analyzed the influence of the number and kind of support points on the meshing stiffness of ring-planet gear pairs. They analyzed the effects of tooth root crack on the dynamic response of PGT by potential energy and the curved-beam model. Furthermore, they studied the effects of rim deformation and the mesh stiffness of PGTs.

Wei *et al.* [26] established the virtual equivalent shaft method to analyze the vibration of planetary transmissions with a deformable ring gear and a flexible planet carrier. They concluded that the influence of the ring gear elasticity was dominant, and the effect of the deflection of the carrier was negligible. Hu. [37] utilized the baseline model to formulate a planetary gearbox with a elastic ring gear. They used the model to predict the ring gear deflection and to analyze the ring gear deformation on dynamic responses of the PGTs. The analysis revealed that ring deformation had a significant effected on ring-planet gear. In addition, the results showed that elastic

ring gear improved load distribution of PGTs with manufacturing errors.

All these studies examined the free or deterministic vibration of the ring gear. However, the random vibration of the ring gear individually or, in a complete model PGT has not been conducted.

2.6 Random Loads

Geared systems are under two types of forces, which are internal and external loads. Meshing forces are internal, which are created from gear mesh. Deterministic and random loads applied from the outsides are external loads. In the majority of the analysis, internal load and deterministic loads are considered in the system. Even though many analyses have been conducted of planetary gearboxes subjected to deterministic excitation, few have been conducted regarding the planetary gear dynamics under random excitation. However, random factors always exist and have an essential effect on geared system dynamics. In applications that are directly subjected to external random loads, such as wind turbine gearboxes or land vehicle transmissions, random load effects cannot be ignored.

Through a few publications considering randomness, Yang and Yang [29] analyzed the random vibration behavior of the PGT under combined external white noise and deterministic excitation. They examined the effect of the noise levels on dynamic responses they found out that the variances of the response were affected by the noise level. This study focused only on PGT, and later they published an extended work

[38], which studied the dynamic behavior of wind turbines' PGT under wind turbulence. They used colored noise to applied wind turbulence as a random excitation to the model.

Srikanth and Sekhar [39, 40] built the dynamic model of the PGT of a wind turbine subjected to stochastic wind loads which were estimated according to the standard model. Wei and Han [42] investigated the influence of various uncertain parameters on the dynamic response of the wind turbines' PGT when subjected to the random wind excitation. During the examination of the effect of different parameters, they found that the uncertain stiffness parameters at the intermediate and high-speed stages had significant effects on the dynamic responses of the system.

Wang and Shen [43] investigated the dynamic response of wind turbines' PGT with consideration for the random factors, loads and design parameters. They used Runge-Kutta and the random sampling method to determine the dynamic responses and the statistic method to determine the meshing forces. Beyaoui *et al.* [45] studied the stochastic dynamic responses of the PGTs, and they considered the random factor caused by the variation of aerodynamic torque on wind turbine blades. In order to define the random factor, uniform and normal probability distributions were applied to the model. The study [44] is the only research that investigated the dynamic behavior of a wind turbines' PGT under the effects of random wind excitation and the stability of the system under the effects of random backlash. In this research, since the ring gear elasticity was not considered, the torsional model of PGT was used, and

the impact of a backlash on dynamic responses of the system was not studied.

In all the above literature, the random vibration of the wind turbine's PGT was studied. Although, none of those accurately represented the dynamic behavior of PGT because of simplifying the model, disregarding the elastic effects of the ring gear and backlash nonlinearity.

2.7 Moving Load

The ring gear of planetary gearboxes is subjected to a moving load caused by the movement of the planets throughout the inside of the ring gear. As noted in section 2.5, in order to analyze the PGT dynamic behavior accurately, it is necessary to consider the elasticity of the ring gears. Meshing forces due to the moving planets through the ring gear cause deflection on the ring gear. Thus, to accurately study the dynamics of the PGTs, it is necessary to consider the moving load on the model and its effects on other components, especially on ring gear.

Metrikine and Tochilin [46] investigated the steady-state response of a deformable ring under a moving load by an analytic method. The authors assumed that elastic springs attached the ring to the fixed point, and load was applied in a radial direction. They analyzed the effect of the load moving velocity on the ring patterns. The results show that at the lower load velocity the ring pattern was symmetric and at the high load velocity it becomes asymmetric. Forbes and Randall [49] investigated the dynamic responses of a flexible ring under a moving load and analyzed the reso-

nance phenomenon caused by the moving loads. The authors considered the ring was stationary. They analyzed the effect of the magnitude-varying moving load, phase varying moving load, and non-uniform continuous moving load on dynamic response of the elastic ring. Both published papers focused on the dynamics of the ring under moving spring, but they have not studied the effect of moving loads in mechanisms such as the planetary gear trains. In addition, a single-deterministic moving load was considered, which in actual cases, we have multi-random and deterministic forces.

Canchi and Parker [47] investigated the vibration of elastic ring gear excited by moving springs, which represent the moving loads. They analyzed the ring's parametric instabilities by considering the spring's stiffness alteration, number spacing, and placement. The same authors [48] employed a rotating thin-walled ring to model and analyze the in-plane vibration and instability of a ring gear due to moving springs. In this study, multiple moving springs with time-variant stiffness were considered as moving loads. In addition, the examinations have been conducted on the rotating and non-rotating ring under moving springs. Although this research focused on the dynamic behavior of ring gear under multi-moving loads, randomness was not considered in the model. In addition, the dynamic behavior of the ring gear under various moving load speeds was not investigated.

2.8 Current Status of the Research Gap in PGT

Based on the literature review presented, and despite the vast amount of research that has been done on the dynamics of PGTs, relatively little attention has been given to the random vibration of PGT. Thus, according to the literature, several gaps are detected are presented:

- The majority of these works introduced a simple model, and none of them considered nonlinearity, ring gear elasticity, and random excitation simultaneously in a dynamic model of the PGT wind turbines.
- There are still many gaps in the ability to solve the nonlinear stochastic dynamics of PGT and analyzing the effect of random-moving loads on ring gears.
- Although several studies conducted on statistical linearization of nonlinear geared system dynamics, all of these studies focused on the single gear pair.
- Only the forced-based statistical linearization was introduced to treat the nonlinear gear system dynamics. However, there are several criteria, such as an energy-based statistical linearization, which can be used to solve the nonlinear dynamics of the geared systems.

For this reason, the overall aim of this thesis is to develop a model to analyze the nonlinear stochastic dynamics of the planetary gear trains of wind turbines.

2.9 Conclusion

Few experiments show that the PGTs are affected by various complex phenomena, such as elastic behavior of ring gear, backlash, time-variant mesh stiffness, and randomness. Considering these phenomenon in the PGT model makes it more realistic and increase the model complexity. Prior studies failed to treat the nonlinear random vibration of the planetary gearboxes of wind turbines with the elastic ring gear. Thus, we should develop a feasible method to model and analyze the PGTs' dynamic behavior in such a way as close as to the realistic case.

References

[1] Wu X, Parker RG. Modal properties of planetary gears with an elastic continuum ring gear. Journal of Applied Mechanics. 2008 May 1;75(3).

[2] Kahraman A. Load sharing characteristics of planetary transmissions. Mechanism and Machine Theory. 1994 Nov 1;29(8):1151-1165.

[3] Kahraman A. Free torsional vibration characteristics of compound planetary gear sets. Mechanism and Machine Theory. 2001 Aug 1;36(8):953-71.

[4] Lin J, Parker RG. Analytical characterization of the unique properties of planetary gear free vibration. ASME: Journal of Vibration and Acoustic. 1999 Jul;121(3), 316–321.

[5] Guo Y, Parker RG. Purely rotational model and vibration modes of compound planetary gears. Mechanism and Machine Theory. 2010 Mar 1;45(3):365-77.

[6] Lin J, Parker RG. Planetary gear parametric instability caused by mesh stiffness variation. Journal of Sound and vibration. 2002 Jan 3;249(1):129-45.

[7] Lin J, Parker RG. Mesh stiffness variation instabilities in two-stage gear systems. J. Vib. Acoust.. 2002 Jan 1;124(1):68-76.

[8] Parker RG, Wu X. Parametric instability of planetary gears having elastic continuum ring gears. Journal of vibration and acoustics. 2012 Aug 1;134(4).

[9] Bahk CJ, Parker RG. Analytical solution for the nonlinear dynamics of planetary gears. Journal of Computational and Nonlinear Dynamics. 2011 Apr 1;6(2).

[10] Al-Shyyab A, Kahraman A. A non-linear dynamic model for planetary gear sets. Proceedings of the Institution of Mechanical Engineers, Part K: Journal of Multi-body Dynamics. 2007 Dec 1;221(4):567-76.

[11] Kahraman A, Kharazi AA, Umrani M. A deformable body dynamic analysis of planetary gears with thin rims. Journal of sound and vibration. 2003 May 1;262(3):752-68.

[12] Kahraman A, Vijayakar S. Effect of internal gear flexibility on the quasi-static behavior of a planetary gear set. Journal of Mechanical Design. 2001 Sep 1;123(3):408-15.

[13] Cooley CG, Parker RG. A review of planetary and epicyclic gear dynamics and vibrations research. Applied Mechanics Reviews. 2014 Jul 1;66(4).

[14] Yang J, Dai L. Survey of dynamics of planetary gear trains. International Journal of Materials and Structural Integrity. 2008 Jan 1;1(4):302-22.

[15] Abousleiman V, Velex P. A hybrid 3D finite element/lumped parameter model for quasi-static and dynamic analyses of planetary/epicyclic gear sets. Mechanism and Machine Theory. 2006 Jun 1;41(6):725-48.

[16] Chen Z, Shao Y. Mesh stiffness of an internal spur gear pair with ring gear rim deformation. Mechanism and Machine Theory. 2013 Nov 1;69:1-2.

[17] Kahraman A. Natural modes of planetary gear trains. Journal of Sound Vibration. 1994 May;173:125-30.

[18] Kahraman A. Planetary gear train dynamics. Journal of Mechanical design. 1994 Sep;116(3):713-20.

[19] Parker RG, Agashe V, Vijayakar SM. Dynamic response of a planetary gear system using a finite element/contact mechanics model. Journal of Mechanical Design. 2000 Sep 1;122(3):304-10.

[20] Ambarisha VK, Parker RG. Nonlinear dynamics of planetary gears using analytical and finite element models. Journal of sound and vibration. 2007 May 8;302(3):577-95.

[21] Abousleiman V, Velex P, Becquerelle S. Modeling of spur and helical gear planetary drives with flexible ring gears and planet carriers. ASME: Journal of Mechanical Design. 2007 Jan;129(1):95–106

[22] Xun C, Long X, Hua H. Effects of random tooth profile errors on the dynamic behaviors of planetary gears. Journal of Sound and Vibration. 2018 Feb 17;415:91-110.

[23] Sun T, Hu H. Nonlinear dynamics of a planetary gear system with multiple clearances. Mechanism and Machine Theory. 2003 Dec 1;38(12):1371-90.

[24] Guo Y, Keller J, Parker RG. Nonlinear dynamics and stability of wind turbine planetary gear sets under gravity effects. European Journal of Mechanics-A/Solids. 2014 Sep 1;47:45-57.

[25] Sondkar P, Kahraman A. A dynamic model of a double-helical planetary gear set. Mechanism and Machine Theory. 2013 Dec 1;70:157-74.

[26] Wei J, Zhang A, Qin D, Lim TC, Shu R, Lin X, Meng F. A coupling dynamics analysis method for a multistage planetary gear system. Mechanism and Machine Theory. 2017 Apr 1;110:27-49.

[27] Qiu X, Han Q, Chu F. Dynamic modeling and analysis of the planetary gear under pitching base motion. International Journal of Mechanical Sciences. 2018 Jun 1;141:31-45.

[28] Kim W, Lee JY, Chung J. Dynamic analysis for a planetary gear with time-varying pressure angles and contact ratios. Journal of Sound and Vibration. 2012 Feb 13;331(4):883-901.

[29] Yang J, Yang P. Random vibration analysis of planetary gear trains. Journal of Vibration and Acoustics. 2013 Apr 1;135(2).

[30] Guo Y, Parker RG. Dynamic modeling and analysis of a spur planetary gear involving tooth wedging and bearing clearance nonlinearity. European Journal of Mechanics-A/Solids. 2010 Nov 1;29(6):1022-33.

[31] Guo Y, Parker RG. Dynamic analysis of planetary gears with bearing clearance. Journal of computational and nonlinear dynamics. 2012 Oct 1;7(4).

[32] Li S, Wu Q, Zhang Z. Bifurcation and chaos analysis of multistage planetary gear train. Nonlinear Dynamics. 2014 Jan 1;75(1-2):217-33.

[33] Tanna RP, Lim TC. Modal frequency deviations in estimating ring gear modes using smooth ring solutions. Journal of sound and vibration. 2004;269(3-5):1099-110.

[34] Wu X, Parker RG. Vibration of rings on a general elastic foundation. Journal of Sound and Vibration. 2006 Aug 8;295(1-2):194-213.

[35] Parker RG, Wu X. Vibration modes of planetary gears with unequally spaced

planets and an elastic ring gear. Journal of Sound and Vibration. 2010 May 24;329(11):2265-75.

[36] Chen Z, Shao Y, Su D. Dynamic simulation of planetary gear set with flexible spur ring gear. Journal of sound and vibration. 2013 Dec 23;332(26):7191-204.

[37] Hu Y, Talbot D, Kahraman A. A Gear Load Distribution Model for a Planetary Gear Set With a Flexible Ring Gear Having External Splines. Journal of Mechanical Design. 2019 May 1;141(5).

[38] Yang J, Yang P. Random vibration and dynamic analysis of a planetary gear train in a wind turbine. Shock and Vibration. 2016;2016.

[39] Srikanth P, Sekhar AS. Dynamic analysis of wind turbine drive train subjected to nonstationary wind load excitation. Proceedings of the Institution of Mechanical Engineers, Part C: Journal of Mechanical Engineering Science. 2015 Feb;229(3):429-46.

[40] Srikanth P, Sekhar AS. Wind turbine drive train dynamic characterization using vibration and torque signals. Mechanism and Machine Theory. 2016 Apr 1;98:2-0.

[41] Alemayehu FM, Ekwaro-Osire S. Loading and design parameter uncertainty in the dynamics and performance of high-speed-parallel-helical-stage of a wind turbine gearbox. Journal of Mechanical Design. 2014 Sep 1;136(9).

[42] Wei S, Han Q, Peng Z, Chu F. Dynamic analysis of wind turbine gearboxes with

unknown-but-bounded parameters under random wind excitation. IET Renewable Power Generation. 2016 Jun 29;11(4):433-42.

[43] Wang L, Shen T, Chen C, Chen H. Dynamic reliability analysis of gear transmission system of wind turbine in consideration of randomness of loadings and parameters. Mathematical Problems in Engineering. 2014;2014.

[44] Chen H, Wang X, Gao H, Yan F. Dynamic characteristics of wind turbine gear transmission system with random wind and the effect of random backlash on system stability. Proceedings of the Institution of Mechanical Engineers, Part C: Journal of Mechanical Engineering Science. 2017 Jul;231(14):2590-7.

[45] Beyaoui M, Tounsi M, Abboudi K, Feki N, Walha L, Haddar M. Dynamic behaviour of a wind turbine gear system with uncertainties. Comptes Rendus Mecanique. 2016 Jun 1;344(6):375-87.

[46] Metrikine AV, Tochilin MV. Steady-state vibrations of an elastic ring under a moving load. Journal of Sound and Vibration. 2000 May 4;232(3):511-24.

[47] Canchi SV, Parker RG. Parametric instability of a circular ring subjected to moving springs. Journal of Sound and Vibration. 2006 May 30;293(1-2):360-79.

[48] Canchi SV, Parker RG. Parametric instability of a rotating circular ring with moving, time-varying springs. Journal of Vibration and Acoustics. 2006 April; 128(2):231-43.

[49] Forbes GL, Randall RB. Resonance phenomena of an elastic ring under a moving load. Journal of sound and vibration. 2008 Dec 23;318(4-5):991-1004.

Chapter 3

Development and Verification of a Computationally Efficient Stochastically Linearized Planetary Gear Train Model with Ring Elasticity

Jalal Taheri Kahnamouei, Ph.D. Candidate

Jianming Yang, Associate Professor

Faculty of Engineering and Applied Science, Memorial University ofNewfoundland,

St. John's, NL, Canada AlB 3X5

The chapter was published as a full research paper to the Journal of Mechanism and Machine Theory (DOI: 10.1016/j.mechmachtheory.2020.104061). Also, it was part of the presented research paper to the ASME 2017, International Mechanical Engineering Congress and Exposition, November 3-9, 2017, Tampa, Florida, USA.

In this chapter, the stochastic nonlinear hybrid model of planetary gear transmission

with elastic ring gear is presented. The elastic behavior of the ring gear and nonlinear backlash between gear pairs are the challenges of modeling the planetary gear transmission (PGT) under random excitation. Thus, the finite element-lumped parameter model was developed to model the PGT with the elastic ring gear, and the statistical linearization (SL) method was applied to nonlinear moving mesh loads to solve the nonlinearity. In the proposed model, to solve the nonlinear equations of the planetary gear trains, the statistical linearization method was used. To the best of my knowledge, there is no published research similar to this chapter in which PGT modeled with considering nonlinearity, randomness, and ring gear elasticity. In addition, more figures regarding the dynamic response of the PGT components, discussed in section 3.6.1 in this chapter, are shown in the Appendix at the end of the thesis.

Tobe [31]and Yang [27] applied the statistical linearization into the fixed gear pair with only rotational movement.

Abstract

This paper develops a hybrid dynamic model for the analysis of nonlinear stochastic vibration of a wind turbine's planetary gear train (PGT) with an elastic ring gear. The elastic deformation of ring gear is considered and incorporated into the model through the finite element model. Moving loads are used to incorporate the meshing loads between the planet-ring gear pairs. In addition, the model includes both the stiffness variation and the backlash nonlinearity between meshing gears. The backlash

is linearized using the statistical linearization technique, and a linear set of equations is obtained based on which simulation is carried out with PGT parameters in wind turbines. A parametric study is conducted, and the results demonstrate that the statistical linearization method is accurate enough to study the nonlinear stochastic PGT. The results reveal that the moving mesh has a strong effect on PGT when the ring gear elasticity is considered. The influence of rim thickness on PGT dynamics was analyzed, and the results show that the effect is significant. Monte Carlo simulations are used to verify the accuracy of the proposed method.

3.1 Introduction

Planetary Gear Trains (PGT) have a wide range of applications in several industries because of their unique properties. Vibration and dynamics are two main concerns in the design and operation of PGTs, especially for high speed and heavy load applications. Wind turbine PGTs have severe dynamic problems that severely affect reliability and fatigue life, and this paper seeks to propose the model and the method to help solve those problems.

Significant research has been conducted on the nonlinear dynamics of PGTs, particularly the factors of backlash and mesh stiffness variation, which causes the dynamics of gear systems to become nonlinear [1-4]. Kahraman conducted a significant study into the field of nonlinear PGT dynamics [1] which included contact loss, manufacturing errors, and mesh stiffness variation. Sun *et al.* [5] attempted to model a

nonlinear dynamic system for the planetary gear by considering multiple backlashes, error excitation, and mesh stiffness variation. They discovered that a variety of stiffness ratio and transmission errors have a significant effect on the dynamic behavior of PGTs. Ambarisha and Parker [6] considered tooth separation as a nonlinear phenomenon, and used a lumped-parameter model and a finite element method to study the dynamic behavior of planetary transmissions, and the obtained results showed chaotic motions responses. Guo and Parker [7, 8] studied the dynamic behavior of the planetary gear of wind turbines by considering contact loss, mesh stiffness variation, and bearing clearance. They discovered that the PGT showed the chaotic responses because of internal excitation due to the clearance.

In the majority of studies, ring gear was modeled as a rigid body; however, in real PGT systems, the ring gear is designed with thin-wall thickness rims to maintain a high torque-to-weight ratio. Thin ring gears show elastic behavior under operating conditions for heavy load applications, and the deformation of the ring gear has a critical effect on the dynamic behavior of PGTs. Several studies have looked into the impact of the ring's elasticity on the dynamic behavior of PGTs. Kahraman *et al.* [9, 10] studied the influence of ring gear thickness on ring gear stress, ring gear deflection, and the planet sharing load, by using the finite element/semi-analytical model. The results showed that elastic ring gear had a significant influence on balancing the load sharing on the planet. Abousleiman *et al.* [11, 12] analyzed the effect of elastic ring gear on the load distributions on ring-planet pair meshes. They discovered that elastic

ring gears improve load distributions throughout ring-planet pair meshes, and that the effect of elasticity of the ring gear was more influential than the elasticity of other components. Yong Hu [13] studied the effect of the elasticity of ring gear on the load distribution of PGTs. Their analysis revealed that the ring deformation affected ring-planet gear mesh, and modified load distribution on PGTs.

Although research on PGT dynamics is abundant, very little research has been conducted regarding PGT stochastic dynamics, particularly, there is a lack of study on the element of randomness. Randomness is an essential feature in geared system dynamics and for some systems, the primary workload is random, such as the transmission set in wind turbines. A few publications have begun to consider the impact of randomness on PGT dynamics [14-18] . Yang and Yang [19, 20] investigated the response of a PGT under random external excitation of white noise and colored noise. They discovered that the variance in responses was affected by the noise level. Beyaoui *et al.* [21] studied the stochastic dynamic responses of PGTs, and they considered the random factor caused by the variation of aerodynamic torque on wind turbine blades. Chen [22] investigated the dynamic behavior of a wind turbine's PGT under random wind excitation. Chen's research did not consider ring gear elasticity, and the influence of backlash on the dynamic behavior of PGT was not analyzed. All aforementioned literature in this section studied either nonlinearity, randomness, or ring gear elasticity of PGTs. PGT models became more complicated when nonlinearity, randomness and ring gear elasticity are considered into model. Currently, there is

no precise method to solve the nonlinear random vibration of PGT dynamic systems.

In this paper, we analyze the stochastic nonlinear dynamics of wind turbine PGTs with elastic ring gear. Section 3.2 proposes a hybrid model that combines elements of finite element model (FEM) with lumped parameter model (LPM). Section 3.3 used the element of wind torque to the proposed hybrid model, which includes a deterministic and a turbulent component. Section 3.4 discusses the stochastic linearization technique, which is used to linearize the proposed stochastic nonlinear model. Section 3.5 is a look at the solution method, which is based on the stochastic Newmark algorithm, and is used in this paper to solve the obtained equivalent linear model. Section 3.6 describes the Monte Carlo simulations (MCS), which were carried out to verify the results. Section 3.7 covers the results and analysis of simulation using the proposed model, and then verifies those results using Monte Carlo simulations (MCS). A parametric study is also conducted based on the simulation to study the effect of ring gear wall thickness on the dynamic response of the PGT.

3.2 Dynamic Model

In this paper, the proposed hybrid PGT model (Figure 3.1) contains specific components used to study the stochastic nonlinear vibration. The core components of a PGT are sun gear, three planet gears, a carrier, and a ring gear. For the sun gear, planet gears, and carrier, the planet gears transmission and rotation displacements are considered, and LPM was used for modeling them. An elastic thin-walled ring

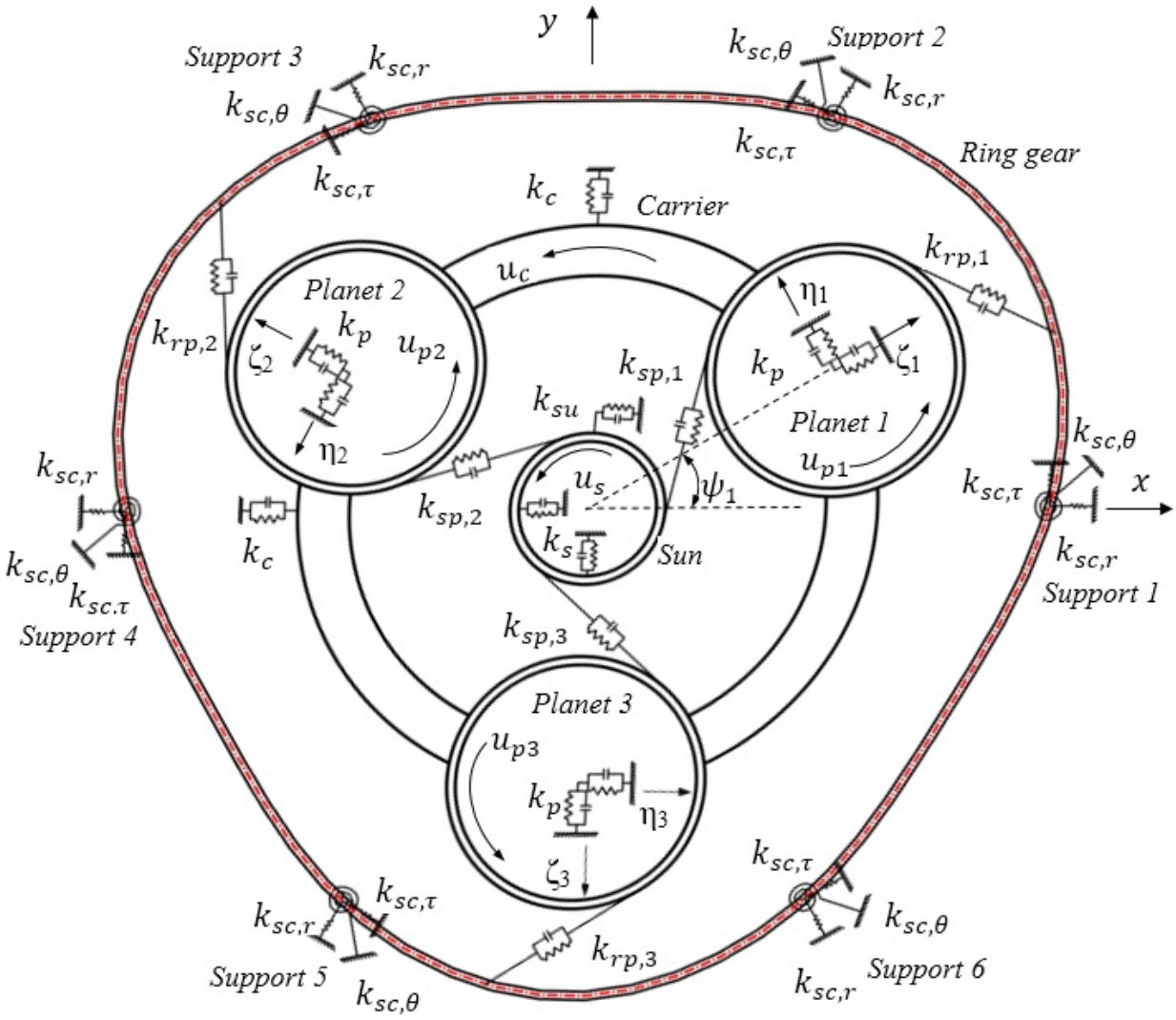

Figure 3.1: Hybrid model of planetary gear transmission

is used to represent the ring gear, which is assembled to the frame through several equally-spaced bolt connections. FEM was used to model the elastic ring, and stiffness and mass matrices of each element were calculated based on the curved beam theory. The meshing force between the ring-planet pairs was applied to the model as moving loads.

Choosing suitable subscripts and coordination systems is critical to defining the equation of motion of each component properly. Throughout the paper, the subscripts c, s, r, and p represent the carrier, sun gear, ring gear, and planet gear, respectively. sp and rp represent the sun-planet and ring-planet gear pairs. In addition, Three coordinate frames are used in the model: xy for the sun gear and carrier, $\xi\eta$ for the planet gears, and $\upsilon\tau$ for the ring's element. The rotational displacements along the line of action are $u_i = R_i\theta_i$ $(i = s, c, p)$ where R_i is the base circle radius of gear body or the radius of the carrier, and θ_i is the component rotation. Meshing stiffness is assumed as time-variant stiffness (see Figure 3.2), and the Fourier Series is used to represent it as [23]:

$$k(t)_{i,n} \approx \bar{k}_i + 2k_i^a \sum_{j=1}^{z} \left(p_{i,n}^{(j)} \sin \omega(t - \Omega_{i,n} T_m) + q_{i,n}^{(j)} \cos \omega(t - \Omega_{i,n} T_m) \right) \quad i = sp, rp \tag{3.1}$$

where $\bar{k}_i$ is the average of the stiffness, $p_{i,n}^{(j)}$ and $q_{i,n}^{(j)}$ are the harmonic coefficients of Fourier series (see Appendix 3.A.1), z is the number of the harmonic terms retained, k_i^a amplitude of the stiffness variation, ω is the meshing frequency, T_m is the mesh period, $\Omega_{sp,n}$ is the phase shift between the first and n^{th} sun-planet meshes, $\Omega_{rp,n}$ the phase shift between the first and n^{th} ring-planet meshes. Also, Ω_{sr} is denote phasing shift between the ring-planet and sun-planet meshes for the n^{th} planet, and $\bar{c}_s$ and $\bar{c}_r$ are contact ratios as shown in Figure 3.2.

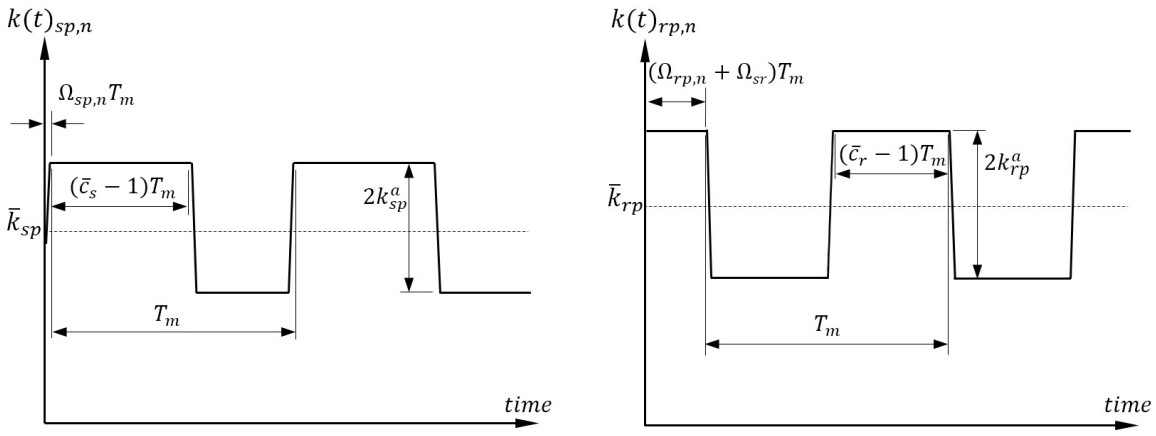

(a) Mesh stiffness of sun-planet mesh

(b) Mesh stiffness of ring-planet mesh

Figure 3.2: Time varying mesh stiffness of gear pair

3.2.1 Sun Gear

The sun gear is the central gear of the PGT, and in the wind turbine, it is used as the output. Using the above notation, the relative compression displacement along the line of action, $\delta_{sp,n}$, in the arbitrary n^{th} sp pair without backlash, can be represented as:

$$\delta_{sp,n} = -x_s \sin\psi_{sp,n} + y_s \cos\psi_{sp,n} + u_s - \xi_n \sin\alpha_s - \eta_n \cos\alpha_s + u_{p,n} \tag{3.2}$$

$$\psi_n = \frac{2\pi\,(n-1)}{N} \qquad n = 1, 2, ...N \tag{3.3}$$

$$\psi_{sp,n} = \psi_n - \alpha_s \tag{3.4}$$

where α_s is the pressure angle of the sun gear, ψ_n is the position of the n^{th} planet, N is the total number of planets. Taking the backlash into consideration, the meshing force in the n^{th} sp mesh can be written as:

$$f_{sp,n} = \begin{cases} k\left(t\right)_{sp,n}\left(\delta_{sp,n} - b_{sp}\right), & \delta_{sp,n} \geq b_{sp} \\ 0, & -b_{sp} \leq \delta_{sp,n} \leq b_{sp} \\ k\left(t\right)_{sp,n}\left(\delta_{sp,n} + b_{sp}\right), & \delta_{sp,n} \leq -b_{sp} \end{cases} \tag{3.5}$$

where $k_{sp,n}$ is the mesh stiffness between the sun and the n^{th} planet gear, and $2b_{sp}$ is the total clearance between the meshing teeth. If we do not consider the damping at this point, the equations of motion for the sun gear are as follows:

$$m_s\ddot{x}_s + k_s x_s - \sum_{n=1}^{N} f_{sp,n}\sin\psi_{sp,n} = 0 \tag{3.6}$$

$$m_s\ddot{y}_s + k_s y_s + \sum_{n=1}^{N} f_{sp,n}\cos\psi_{sp,n} = 0 \tag{3.7}$$

$$\frac{I_s}{R_s^2}\ddot{u}_s + k_{su}u_s + \sum_{n=1}^{N} f_{sp,n} = 0 \tag{3.8}$$

where k_s and k_{su} are bearing the stiffness of the sun in transnational and rotational directions.

3.2.2 Carrier

The carrier holds the planet gears, and it rotates relative to the sun gear. In the wind turbine, the aerodynamic torque of the wind is input through the carrier. The

equations of motion of the carrier then are:

$$m_c\ddot{x}_c + k_c x_c + \sum_{n=1}^{N} k_{p,n}\left[x_c - \xi_n \cos\psi_n + (\eta_n - u_c)\sin\psi_n\right] = 0 \tag{3.9}$$

$$m_c\ddot{y}_c + k_c y_c + \sum_{n=1}^{N} k_{p,n}\left[y_c - \xi_n \sin\psi_n + (\eta_n - u_c)\cos\psi_n\right] = 0 \tag{3.10}$$

$$\frac{I_c}{R_c^2}\ddot{u}_c + \sum_{n=1}^{N} k_{p,n}\left(-x_c \sin\psi_n + y_c \cos\psi_n + u_c - \eta_n\right) = \frac{T_{in}}{R_c} \tag{3.11}$$

where k_c is the carrier bearing stiffness in the translational direction, $k_{p,n}$ is the n^{th} planet bearing stiffness, and T_{in} is the torque caused by the wind which is discussed in section 3.3.

3.2.3 Ring Gear

The ring gear is the outer fixed internal gear which meshes with planetary gears. The ring gear is modeled as a smooth thin-walled ring connected to the frame through a certain number of bolt connections. Each bolt connection is modeled as three springs, namely $k_{sc,r}$, $k_{sc,\tau}$, and $k_{sc,\theta}$ (Figure 3.3a). Curved beam elements are used to discretize the ring with a typical element shown in Figure 3.3b. The stiffness and mass matrices of the ring are created by curved beam theory, and the meshes between the ring-planet pairs are considered as moving loads.

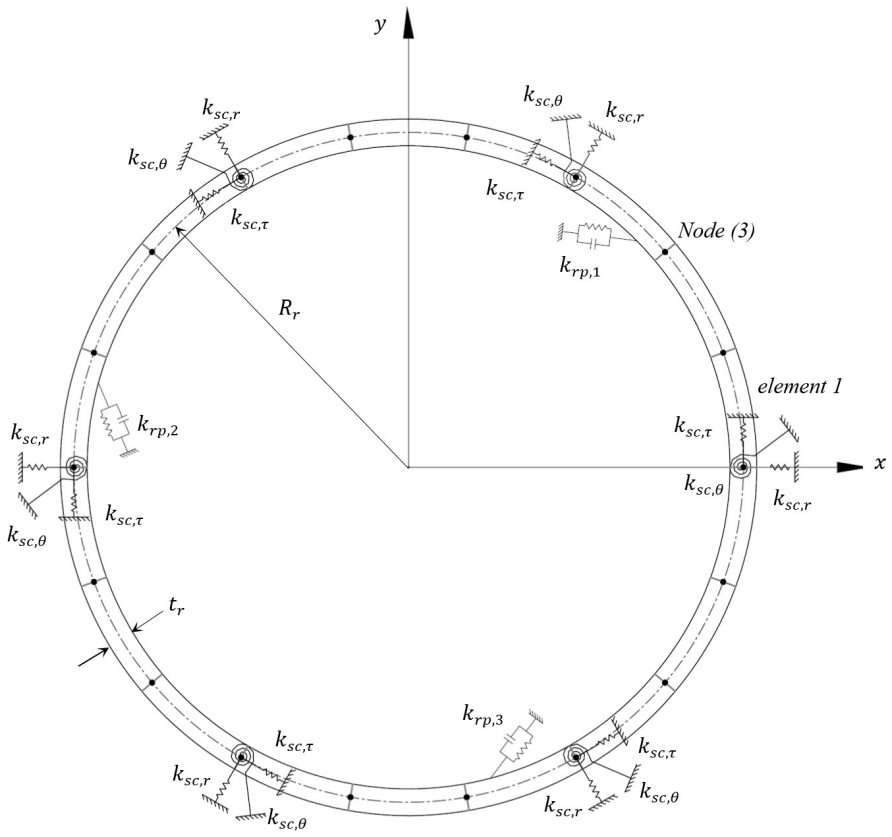

(a) A finite element model of the ring gear with six supports

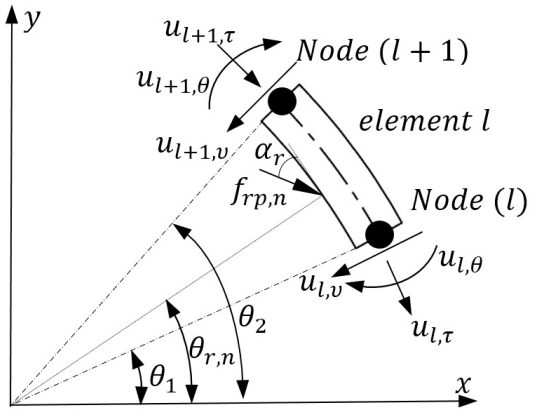

(b) A curved beam element under moving load

Figure 3.3: Ring gear model

3.2.3.1 Element Stiffness and Mass Matrices

The mass and stiffness matrices of an element are calculated based on reference [24]. The reference [24] used a curved beam for modeling arc structures, while this research applied the same method for modeling the ring gear. Here, we directly give the final equations, and details can be found in the reference paper and in Appendix 3.A.2.

$$[k_l] = \frac{\bar{E}I_l}{R_r^3}[D][B]^{-1} \qquad l = 1, 2, ...L \tag{3.12}$$

$$[m_l] = \rho R_r [B]^{-1^T} \int_{\theta_1}^{\theta_2} \left([H]^T [\Lambda] [H] \, d\theta \right) [B]^{-1} \qquad l = 1, 2, ...L \tag{3.13}$$

where k_l and m_l are the stiffness matrix and mass matrix of the l^{th} element, respectively, $\bar{E}$ and ρ are the elasticity module and the density of the ring material. θ_1 and θ_2 are the angular coordinations of the two nodes of the element, and D, B, Λ and H are matrices given in Appendix 3.A.2.

3.2.3.2 Moving Meshing Force f_{rp}

The ring gear of a PGT is subjected to vibration under multiple moving meshing forces, $f_{rp,n}$ $(n = 1, 2, ..., N)$, and due to the elastic behavior of the ring gear applying these moving loads on the model in a proper way is important. The ring gear is supported by six equally-spaced elastic supports while moving loads, caused by the planet-ring meshing pairs, rotate throughout the inside of the ring gear (see Figure 3.4). Each moving load is assumed to have a constant angular velocity, ω_c, and is at

a fixed angular distance $2\pi/N$ form its neighbors. The acting point of moving loads are:

$$\theta_{r,n} = \omega_c t + \frac{2\pi\,(n-1)}{N} \qquad\qquad n = 1, ..., N \tag{3.14}$$

where $\theta_{r,n}$ is the angular coordination of the nth moving load inside the ring gear. In the following, the process leads to the ring gear dynamic equation under moving meshes were presented.

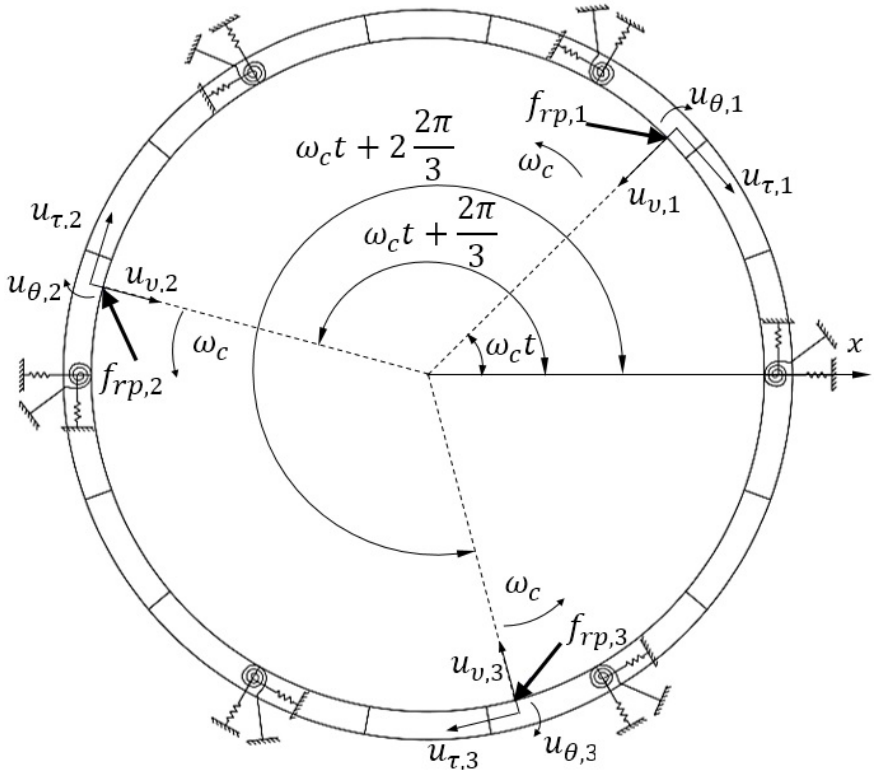

Figure 3.4: Ring gear under moving meshing loads of the planets.

To develop the ring gear dynamic equation under the moving load, the meshing

force in the rp mesh should be defined. Because backlash is considered the meshing force can be calculated by:

$$f_{rp,n} = \begin{cases} k\left(t\right)_{rp,n}\left(\delta_{rp,n} - b_{rp}\right), & \delta_{rp,n} \geq b_{rp} \\ 0, & -b_{rp} \leq \delta_{rp,n} \leq b_{rp} \\ k\left(t\right)_{rp,n}\left(\delta_{rp,n} + b_{rp}\right), & \delta_{rp,n} \leq -b_{rp} \end{cases} \tag{3.15}$$

where $k_{rp,n}$ is the stiffness between rp mesh, and $2b_{rp}$ is the total clearance between meshing teeth of the planet-ring pair, and $\delta_{rp,n}$ is the relative compression displacement and can be computed in a way similar to the sp mesh as follows.

$$\delta_{rp,n} = \xi_n \sin\alpha_r - \eta_n \cos\alpha_r - u_n + u_{\upsilon,n}\cos\alpha_r - u_{\tau,n}\sin\alpha_r \tag{3.16}$$

where $u_{\upsilon,n}$ and $u_{\tau,n}$ are the displacements in the radial and tangential direction at the contact point, respectively. Due to the moving of this contact point, we can translate the two displacements into that of the two nodes using the following shape function [24]:

$$u_{\upsilon,n} = G_1 + G_2\cos\theta_r + G_3\sin\theta_r + G_4\theta_r\sin\theta_r + G_6\theta_r\cos\theta_r \tag{3.17}$$

$$u_{\tau,n} = G_1\bar{A}\theta_r + G_2\sin\theta_r - G_3\left(\sin\theta_r - \theta_r\cos\theta_r\right) + G_5 + G_6\left(\cos\theta_r + \theta_r\sin\theta_r\right) \tag{3.18}$$

$$u_{\theta,n} = G_1\bar{A}R_r^{-1}\theta_r + 2G_4R_r^{-1}\sin\theta_r + G_5R_r^{-1} + 2G_6R_r^{-1}\cos\theta_r \tag{3.19}$$

In these equations, G_1 - G_6 are constants computed with the node displacements of the ring element in meshing with the planet. According to the shape functions

presented in Eqs. 3.17 to 3.19, the displacements of the nodes of l^{th} element, $\{u_l\}$, can be defined as:

$$\{u_\upsilon \quad u_\tau \quad u_\theta\}^T = \left[\bar{N}\right]\{u_{l,\upsilon} \quad u_{l,\tau} \quad u_{l,\theta} \quad u_{l+1,\upsilon} \quad u_{l+1,\tau} \quad u_{l+1,\theta}\}^T \tag{3.20}$$

where $[\bar{N}]$ is shape function matrix that can be found in Appendix 3.A.2. In addition, for FEM modeling, we need to transform the $f_{rp,n}$ into its equivalent node forces as:

$$f_l = \begin{bmatrix} \bar{N}_{11} & \bar{N}_{12} & \dots & \bar{N}_{16} \\ \\ \bar{N}_{21} & \bar{N}_{22} & \dots & \bar{N}_{26} \end{bmatrix}^T \begin{Bmatrix} -f_{rp,n}\sin\alpha_r \\ \\ f_{rp,n}\cos\alpha_r \end{Bmatrix} \tag{3.21}$$

In Eq. 3.21, $\bar{N}_{i,j}$ is the component of the shape function matrix and f_l is the transformed node force array caused by moving mesh and defined as:

$$f_l = \begin{Bmatrix} f_{r1} & f_{\tau 1} & M_1 & f_{r2} & f_{\tau 2} & M_2 \end{Bmatrix}^T \tag{3.22}$$

Due to the movement of the planet through the ring gear, the value of f_l varies with time, and this transformed node force would be zero for the elements without applied moving mesh. The governing equation of the element by considering the effect of moving mesh can be represented as:

$$[m_l]\{\ddot{u}_l\}+[k_l]\{u_l\}=\{f_l\}\hat{\delta}\left(\theta_{r,n}-\frac{2\pi(l-1)}{L}-\omega_c t\right) \quad n=1,...,N \;\; l=1,...,L \tag{3.23}$$

where ω_c is the carrier angular velocity, and $\hat{\delta}$ is the Dirac delta function. The global

dynamic equation of the entire ring is obtained by assembling the elements and then applying the boundary conditions.

$$[M_l]\{\ddot{U}_l\} + [K_l + K_{sc}]\{U_l\} = \{F_r\} \tag{3.24}$$

where M_l is the global mass matrix of the ring, K_l is the global stiffness matrix of the ring, K_{sc} is the supports' stiffness matrix, U_l is the global displacement of the ring, and F_r is the applied moving mesh forces vector. K_{sc} and F_r can be found in Appendix 3.A.3.

3.2.4 Planet Gear

The planet gears are held by the carrier, and they mesh with both the sun gear and the ring gear. With the rp meshing force $f_{rp,n}$, the governing equations of the motion of a planet can be represented as:

$$m_p\ddot{\xi}_n + k_p\xi_n - f_{sp,n}\sin\alpha_s + f_{rp,n}\sin\alpha_r - k_{p,n}\left(x_c\cos\psi_n + y_c\sin\psi_n - \xi_n\right) = 0 \tag{3.25}$$

$$m_p\ddot{\eta}_n + k_p\eta_n - f_{sp,n}\cos\alpha_s - f_{rp,n}\cos\alpha_r - k_{p,n}\left(x_c\sin\psi_n + y_c\cos\psi_n + u_c - \eta_n\right) = 0 \tag{3.26}$$

$$\frac{I_p}{R_p^2}\ddot{u}_n + f_{sp,n} - f_{rp,n} = 0 \tag{3.27}$$

3.3 Wind Torque

The input torque is placed on the carrier, as in the case of wind turbine PGTs, and wind is the source of the input torque. The wind speed can be split into two parts, namely the mean wind velocity, V_0, which is deterministic, and the turbulence, V_t, which is random. Then the torque generated by the wind can be calculated by [20]:

$$T_{in} \approx \underbrace{\frac{1}{2}\rho_a A_b R_b \frac{C_p}{\lambda_0} V_0^2}_{T_d\ deterministic\ part} + \underbrace{\rho_a A_b R_b V_0 \frac{C_p}{\lambda_0} V_0 V_t}_{T_r\ Random\ part} \tag{3.28}$$

where ρ_a is the air density, A_b is the swept area of the rotor, R_b is the rotor radius, C_p is the power coefficient, and λ_0 is the tip speed ratio defined as:

$$\lambda_0 = \frac{\omega_{r0} R_b}{V_0} \tag{3.29}$$

where ω_{r0} is the rotation speed of the rotor. The random turbulence in this paper is modeled based on the Von Karman spectrum, which is implemented in the dynamic model through the following filter [20, 25].

$$V_t = \sigma_t \left(k_v \chi + k_v T_v a_1 \dot{\chi}\right) \tag{3.30}$$

$$a_2 T_v^2 \ddot{\chi} + \left(a_2 T_v + T_v\right) \dot{\chi} + \chi = W\left(t\right) \tag{3.31}$$

where $W(t)$ is white noise, a_1 and a_2 are two constant values which are 0.4 and 0.25, respectively, χ is the variable associated with the filter, and $T_v = l_t/V_o$ where σ_t is the intensity of turbulence, and l_t is the length of the turbulence.

3.4 Statistical Linearization

In this paper, backlash between the sun-planets pair and ring-planets pair are considered and statistical linearization is applied to both. $f_{sp,n}$ and $f_{rp,n}$ are strongly nonlinear functions of the general coordinates due to the backlash as shown in Eqs. 3.5 and 3.15. These nonlinear equations are first approximated with linear equations through the stochastic linearization technique [26]. Paper [26] used SL for a fixed center gear model in which gears relative displacements affect form only gear rotational; this research used the SL method for planetary gear in which gears relative displacements affect from rotational, transnational, and elastic displacements of gears. In the following section, steps are provided for the linearization which is mainly based on [27]. A nonlinear function of a general backlash type is expressed as:

$$f(x) = \begin{cases} k(x-b), & x \geq b \\ 0, & -b \leq x \leq b \\ k(x+b), & x \leq -b \end{cases} \tag{3.32}$$

where x represents the relative displacement ($\delta_{sp,n}$ or $\delta_{rp,n}$) and b is a general expression of the clearance. A linear function, $f_e(x)$ in the following form is sought.

$$f_e(x) = k_e\hat{x} + f_0 \tag{3.33}$$

where k_e is an equivalent stiffness, f_0 denotes the original shift, and $\hat{x}$ is the zero-mean displacement defined as $\hat{x} = x - E(x)$ where $E()$ indicates the mean operation. The difference between Eqs. 3.32 and 3.33 is:

$$\varepsilon = f(x) - k_e(x - E(x)) - f_0 \tag{3.34}$$

To minimize ε in the stochastic sense, the following two conditions should be met.

$$\frac{\partial E\left(\varepsilon^2\right)}{\partial k_e} = 0 \tag{3.35}$$

$$\frac{\partial E\left(\varepsilon^2\right)}{\partial f_0} = 0 \tag{3.36}$$

This leads to the following two relations if it is assumed that the responses follow the Gaussian distribution.

$$k_e = E\left[\frac{\mathrm{d}f}{\mathrm{d}x}\right] \tag{3.37}$$

$$f_0 = E\left[f(x)\right] \tag{3.38}$$

Finally, after taking expectation of gradient of the nonlinear function (f), k_e and f_0 can be reached as:

$$k_e = \frac{k}{2}\left[2 + erf\left(V_1\right) - erf\left(V_2\right)\right] \tag{3.39}$$

$$f_0 = k\mu - \frac{\sigma k}{\sqrt{2\pi}}\left(e^{-V_1^2} - e^{-V_2^2}\right) - \frac{k\mu}{2}\left[erf\left(V_2\right) - erf\left(V_1\right)\right] + \frac{kb}{2}\left[erf\left(V_1\right) + erf\left(V_2\right)\right] \tag{3.40}$$

where σ and μ are the standard deviation and the mean of x, respectively. V_1 and V_2 are two variables defined by:

$$V_1 = \frac{-b - \mu}{\sqrt{2}\sigma} \tag{3.41}$$

$$V_2 = \frac{b - \mu}{\sqrt{2}\sigma} \tag{3.42}$$

3.4.1 Overall Linearized Equation

The aforementioned statistical linearization method is applied to nonlinear dynamics equations (Eqs. 3.5 and 3.15) and then combining Eqs. 3.6−3.11, 3.24, 3.25−3.27, 3.28, 3.30, and 3.31 and inserting the damping will give the linear dynamic equation of the whole system. It can be presented in a matrix form as:

$$[M]\left\{\ddot{U}\right\} + [C]\left\{\dot{U}\right\} + [K_e]\{U\} = F_d + W\left(t\right) - F_e \tag{3.43}$$

where $[M]$, $[C]$,and $[K_e]$ are the overall mass, damping, and equivalent stiffness matrix respectively, and F_d, and F_e are the deterministic load and the load generated by stochastic linearization, respectively. Their entries can be found in the Appendix 3.A.3. U is the overall generalized coordinate vector expressed as follows:

$$\{U\} = \{\underbrace{x_s \quad y_s \quad u_s}_{\text{sun}} \quad \underbrace{\xi_1 \quad \eta_1 \quad u_1}_{\text{planet1}} \quad \cdots \quad \underbrace{\xi_N \quad \eta_N \quad u_N}_{\text{planet N}} \quad \underbrace{x_c \quad y_c \quad u_c}_{\text{carrier}}$$

$$\underbrace{u_{1,\upsilon} \quad u_{1,\tau} \quad u_{1,\theta}}_{\text{node 1}} \quad \cdots \quad \underbrace{u_{L+1,\upsilon} \quad u_{L+1,\tau} \quad u_{L+1,\theta}}_{\text{node L+1}} \quad \underbrace{\chi}_{\text{filter}}\} \tag{3.44}$$

3.5 Solution procedure

Different numerical methods were introduced to solve the MDOF dynamic model which is subjected to both deterministic and random excitation. In this paper, the stochastic Newmark [28] algorithm is used to solve Eq. 3.43. In this algorithm, the time is first discretized into many short time intervals and Eq. 3.43 is recast into the state space form as below.

$$\{Y_{i+1}\} = [T_1]\{Y_i\} + [T_2]\{H_i\} + [T_3]\{W_i\} \tag{3.45}$$

The elements in this equation are given as:

$$\{Y_i\} = \begin{Bmatrix} U_i \\ \dot{U}_i \end{Bmatrix} \tag{3.46}$$

$$[T_1] = \begin{bmatrix} C_e + \frac{\Delta t}{2} K_e & M \\ M & -M\frac{\Delta t}{2} \end{bmatrix}^{-1} \begin{bmatrix} C_e - \frac{\Delta t}{2} K_e & M \\ M & M\frac{\Delta t}{2} \end{bmatrix} \tag{3.47}$$

$$[T_2] = \begin{bmatrix} C_e + \frac{\Delta t}{2} K_e & M \\ M & -M\frac{\Delta t}{2} \end{bmatrix}^{-1} \begin{bmatrix} \frac{\Delta t}{2} & \frac{\Delta t}{2} \\ 0 & 0 \end{bmatrix} \tag{3.48}$$

$$[T_3] = \begin{bmatrix} C_e + \frac{\Delta t}{2} K_e & M \\ M & -M\frac{\Delta t}{2} \end{bmatrix}^{-1} \begin{bmatrix} \sqrt{\Delta t B} & 0 \\ 0 & B\frac{\Delta t\sqrt{\Delta t}}{\sqrt{12}} \end{bmatrix} \tag{3.49}$$

$$\{H_i\} = \begin{Bmatrix} F_i \\ F_{i+1} \end{Bmatrix} \tag{3.50}$$

$$\{W_i\} = \begin{Bmatrix} N_i \\ P_{i+1} \end{Bmatrix} \tag{3.51}$$

where $(N_i; P_i)$ is an independent standard Gaussian random variable and the subscript i means the i^{th} time instant. Due to the deterministic load, the mean response of the system is not zero, which can be obtained through taking the ensemble average of Eq. 3.45.

$$\langle Y_{i+1} \rangle = T_1 \langle Y_i \rangle + T_2 \langle H_i \rangle \tag{3.52}$$

where $\langle\rangle$ represents the ensemble average. To determine the correlation matrix, multiplying Eq. 3.45 with its transposition, and then taking the ensemble average gives:

$$[R_{i+1}] = [T_1][R_i][T_1]^T + [T_2][B_1][T_2]^T + [T_3][B_2][T_3]^T + [T_1][B_3][T_2]^T + [T_2][B_3]^T[T_1]^T \tag{3.53}$$

where $[R_i] = \langle Y_i Y_i^T \rangle$, $[B_1] = \langle E_i E_i^T \rangle$, $[B_2]$ is a unity matrix, and $[B_3] = \langle Y_i \rangle E_i$.

3.6 Monte Carlo simulations

Monte Carlo simulations [29] were carried out to verify the obtained results by using the statistical linearization method for PGT with an elastic ring under random excitation. Assembling the PGT motion equations and taking the backlash nonlinearity into account, the governing equation of the nonlinear stochastic dynamic equation of PGT takes the following form:

$$[M]\{\ddot{U}\} + [C]\{\dot{U}\} + \{\bar{f}(t,U)\} = F_d + W(t) \tag{3.54}$$

where $\bar{f}(t,U)$ is the vector of nonlinear functions. To perform the MCS in this research, initially, the white noise excitation that was applied to the system through Eq. 3.31 was discretized into time steps, Δt. Therefore, a series of independent and identically distributed random variables, Γ, was generated by using Matlab software to represent the white noise. The variables have zero mean and variance, $\sigma_\Gamma^2 = 2\pi S_0/\Delta t$, where S_0 is the white noise spectral density. The variable Γ is given as:

$$\Gamma = \sqrt{\frac{2\pi S_0}{\Delta t}}\gamma \tag{3.55}$$

where γ is an independent and identically distributed random number. Each of these random variables (Γ) were substituted into the nonlinear dynamic model, and then the deterministic solution was performed on Eq. 3.54. After a sufficient set of simulations that could determine the accuracy of the MCS results, the response statistics were

computed from an ensemble of responses.

3.7 Simulation and Result Analysis

The simulations were carried out using MATLAB software to evaluate the PGT of a wind turbine. Throughout the simulations, the mean of wind speed assumed 16 km/h, and the mechanical parameter values of the PGT of wind turbines with 50 m tower height are provided in Table 3.1[30], and the material properties and system parameters are provided in Table 3.2. The ring is divided into 18 curved beams, with six equally-spaced supports on the ring gear. The number of planets and supports considered were three and six, respectively. In this case, because the number of the sun gear teeth and ring gear teeth are integer multiple of the number of planets, the phase shift of all sun-planet pair meshes equal to zero ($\Omega_{sp,n} = 0, n = 1, 2, 3$), and the phase shift of all the ring-planet meshes equal to zero ($\Omega_{rp,n} = 0, n = 1, 2, 3$).

Table 3.1: Planetary gear transmission parameters

	Sun	Planet	Ring	Carrier
Teeth number	21	39	99	-
Mass (kg)	181.6	104	-	759.9
Moment of inertia (kg.m^2)	3.2	3.2	-	59.1
Pitch diameter (mm)	215.6	400.4	1016.4	-
Bearing stiffness (N/m)	100	6.8×10^9	-	5×10^9
Torsional stiffness (Nm/rad)	45.8×10^6	-	-	-
Mesh stiffness average (N/m)	$\bar{k}_{sp} = 16.9 \times 10^9$, $\bar{k}_{rp} = 19.2 \times 10^9$			
Pressure angle (°)	$\alpha_s = 20$, $\alpha_r = 20$			

Table 3.2: Material properties and system parameters

Parameter	Value	Parameter	Value
b (μm)	100	ρ (kg/m^3)	7800
$\bar{E}$ (GPa)	210	ω (rad/s)	22.990
$\bar{G}$ (GPa)	79.3	ω_c (rad/s)	0.2322
k_r(N/m)	1.362×10^{10}	$\bar{c}_s$	1.6
k_τ(N/m)	1.362×10^{10}	$\bar{c}_r$	1.5
k_θ(N.m/rad)	5.146×10^9	Ω_{sr}	0.25
T_m(s)	0.2733		

Using the simulation results, the mean and the mean square of all generalized coordinates are analyzed. Also, to determine the accuracy of the proposed linearized model, Monte Carlo simulations were carried out, and the results were compared. In this study, according to the required accuracy and system complexity, 100,000 simulations with time step $\Delta t = 0.0027$ s and $S_0 = 1$ were carried out, and comparisons of the obtained results from SL and the Monte Carlo simulations were given. Then, the effect of elastic ring gear on meshing forces, the sun-planet, and the ring-planet pairs were analyzed. A parametric study was conducted based on the simulation to study the effect of a ring gear's rim wall thickness on the dynamic response of the PGT.

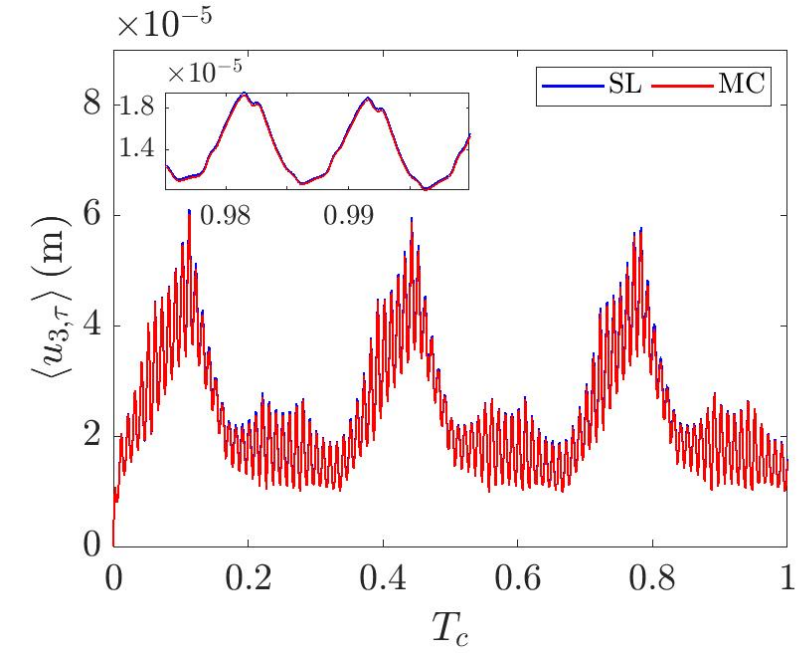

(a) Mean of displacement

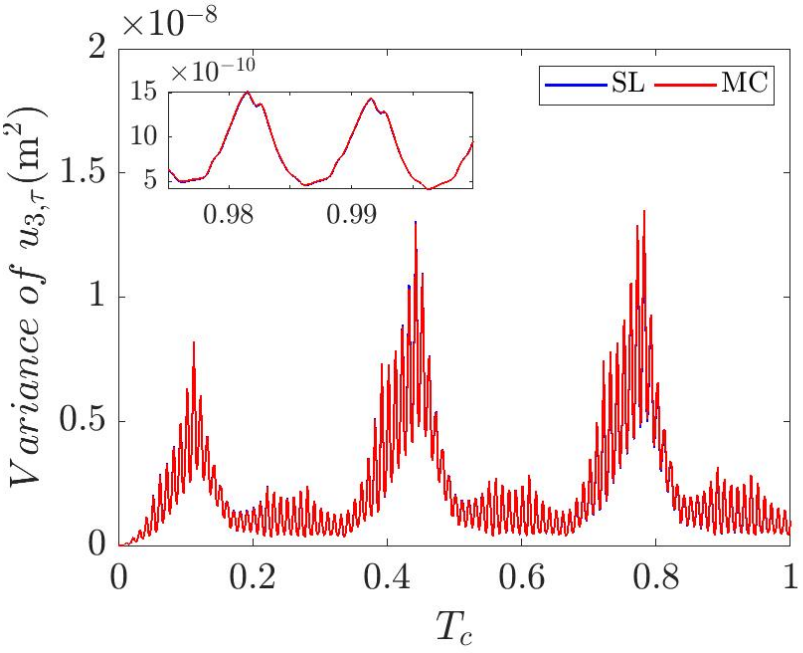

(b) Variance of displacement

Figure 3.5: Displacement of Node (3) at τ direction (the blue line represents the statistical linearization, and the red line represents the Monte Carlo simulations)

3.7.1 Dynamic Responses

In this section, Monte Carlo simulations are used to verify the accuracy of the presented model and solution method. The mean and variance of the displacement of the ring gear' node, planet gear, sun gear, and carrier are compared with the MCS results. In this section, for brevity, only the response of one specific direction of each component is presented in following.

The results generated by the MCS for node 3 were identical to results of the linearized model (Figure 3.5). The mean and variance of displacement responses of nodes 3 at tangential direction are shown in Figure 3.5. The positions of the nodes are shown in Figure 3.3a where T_c is the period of the carrier. The figure shows that both the gear meshing frequency and the planet frequency are presented in the response. Three peaks show the planet frequency in one carrier period. In addition, based on the obtained results from the linearized model and MCS, both methods agree well. It should be noted that the number of elements affects the phase difference in response of the nodes, and in this study, the phase difference between every two adjacent nodes was $\frac{1}{18}$ carrier period.

The results obtained by the MCS for sun gear, carrier, and planet gear were near identical to the results of the linearized model (Figures 3.6-3.8). The mean and variance of displacement responses of the sun gear and the carrier at the rotational direction are shown in Figures 3.6 and 3.7. Comparisons with Monte Carlo simulations demonstrated that the obtained results from the linearized model are in good

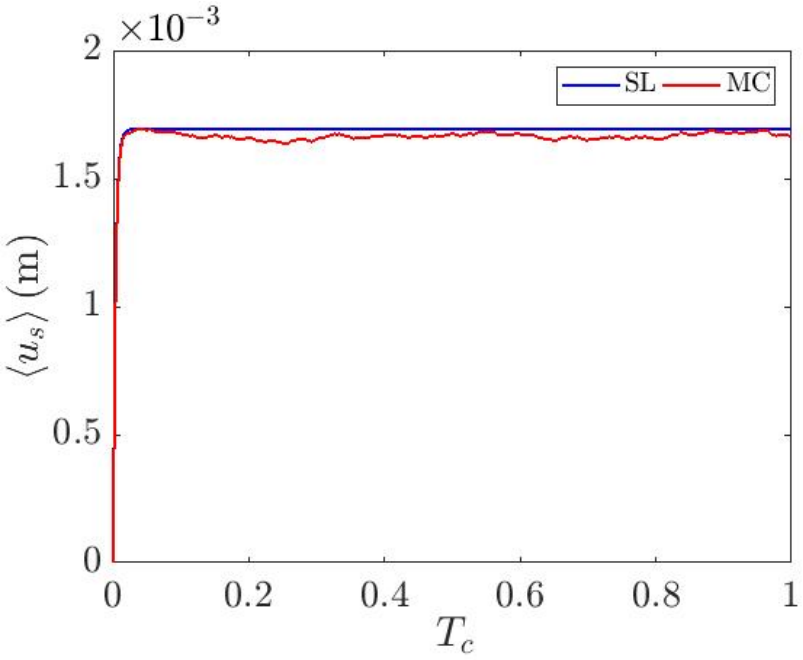

(a) Mean of displacement

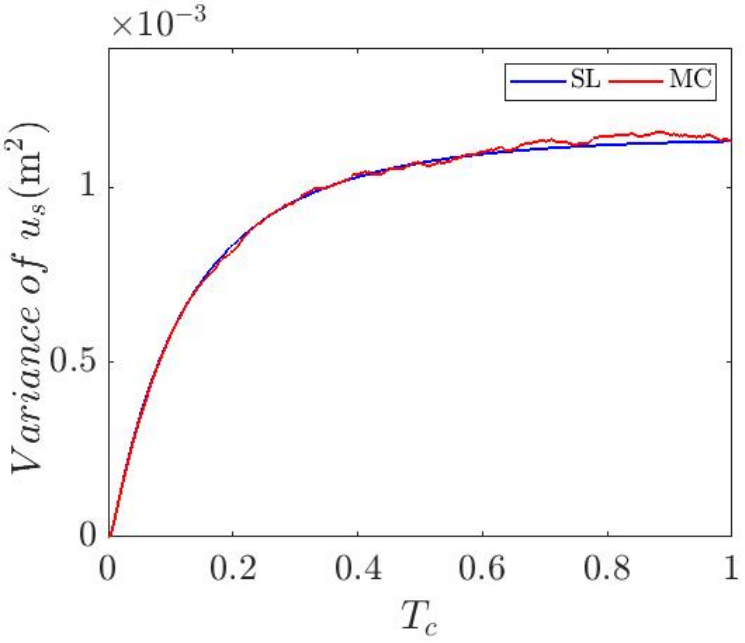

(b) Variance of displacement

Figure 3.6: Displacement of sun gear at θ direction (the blue line represents the statistical linearization, and the red line represents the Monte Carlo simulations)

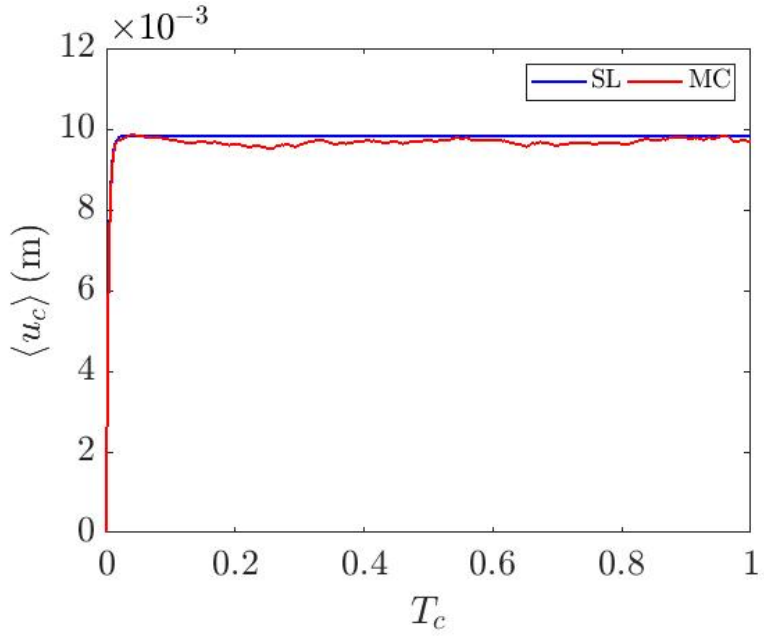

(a) Mean of displacement

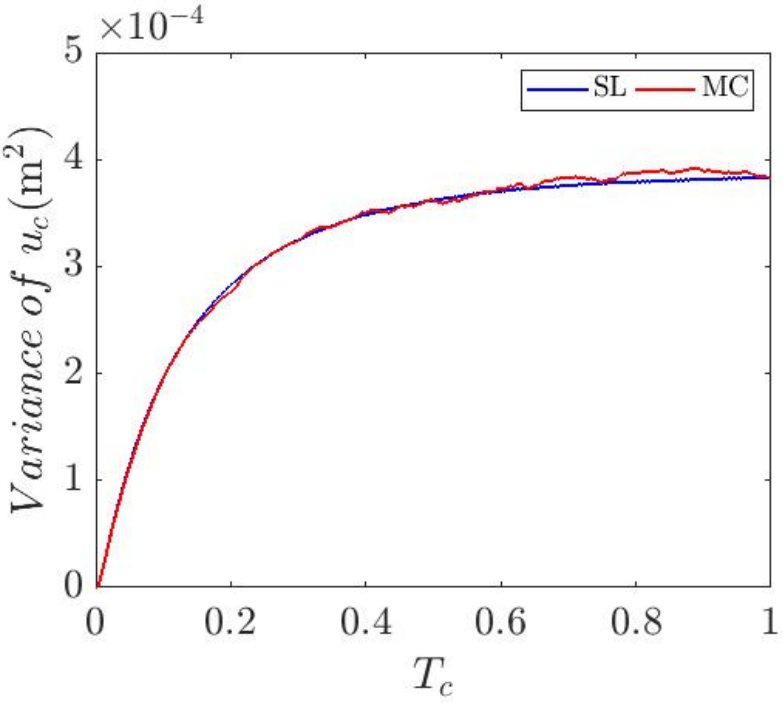

(b) Variance of displacement

Figure 3.7: Displacement of carrier at θ direction (the blue line represents the statistical linearization, and the red line represents the Monte Carlo simulations)

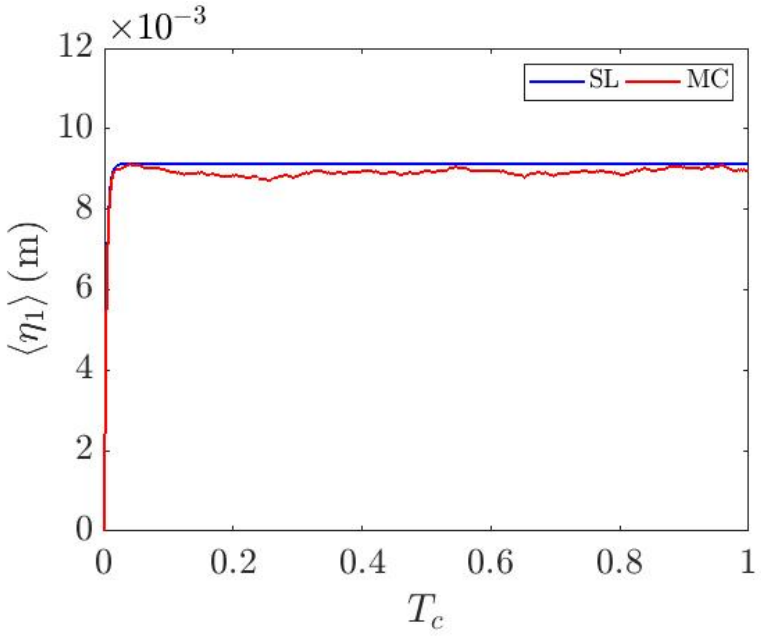

(a) Mean of displacement

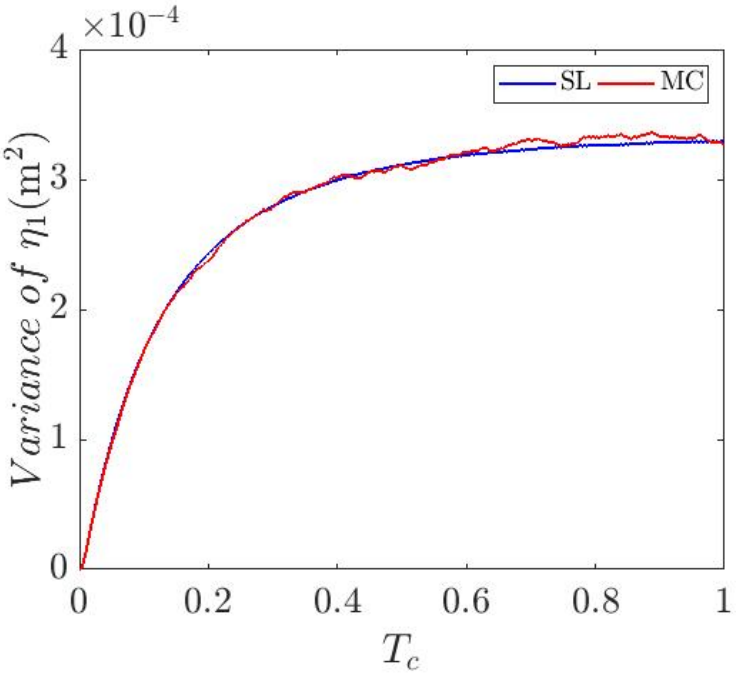

(b) Variance of displacement

Figure 3.8: Displacement of planet at η direction (the blue line represents the statistical linearization, and the red line represents the Monte Carlo simulations)

agreement with the MCS. The mean and variance of displacement responses of the planet gear at η direction are shown in Figure 3.8, and both the linearized model and MCS are in good agreement.

For computational time, the comparison revealed that MCS required much more computational time than SL because in MCS the most accurate results were obtained running numerous simulations. The MCS requested 223 hours of CPU time to process 100,000 simulations, while SL needed only 48 seconds of CPU time to perform the same function on the same computer (CPU i7-8700 3.2GHz/16GB RAM). This proved that the SL method increased the computational efficiency of stochastic nonlinear dynamic analysis of PGTs.

3.7.2 Ring gear deformation under moving meshes

Ring gear displacement under a moving meshing force, caused by the movement of the planet throughout the inside of the ring gear, is presented. The moving meshing forces traverse the ring gear for one rotation cycle in a time equal to the carrier period. Mean and standard deviation of displacement of the contact point of the ring gear and planet 1 with angular velocity $\omega_c = 0.2322$ rad/s are shown in Figure 3.9. Ring gear displacement caused by other planets is the same with a 1/3 period phase difference. Both the mean and mean square of displacement undergo six cycles in one carrier period, and this is because of elastically supported ring gear having six equally-spaced supports. From the figure, it is evident that the elastic supports have a

significant effect on dynamic responses, and the displacement decreased significantly when the meshing load approached the supports.

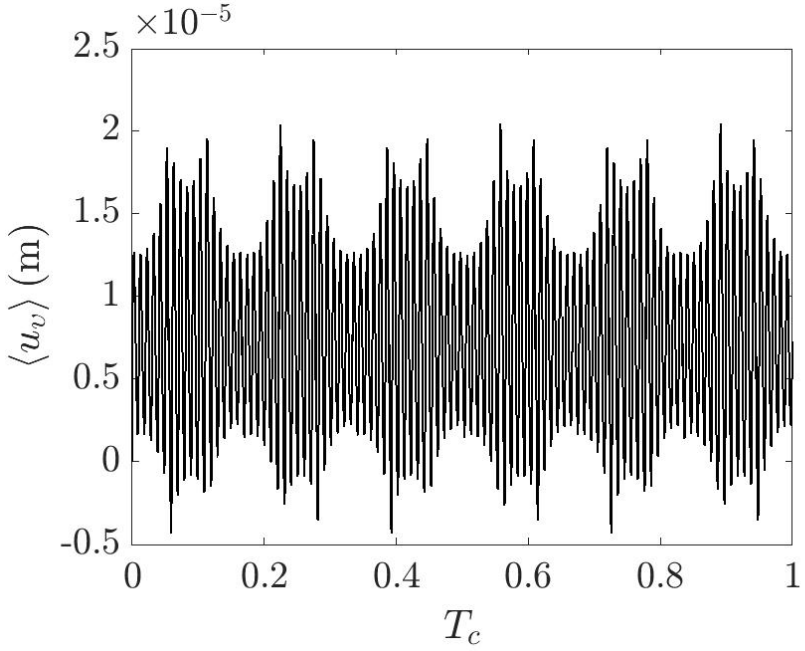

(a) Mean value of displacement

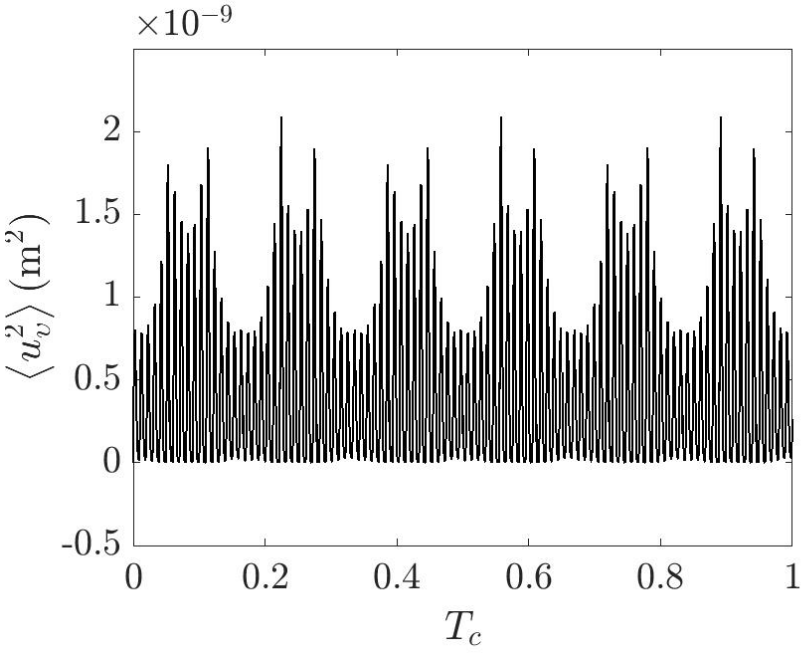

(b) Mean square value of displacement

Figure 3.9: Displacement of ring gear due to the moving meshing load of planet 1, $f^e_{rp,1}$.

3.7.3 Equivalent linear meshing loads

In this section, the equivalent linear meshing forces obtained from the statistical linearization process in section 3.4 are presented. The mean of the equivalent linear meshing forces in both the sun-planet and the ring planet pairs can be obtained by taking the ensemble average from Eq. 3.33. The mean squares are computed by first multiplying Eq. 3.33 by its transposition and then calculating the average.

For both the sun-planet and the ring-planet pairs meshes, only one pair is presented and there is only one phase difference between the adjacent pairs. The equivalent linear meshing load results for the sun-planet and the ring-planet pairs are provided in Figures 3.10 and 3.11, respectively. In both cases, the meshing frequency caused by the time-varying meshing stiffness was recorded. In any ring-planet pair, the lower frequency is always equal to the chosen number of supports; in this study, the lower frequencies are equal to six, matching the number of supports. However, in the sun-planet pair, a lower frequency is not recorded because the sun-planet mesh was not directly connected to the ring.

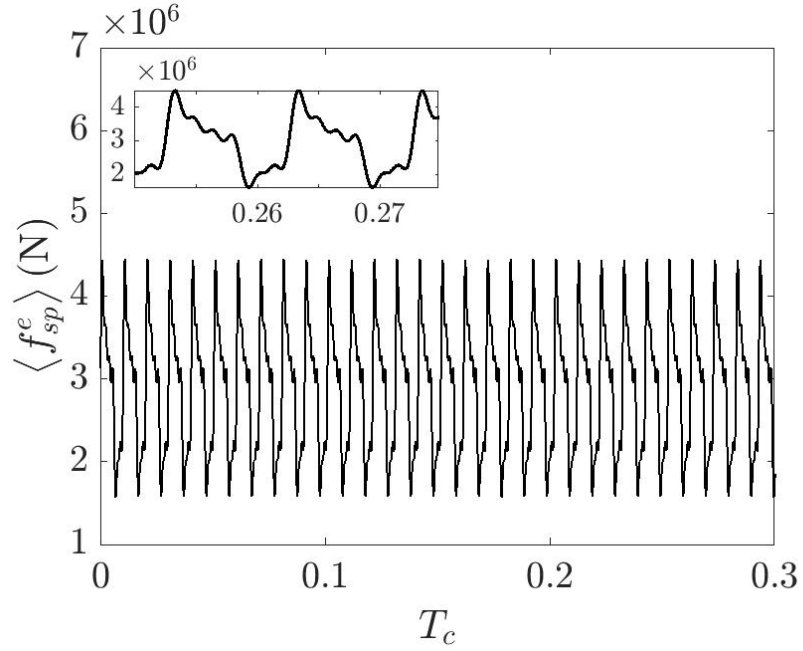

(a) Mean value of meshing force

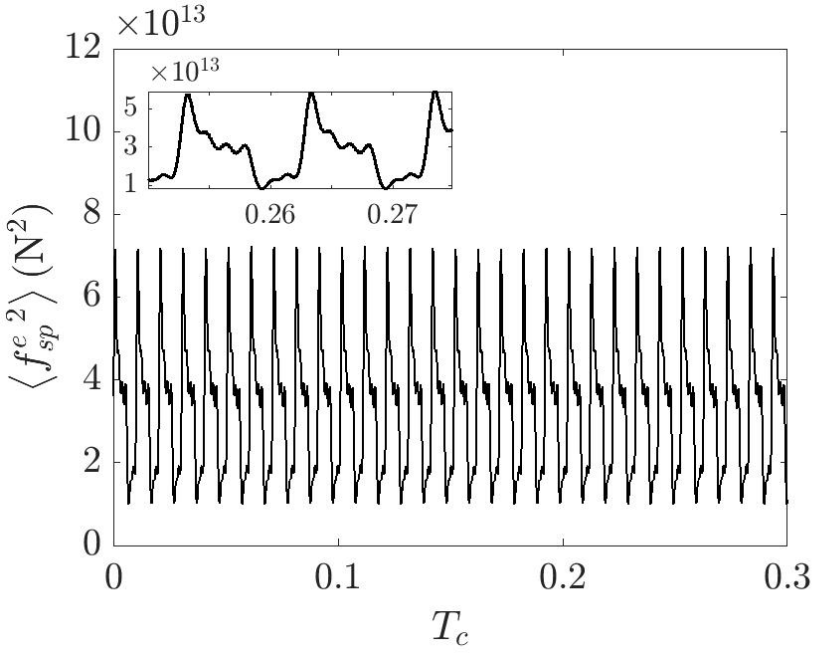

(b) Mean square value of meshing force

Figure 3.10: Equivalent linear meshing force between the sun-planet pair

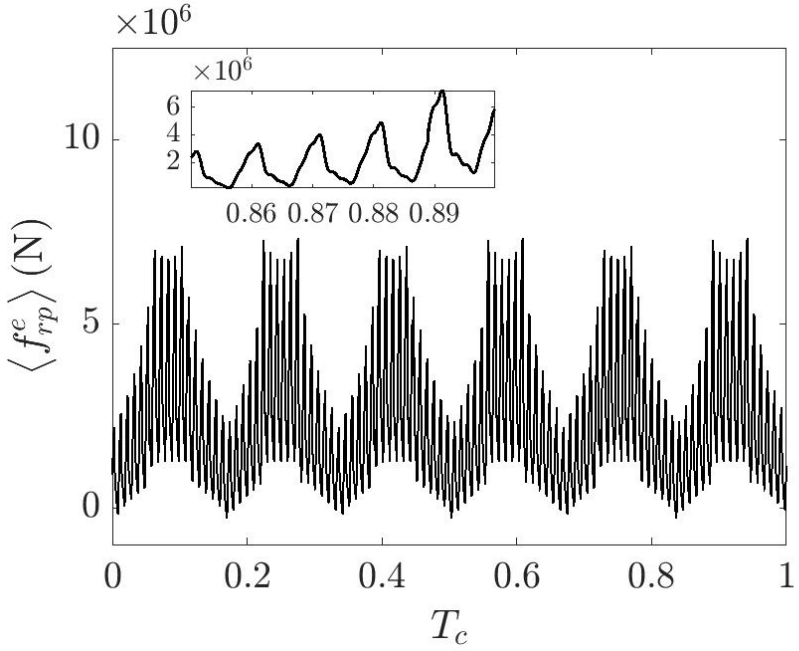

(a) Mean value of meshing force

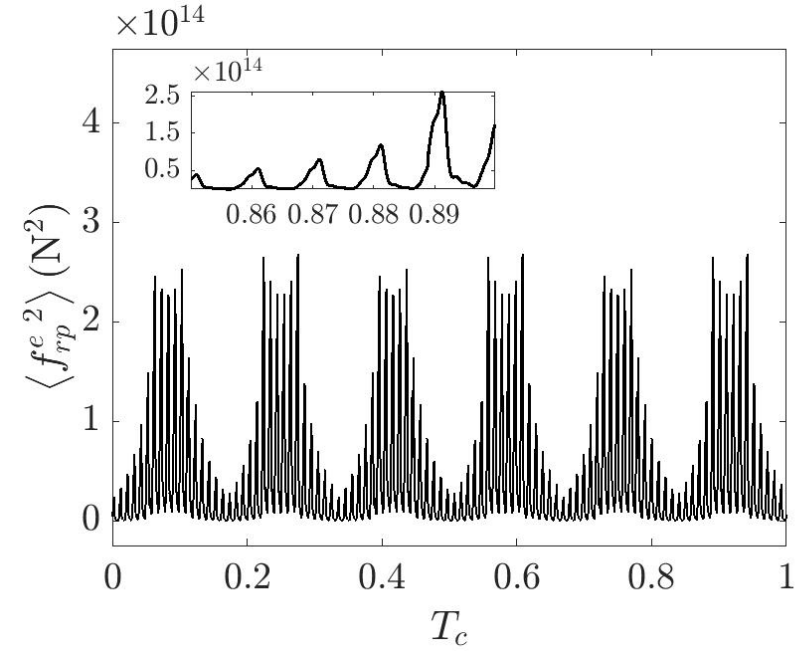

(b) Mean square value of meshing force

Figure 3.11: Equivalent linear meshing force between the ring-planet pair

3.7.4 Influence of rim thickness of ring gear

It is apparent that the elastic deformation of the ring gear has a significant effect on the dynamic response of the components of the PGT. There is a tendency to make the rim as thin as possible in the interest of making the weight of the PGT lighter. To verify this effect, three different wall thicknesses, t_{r1}=87 mm, t_{r2}=128 mm, and t_{r3}=168 mm, were used to calculate the responses.

First, the mean and the mean square values of the node (3) on the ring gear were examined and the results are shown in Figure 3.12. It was discovered that whenever the thickness was increased, the response decrease. This response was expected because a thicker rim generates a higher stiffness.

Secondly, the responses of the sun, planet and the carrier were observed using the model simulation, and the results are given in Figures 3.13−3.15, respectively. For the planet and the carrier, the rim thickness increased, the responses slightly decreased. However, any effect on the sun gear was negligible, possibly because the sun is under the action of three planets simultaneously, and the effects of the planets on the sun gear may have canceled each other out. Thus, it appears that the elasticity of the ring has little effect on the response of the sun gear.

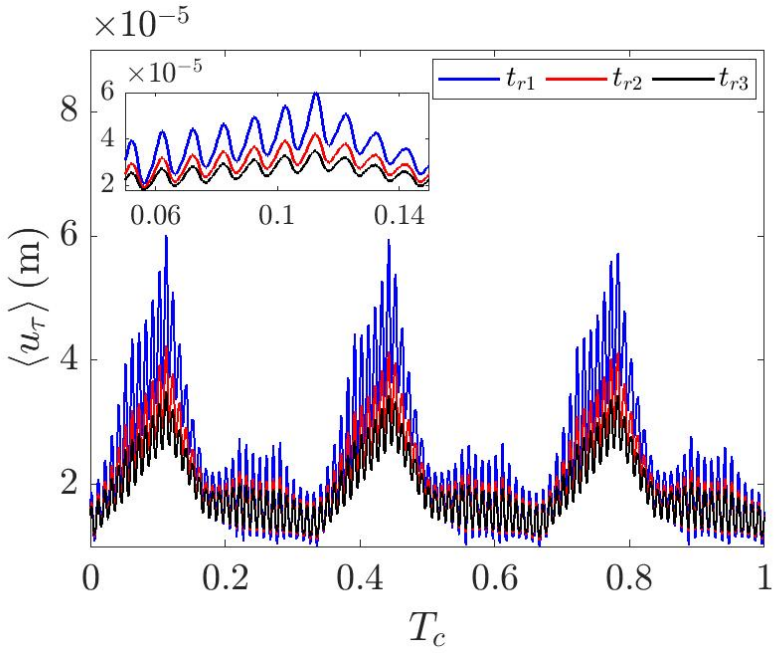

(a) Mean value of displacement

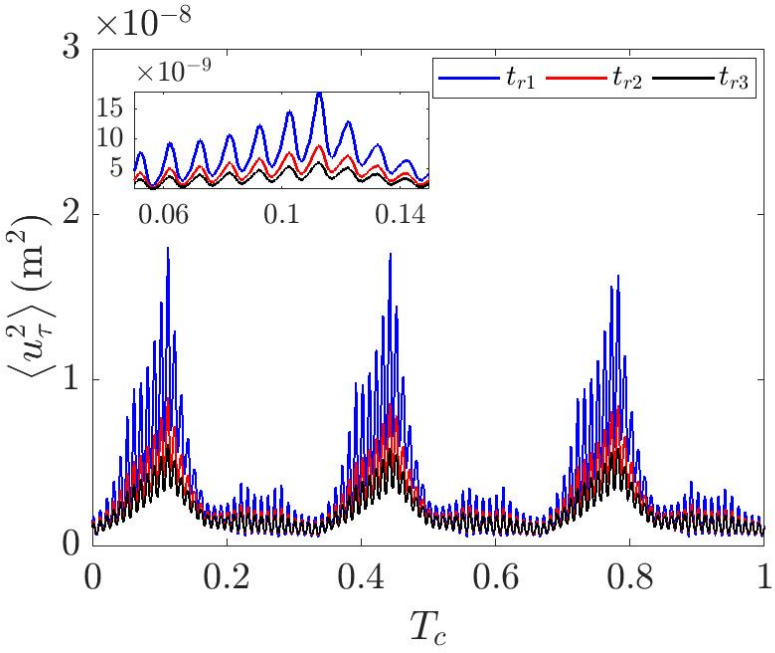

(b) Mean square value of displacement

Figure 3.12: Displacement of Node (3) (t_{r1}=87 mm, t_{r2}=128 mm, t_{r3}=168 mm)

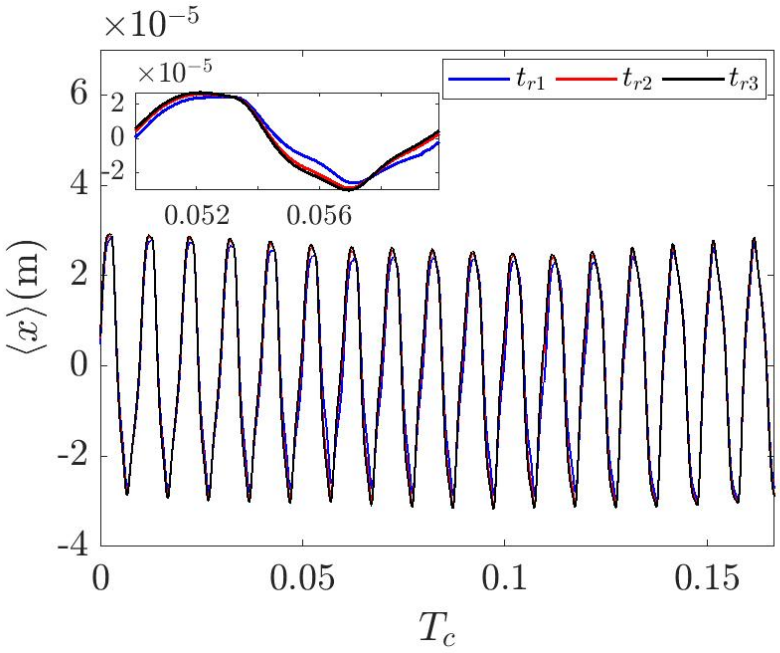

(a) Mean value of displacement

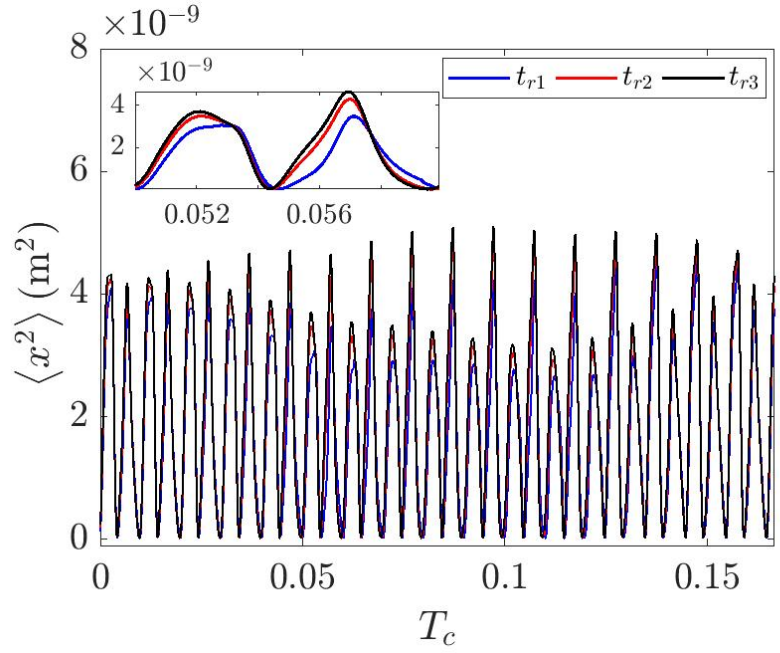

(b) Mean square value of displacement

Figure 3.13: Displacement of sun gear in the x direction (t_{r1}=87 mm, t_{r2}=128 mm, t_{r3}=168 mm)

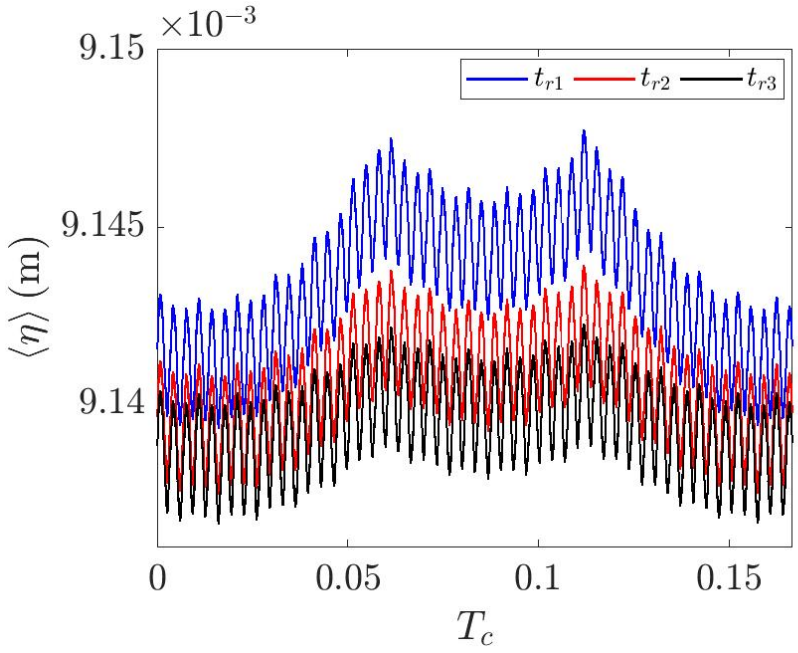

(a) Mean value of displacement

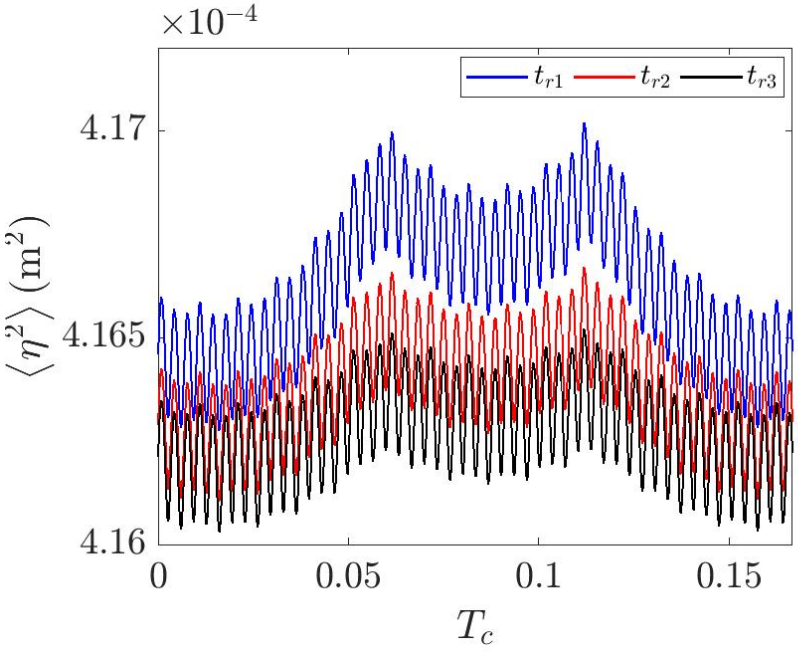

(b) Mean square value of displacement

Figure 3.14: Displacement of planet gear in the η direction (t_{r1}=87 mm, t_{r2}=128 mm, t_{r3}=168 mm)

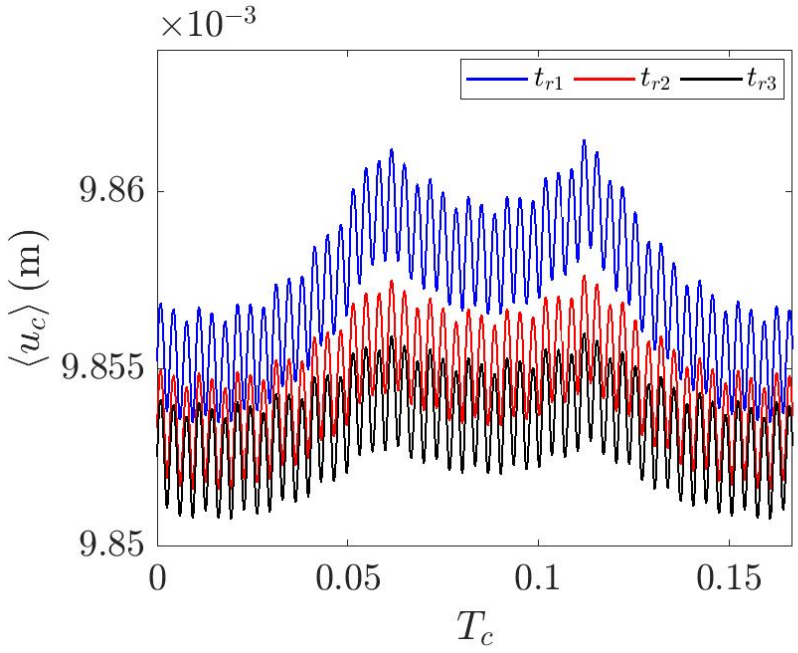

(a) Mean value of displacement

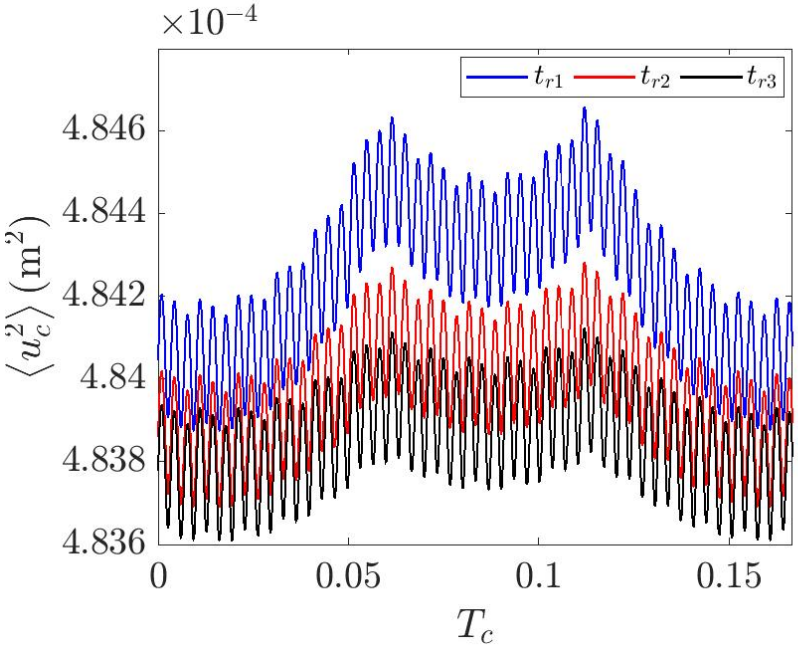

(b) Mean square value of displacement

Figure 3.15: Displacement of carrier in the rotational direction (t_{r1} =87 mm, t_{r2} =128 mm, t_{r3} =168 mm)

3.8 Conclusion

This paper analyzed the stochastic dynamics of the PGT of wind turbine with elastic ring gear. Time-varying mesh stiffness and the backlash nonlinearity between meshing gears were considered. In this paper, the ring was modeled as continuous, and all other components were treated as lumped-parameter models. Statistical linearization was used to handle nonlinearity, and then the random Newmark method was used to solve the equations. Monte Carlo simulations were then conducted to verify the proposed model and the linearization method.

This paper discovered that the statistical linearization method is accurate enough to study the nonlinear stochastic PGT in wind turbines, and the MCS results verified the accuracy of the method. In addition, the rim thickness of the ring gear had a significant effect on the dynamic responses of the ring gear itself; however, the effect was weak on the dynamic response of the carrier, planet gear, and sun gear.

The method used to connect the ring to the frame also had a significant effect on the dynamic responses of the ring gear and the gear meshing force. The ring-planet meshing forces, in particular, were affected by the number of the supports. However, the interaction between the number of supports and the number of planets was not examined in this paper.

3.A Appendix

3.A.1 Fourier series' harmonic coefficients

$$p_{sp,n}^{(j)} = \frac{-2}{j\pi} sin(j\pi(\bar{c}_s - 2\Omega_{sp,n}))sin(j\pi\phi_s) \tag{3.56}$$

$$q_{sp,n}^{(j)} = \frac{-2}{j\pi} cos(j\pi(\bar{c}_s - 2\Omega_{sp,n}))sin(j\pi\phi_s) \tag{3.57}$$

$$p_{rp,n}^{(j)} = \frac{-2}{j\pi} sin(j\pi(\bar{c}_r - 2\Omega_{rp,n} - 2\Omega_{sr}))sin(j\pi\phi_r) \tag{3.58}$$

$$q_{rp,n}^{(j)} = \frac{-2}{j\pi} cos(j\pi(\bar{c}_r - 2\Omega_{rp,n} - 2\Omega_{sr}))sin(j\pi\phi_r) \tag{3.59}$$

3.A.2 Matrix used in finite element model of curved beam

$$[B] = \begin{bmatrix} 1 & \cos\theta_1 & \sin\theta_1 & \theta_1\sin\theta_1 & 0 & \theta_1\cos\theta_1 \\ \bar{A}\theta_1 & \sin\theta_1 & -\cos\theta_1 & \sin\theta_1 - \theta_1\cos\theta_1 & 1 & \cos\theta_1 + \theta_1\sin\theta_1 \\ \bar{A}\theta_1 R_r^{-1} & 0 & 0 & 2R_r^{-1}\sin\theta_1 & R_r^{-1} & 2R_r^{-1}\cos\theta_1 \\ 1 & \cos\theta_2 & \sin\theta_2 & \theta_2\sin\theta_2 & 0 & \theta_2\cos\theta_2 \\ \bar{A}\theta_2 & \sin\theta_2 & -\cos\theta_2 & \sin\theta_2 - \theta_2\cos\theta_2 & 1 & \cos\theta_2 + \theta_2\sin\theta_2 \\ \bar{A}\theta_2 R_r^{-1} & 0 & 0 & 2R_r^{-1}\sin\theta_2 & R_r^{-1} & 2R_r^{-1}\cos\theta_2 \end{bmatrix} \tag{3.60}$$

$$[D] = \begin{bmatrix} 0 & 0 & 0 & -2\sin\theta_1 & 0 & -2\cos\theta_1 \\ 0 & 0 & 0 & 2\cos\theta_1 & 1 & -2\sin\theta_1 \\ -R_r & 0 & 0 & -2R_r\cos\theta_1 & R_r^{-1} & 2R_r\sin\theta_1 \\ 0 & 0 & 0 & 2\sin\theta_2 & 0 & -2\cos\theta_2 \\ 0 & 0 & 0 & -2\cos\theta_2 & 1 & -2\sin\theta_2 \\ R_r & 0 & 0 & 2R_r\cos\theta_2 & R_r^{-1} & -2R_r\sin\theta_2 \end{bmatrix} \tag{3.61}$$

$$[H] = \begin{bmatrix} 1 & \cos\theta & \sin\theta & \theta\sin\theta & 0 & \theta\cos\theta \\ \bar{A}\theta & \sin\theta & -\cos\theta & \sin\theta - \theta\cos\theta & 1 & \cos\theta + \theta\sin\theta \\ \bar{A}\theta R_r^{-1} & 0 & 0 & 2R_r^{-1}\sin\theta & R_r^{-1} & 2R_r^{-1}cos\theta \end{bmatrix} \tag{3.62}$$

$$\bar{A} = 1 + \left(\frac{I_l}{AR_r^2}\right) \tag{3.63}$$

$$[\Lambda] = diag\,(A\ A\ I) \tag{3.64}$$

$$\{u_\upsilon\ \ u_\tau\ \ u_\theta\}^T = [H]\,\{G_l\ \ G_2\ \ G_3\ \ G_4\ \ G_5\ \ G_6\}^T \tag{3.65}$$

$$\{u_{l,\upsilon}\ \ u_{l,\tau}\ \ u_{l,\theta}\ \ u_{l+1,\upsilon}\ \ u_{l+1,\tau}\ \ u_{l+1,\theta}\}^T = [B]\,\{G_l\ \ G_2\ \ G_3\ \ G_4\ \ G_5\ \ G_6\}^T \tag{3.66}$$

$$\left[\bar{N}\right] = [H]\,[B]^T \tag{3.67}$$

3.A.3 Matrices M, K and C

3.A.3.1 Mass matrices

$$[M] = \begin{bmatrix} [M_1] & 0 \\ 0 & a_2 T_v^2 \end{bmatrix} \tag{3.68}$$

$$[M_1] = diag\,(M_s \quad M_{p1} \quad \cdots \quad M_{pn} \quad M_c \quad M_l) \tag{3.69}$$

$$[M_j] = diag\left(m_j \quad m_j \quad \frac{I_j}{R_j^2}\right) \quad j = s, c, p_1, \ldots, p_N \tag{3.70}$$

3.A.3.2 Stiffness matrices

$$[K_e] = \begin{bmatrix} [K_{e1}] & [K_{e2}] \\ 0 & 1 \end{bmatrix} \tag{3.71}$$

$$[K_e1] = \begin{bmatrix} [K_i] & [K_j] \\ [K_j]^T & [K_l] + [K_{sc}] \end{bmatrix} \tag{3.72}$$

$$[K_{e2}] = \begin{bmatrix} 0 & 0 & 0 & \cdots & 0 & \rho_a A_b R_b \frac{C_p}{\lambda_0} V_0 \sigma_t k_v & 0 & \cdots & 0 & 0 \end{bmatrix}^T \tag{3.73}$$

$$[K_i] = \begin{bmatrix} K_{S1} & K_{S2} & \cdots & K_{S2} & \cdots & K_{S2} & 0 \\ & K_{P1} & \cdots & 0 & \cdots & 0 & K_{Q1} \\ & & \ddots & \vdots & \ddots & \vdots & \vdots \\ & & & K_{Pn} & \cdots & 0 & K_{Qn} \\ & & & & \ddots & \vdots & \vdots \\ & symmetric & & & & K_{PN} & K_{QN} \\ & & & & & & K_C \end{bmatrix} \tag{3.74}$$

$$[K_{S1}] = \sum_{n=1}^{3} k\,(t)_{e,sp} \begin{bmatrix} \sin^2 \psi_{sp,n} & -\sin \psi_{sp,n} \cos \psi_{sp,n} & -\sin \psi_{sp,n} \\ & \cos^2 \psi_{sp,n} & \cos \psi_{sp,n} \\ symmetric & & 1 \end{bmatrix} \tag{3.75}$$

$$[K_{S2}] = k\,(t)_{e,sp} \begin{bmatrix} \sin \alpha_s \sin \psi_{sp,n} & \cos \alpha_s \sin \psi_{sp,n} & -\sin \psi_{sp,n} \\ -\sin \alpha_s \cos \psi_{sp,n} & -\cos \alpha_s \cos \psi_{sp,n} & \cos \psi_{sp,n} \\ -\sin \alpha_s & -\cos \alpha_s & 1 \end{bmatrix} \tag{3.76}$$

$$[K_{Pn}] = k\,(t)_{e,sp} \begin{bmatrix} \sin^2 \alpha_s & \cos \alpha_s \sin \alpha_s & -\sin \alpha_s \\ \cos \alpha_s \sin \alpha_s & \cos^2 \alpha_s & -\cos \alpha_s \\ -\sin \alpha_s & -\cos \alpha_s & 1 \end{bmatrix} \tag{3.77}$$

$$+k\,(t)_{e,rp} \begin{bmatrix} \sin^2 \alpha_r & -\cos \alpha_r \sin \alpha_r & -\sin \alpha_r \\ -\cos \alpha_r \sin \alpha_r & \cos^2 \alpha_r & \cos \alpha_r \\ -\sin \alpha_r & \cos \alpha_r & 1 \end{bmatrix} \tag{3.78}$$

$$[K_{Qn}] = k_{p,n} \begin{bmatrix} -\cos \psi_n & -\sin \psi_n & 0 \\ \sin \psi_n & -\cos \psi_n & -1 \\ 0 & 0 & 0 \end{bmatrix} \tag{3.79}$$

$$[K_C] = \sum_{n=1}^{3} k_{p,n} \begin{bmatrix} \sin^2 \psi_{sp,n} + \cos^2 \psi_{sp,n} & 0 & -\sin \psi_n \\ 0 & \sin^2 \psi_{sp,n} + \cos^2 \psi_{sp,n} & \cos \psi_n \\ -\sin \psi_n & \cos \psi_n & 1 \end{bmatrix} \tag{3.80}$$

$$[K_j] = \begin{bmatrix} 0 & \cdots & 0 & \cdots & 0 & \cdots & 0 \\ K_R & \cdots & 0 & \cdots & 0 & \cdots & 0 \\ \vdots & \ddots & \vdots & \ddots & \vdots & \ddots & \vdots \\ 0 & \cdots & K_R & \cdots & 0 & \cdots & 0 \\ \vdots & \ddots & \vdots & \ddots & \vdots & \ddots & \vdots \\ 0 & \cdots & 0 & \cdots & K_R & \cdots & 0 \\ 0 & \cdots & 0 & \cdots & 0 & \cdots & 0 \end{bmatrix} \tag{3.81}$$

$$[K_R] = k(t)_{e,rp} \begin{bmatrix} -N_{11}(\theta)\sin\alpha_r & -N_{12}(\theta)\sin\alpha_r & \cdots & -N_{16}(\theta)\sin\alpha_r \\ N_{21}(\theta)\cos\alpha_r & N_{22}(\theta)\cos\alpha_r & \cdots & N_{26}(\theta)\cos\alpha_r \\ N_{31}(\theta) & N_{32}(\theta) & \cdots & N_{36}(\theta) \end{bmatrix} \tag{3.82}$$

$$[K_{sc}] = diag\,(k_{sc,r} \quad k_{sc,\tau} \quad k_{sc,\theta} \cdots 0 \cdots k_{sc,r} \quad k_{sc,\tau} \quad k_{sc,\theta} \cdots 0) \tag{3.83}$$

$$\{W(t)\} = \{0 \quad 0 \quad 0 \quad \cdots \quad W_w \quad 0 \quad \cdots \quad 0\} \tag{3.84}$$

$$\{F_d\} = \left\{0 \quad 0 \quad 0 \quad \cdots \quad \frac{T_d}{R_c} \quad 0 \quad \cdots \quad 0\right\} \tag{3.85}$$

$$\{F_e\} = \{F_{e,sp} + F_{e,rp} \quad F_r\} \tag{3.86}$$

$$\{F_{e,sp}\} = \{-\sum_{n=1}^{3} f_{0,sp}\ \sin(\psi_{sp,n}) \quad \sum_{n=1}^{3} f_{0,sp}\, cos(\psi_{sp,n}) \quad \sum_{n=1}^{3} f_{0,sp}$$
$$- f_{0,sp}\, sin(\psi_{sp,1}) \quad - f_{0,sp}\, cos(\psi_{sp,1}) \quad f_{0,sp}$$
$$- f_{0,sp}\, sin(\psi_{sp,2}) \quad - f_{0,sp}\, cos(\psi_{sp,2}) \quad f_{0,sp}$$
$$- f_{0,sp}\, sin(\psi_{sp,3}) \quad - f_{0,sp}\, cos(\psi_{sp,3}) \quad f_{0,sp} \quad 0 \quad 0 \quad 0\}^T \quad (3.87)$$

$$\{F_{e,rp}\} = \{0 \quad 0 \quad 0 \quad f_{0,rp}\ \sin(\alpha_r) \quad - f_{0,rp}\, cos(\alpha_r) \quad - f_{0,rp}$$
$$f_{0,rp}\ \sin(\alpha_r) \quad - f_{0,rp}\, cos(\alpha_r) \quad - f_{0,rp}$$
$$f_{0,rp}\, sin(\alpha_r) \quad - f_{0,rp}\, cos(\alpha_r) \quad - f_{0,rp} \quad 0 \quad 0 \quad 0\}^T \quad (3.88)$$

$$\{F_r\} = \{f_{0,rp}\left(N_{11}\left(\theta_1\right)\cos\left(\alpha_r\right) + N_{21}\left(\theta_1\right)\sin\left(\alpha_r\right)\right)$$
$$f_{0,rp}\left(N_{16}\left(\theta_1\right)\cos\left(\alpha_r\right) + N_{26}\left(\theta_1\right)\sin\left(\alpha_r\right)\right) \quad 0 \quad \cdots$$
$$0 \quad \cdots \quad f_{0,rp}\left(N_{11}\left(\theta_2\right)\cos\left(\alpha_r\right) + N_{21}\left(\theta_2\right)\sin\left(\alpha_r\right)\right)$$
$$f_{0,rp}\left(N_{16}\left(\theta_2\right)\cos\left(\alpha_r\right) + N_{26}\left(\theta_2\right)\sin\left(\alpha_r\right)\right) \quad 0 \quad \cdots$$
$$0 \quad \cdots \quad f_{0,rp}\left(N_{11}\left(\theta_3\right)\cos\left(\alpha_r\right) + N_{21}\left(\theta_3\right)\sin\left(\alpha_r\right)\right)$$
$$f_{0,rp}\left(N_{16}\left(\theta_3\right)\cos\left(\alpha_r\right) + N_{26}\left(\theta_3\right)\sin\left(\alpha_r\right)\right) \quad 0 \quad \cdots \quad 0\}^T \quad (3.89)$$

3.A.3.3 Damping matrices

$$[C] = \begin{bmatrix} [C_1] & [C_2] \\ 0 & a_2 T_v + T_v \end{bmatrix} \quad (3.90)$$

$$[C_1] = 0.05\,[M_1] + 0.03\,[K_{e1}] \quad (3.91)$$

$$[C_2] = \begin{bmatrix} 0 & 0 & 0 & \cdots & 0 & \rho_a A_b R_b \frac{C_p}{\lambda_0} V_0 \sigma_t k_v T_v a_1 & 0 & \cdots & 0 & 0 \end{bmatrix}^T \tag{3.92}$$

References

[1] Kahraman A. Load sharing characteristics of planetary transmissions. Mechanism and Machine Theory. 1994 Nov 1;29(8):1151-65.

[2] Kim W, Lee JY, Chung J. Dynamic analysis for a planetary gear with time-varying pressure angles and contact ratios. Journal of Sound and Vibration. 2012 Feb 13;331(4):883-901.

[3] Bahk CJ, Parker RG. Analytical solution for the nonlinear dynamics of planetary gears. Journal of Computational and Nonlinear Dynamics. 2011 Apr 1;6(2).

[4] Li S, Wu Q, Zhang Z. Bifurcation and chaos analysis of multistage planetary gear train. Nonlinear Dynamics. 2014 Jan 1;75(1-2):217-33.

[5] Sun T, Hu H. Nonlinear dynamics of a planetary gear system with multiple clearances. Mechanism and Machine Theory. 2003 Dec 1;38(12):1371-90.

[6] Ambarisha VK, Parker RG. Nonlinear dynamics of planetary gears using analytical and finite element models. Journal of sound and vibration. 2007 May 8;302(3):577-95.

[7] Guo Y, Parker RG. Dynamic modeling and analysis of a spur planetary gear

involving tooth wedging and bearing clearance nonlinearity. European Journal of Mechanics-A/Solids. 2010 Nov 1;29(6):1022-33.

[8] Guo Y, Parker RG. Dynamic analysis of planetary gears with bearing clearance. Journal of computational and nonlinear dynamics. 2012 Oct 1;7(4).

[9] Kahraman A, Kharazi AA, Umrani M. A deformable body dynamic analysis of planetary gears with thin rims. Journal of sound and vibration. 2003 May 1;262(3):752-68.

[10] Kahraman A, Vijayakar S. Effect of internal gear flexibility on the quasi-static behavior of a planetary gear set. J. Mech. Des.. 2001 Sep 1;123(3):408-15.

[11] Abousleiman V, Velex P. A hybrid 3D finite element/lumped parameter model for quasi-static and dynamic analyses of planetary/epicyclic gear sets. Mechanism and Machine Theory. 2006 Jun 1;41(6):725-48.

[12] Abousleiman V, Velex P, Becquerelle S. Modeling of spur and helical gear planetary drives with flexible ring gears and planet carriers. ASME: Journal of Mechanical Design. 2007 Jan;129(1):95–106

[13] Hu Y, Talbot D, Kahraman A. A Gear Load Distribution Model for a Planetary Gear Set With a Flexible Ring Gear Having External Splines. Journal of Mechanical Design. 2019 May 1;141(5).

[14] Xun C, Long X, Hua H. Effects of random tooth profile errors on the dynamic be-

haviors of planetary gears. Journal of Sound and Vibration. 2018 Feb 17;415:91-110.

[15] Alemayehu FM, Ekwaro-Osire S. Probabilistic Multibody Modeling of Gearboxes for wind turbines. InASME 2011 International Mechanical Engineering Congress and Exposition 2011 Jan 1 (pp. 793-804). American Society of Mechanical Engineers Digital Collection.

[16] Wang L, Shen T, Chen C, Chen H. Dynamic reliability analysis of gear transmission system of wind turbine in consideration of randomness of loadings and parameters. Mathematical Problems in Engineering. 2014;2014.

[17] Srikanth P, Sekhar AS. Dynamic analysis of wind turbine drive train subjected to nonstationary wind load excitation. Proceedings of the Institution of Mechanical Engineers, Part C: Journal of Mechanical Engineering Science. 2015 Feb;229(3):429-46.

[18] Wei S, Han Q, Peng Z, Chu F. Dynamic analysis of wind turbine gearboxes with unknown-but-bounded parameters under random wind excitation. IET Renewable Power Generation. 2016 Jun 29;11(4):433-42.

[19] Yang J, Yang P. Random vibration analysis of planetary gear trains. Journal of Vibration and Acoustics. 2013 Apr 1;135(2).

[20] Yang J, Yang P. Random vibration and dynamic analysis of a planetary gear train in a wind turbine. Shock and Vibration. 2016.

[21] Beyaoui M, Tounsi M, Abboudi K, Feki N, Walha L, Haddar M. Dynamic behaviour of a wind turbine gear system with uncertainties. Comptes Rendus Mecanique. 2016 Jun 1;344(6):375-87.

[22] Chen H, Wang X, Gao H, Yan F. Dynamic characteristics of wind turbine gear transmission system with random wind and the effect of random backlash on system stability. Proceedings of the Institution of Mechanical Engineers, Part C: Journal of Mechanical Engineering Science. 2017 Jul;231(14):2590-7.

[23] Lin J. Parker RG.Planetary gear parametric instability caused by mesh stiffness variation. Journal of Sound and vibration. 2002;249(1):129-145.

[24] Wu JS, Chiang LK. Dynamic analysis of an arch due to a moving load. Journal of Sound and Vibration. 2004 Jan 22;269(3-5):511-34.

[25] Bianchi FD, De Battista H, Mantz RJ. Wind turbine control systems: principles, modelling and gain scheduling design. Springer Science & Business Media; 2006 Sep 7.

[26] Roberts JB, Spanos PD. Random vibration and statistical linearization. Courier Corporation; 2003 Dec 9.3.

[27] Yang J. Vibration analysis on multi-mesh gear-trains under combined deterministic and random excitations. Mechanism and Machine Theory. 2013 Jan 1;59:20-33.

[28] Bernard P, Fleury G. Stochastic newmark scheme. Probabilistic engineering mechanics. 2002 Jan 1;17(1):45-61.

[29] Bucher C. Computational analysis of randomness in structural mechanics: Structures and infrastructures book series, vol. 3. Crc Press (2009)

[30] Guo Y, Keller J, Parker, R G. Nonlinear dynamics and stability of wind turbine planetary gear sets under gravity effects. European Journal of Mechanics-A/Solids. 2014;47:45-57

[31] TOBE T, SATO K. Statistical analysis of dynamic loads on spur gear teeth. Bulletin of JSME. 1977;20(145):882-9.

Chapter 4

Random Vibration of A Nonlinear Gear Pair Using Energy-Based Statistical Linearization

Jalal Taheri Kahnamouei, Ph.D. Candidate

Jianming Yang, Associate Professor

Faculty of Engineering and Applied Science, Memorial University ofNewfoundland,

St. John's, NL, Canada AlB 3X5

This chapter was submitted as a full research paper to the Journal of Nonlinear Dynamics, Springer on August 24th, 2020 and is currently under review.

In this chapter, the energy-based statistical linearization technique was developed for nonlinear stochastic dynamic gear systems. There are four criteria of statistical linearization, in which two of them are forced-based, and two others are energy-based. This chapter focused on energy-based statistical linearization, and the idea of this criterion is according to minimizing mean-square error in potential energies between the original and equivalent linear systems. Force-based statistical linearization was

used by Yang for fixed gear-pair, and, in Chapter 3, I used force-based statistical linearization for planetary gear transmission with moving gear-pair. To the best of my knowledge, there is not any published research that developed energy-based statistical linearization for geared systems.

Abstract

In this article, an energy-based statistical linearization method (SL) is proposed to simulate a nonlinear dynamic model of spur gear pair. The gear pair operates under combined deterministic and random loads, and both backlash and time-varying mesh stiffness are considered in the dynamic model. The equivalent linear function approximates the teeth backlash nonlinearity in the gear model. The energy-based linearization, which minimizes the error in potential energy between the original and equivalent linear systems, is used. Simulations are conducted on a gear-pair, and the effect of the input torque on the dynamic response of the gear pair is then examined. The results demonstrate that for high input torque, the system operates in the linear range. For low input torque, the results are not similar to the original because the system became strongly nonlinear. Monte Carlo simulations were carried out to verify the accuracy of the presented method.

4.1 Introduction

Geared systems are widely used in mechanisms found in the automation and aviation industries. The advancement of these industries demands high-performance mechanisms, and it is necessary to enhance the performance of the gears in order to meet the needs of these industries. Thus, an in-depth analysis of the various aspects of a geared system is necessary. The dynamic behavior of gears has been widely investigated by researchers to clarify the fundamental problems of a gear pair [1-3] . These problems become more critical in complicated mechanisms such as backlash, clearance, and tooth crack [4, 5]. The literature shows that the operation of a geared system is affected by many factors, which include backlash, time-varying mesh stiffness, and randomness [3, 6, 7]. Therefore, this paper will provide a detailed assessment of the three aforementioned phenomena in order to help describe many of the dynamic specifications of a geared system.

While considerable research has been conducted on the deterministic part of these systems, only limited research has been conducted on the stochastic part of these systems. Different methods have been introduced to solve the stochastic equations, but only some of them apply to the stochastic gear dynamic systems. The first method of SL was introduced to engineering fields by Booton [8] to study nonlinear control system under random signals. Brückner and Lin [9] developed an SL method for systems with both parametric and external white noise excitations. They found the

first and second moments by minimizing the mean square deviation of the difference between the linear and nonlinear equations. Elishakoff *et al.* [10] proposed a new SL method based on the potential energy of the system. They determined the equivalent linear equations by minimizing the mean square of the difference of potential energies of the original and equivalent models. Sobiechowski, and Socha [11] applied four different SL criteria to Duffing oscillator and then compared the results to each other. Although several studies have been published in the statistical linearization of geared systems, those studies only used a force-based criterion; no research has yet investigated the stochastic linearization of geared systems using energy-based criteria. Tobe, and Sato [12], first used a statistical linearization method in order to analyze the nonlinear stochastic spur gear dynamics. Tobe *et al.* [13] then conducted a second study using an experimental method to compare results to their previous study, and the results verified the SL results of [12]. Based on the SL method introduced by Tobe, Yang [14] developed a statistical linearization method and used a stochastic Newmark scheme to investigate the dynamic responses of the geared system under both deterministic and random excitation. The linear equations were established by minimizing the mean square deviation of the difference between the linear and nonlinear parts. His findings suggested that, gears work as a linear system in heavy-loaded operating conditions. Kahnamouei and Yang [15] developed a stochastic nonlinear dynamic model of a planetary gearbox with an elastic ring gear and used the SL method to linearize the nonlinear-moving mesh loads. The nonlinear backlash func-

tions were more complicated in their model because backlash functions were affected by the transverse and torsional movement of gears and carrier, and elastic behavior for the ring gear.

Other stochastic nonlinear gear analysis methods include aspects that factor into the proposed method of this study. Neriya *et al.* [16], who used the matrix exponential method to study the oscillation of helical geared systems using both deterministic and random excitation. They considered the backlash and time-variant mesh stiffness in a dynamic model, and concluded that the combination of the matrix exponential and piecewise linearization methods was stable and accurate. Naess *et al.* [17] used the path integration method to study stochastic gear mechanics, and modeled the gear pair with the backlash under Gaussian white noise. Hasnijeh *et al.* [18] used an adaptive time-stepping path integration method to investigate the nonlinear random dynamics of a spur gear. They then used the Monte Carlo simulations to validate the accuracy of their method. These methods did not attempt to simplify equation solution through linearization.

In this paper, the energy-based statistical linearization is applied to the gear model, which includes gear backlash, mesh stiffness variation, and random excitation. The linear equation obtained by the method is then solved using the stochastic Newmark method. To analyze the efficiency of the method under various load conditions, different values of torque are chosen and then applied to the equation to generate simulated results. In addition, the Monte Carlo simulations (MCS) are carried out

to assess the reliability of the method.

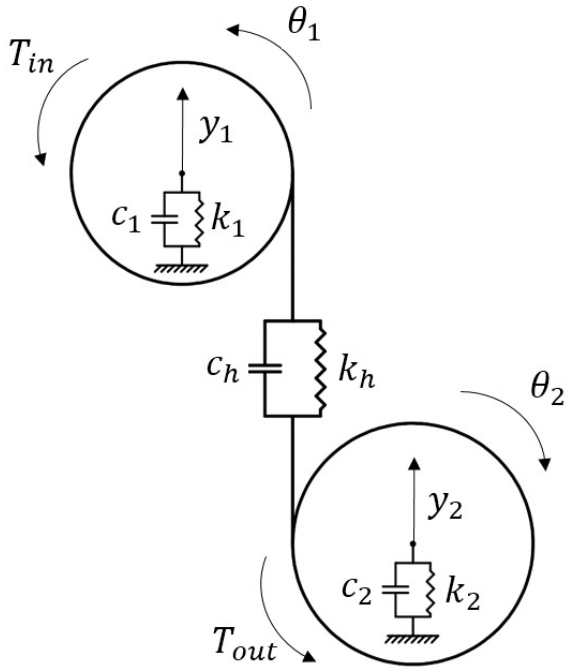

Figure 4.1: Four-DOF transverse-torsional model of gear pair

4.2 Dynamic Model

In this paper, a single pair of spur gears is considered (Figure 4.1). To develop the dynamic gear model, a transverse-torsional model is used with four degrees of freedom. This model includes gears with the known parameters of mass, m_i, mass moments of inertia, I_i, number of teeth, a_i, and pitch radius, r_i (i=1,2). Also, bearings are used to support gears with lumped stiffness, k_{y_1} and k_{y_2}, at directions y_1 and y_2, respectively. Each gear has two degrees of freedom, one translation in the y_i direction, which is

parallel to the line of action of the gears, and one rotational in the θ_i direction. The equation of the gear pair shown in Figure 4.1 is given by:

$$m_1\ddot{y}_1 + k_1 y_1 + f\left(y_1 - y_2 + \theta_1 r_1 - \theta_2 r_2\right) = 0 \tag{4.1}$$

$$I_1\ddot{\theta}_1 + f\left(y_1 - y_2 + \theta_1 r_1 - \theta_2 r_2\right) r_1 = T_{in} \tag{4.2}$$

$$m_2\ddot{y}_2 + k_2 y_2 - f\left(y_1 - y_2 + \theta_1 r_1 - \theta_2 r_2\right) = 0 \tag{4.3}$$

$$I_2\ddot{\theta}_2 - f\left(y_1 - y_2 + \theta_1 r_1 - \theta_2 r_2\right) r_2 = -T_{out} \tag{4.4}$$

where T_{in} and T_{out} refer to the input and output torques applied to the first and second gears, respectively, and f is the mesh force between the gear pair. In order to transform the system with four aforementioned equations into a third order equation, the torsional motion equations are rewritten in terms of the relative translational displacement, $z = \theta_1 r_1 - \theta_2 r_2$. The governing equations of motions of the gears are given as:

$$m_1\ddot{y}_1 + k_1 y_1 + f\left(y_1 - y_2 + z\right) = 0 \tag{4.5}$$

$$m_2\ddot{y}_2 + k_2 y_2 - f\left(y_1 - y_2 + z\right) = 0 \tag{4.6}$$

$$m_c\ddot{z} + f\left(y_1 - y_2 + z\right) = \frac{T_{in}}{r_1} \tag{4.7}$$

where

$$m_c = \frac{I_1 I_2}{I_2 r_1^2 + I_1 r_2^2} \tag{4.8}$$

In equations 4.5 to 4.7, f represents the nonlinear function caused by the backlash, $2b$, at meshing point and is given as:

$$f(\delta) = \begin{cases} k_h(t)(\delta - b), & \delta \geq b \\ 0, & -b \leq \delta \leq b \\ k_h(t)(\delta + b), & \delta \leq -b \end{cases} \tag{4.9}$$

where $k_h(t)$ is the mesh stiffness, and δ represents the relative displacement at the gear meshing point and is given as:

$$\delta = y_1 - y_2 + z \tag{4.10}$$

Due to the $k(t)$ is assumed as time-variant stiffness, it is expanded into the Fourier Series [19].

$$k_h(t) \approx k_0 + \sum_{j=1}^{n} \left[k_a^{(j)} \sin \omega j \ t + k_b^{(j)} \cos \omega j \ t \right] \tag{4.11}$$

where k_0 is the average of the stiffness, $k_a^{(j)}$ and $k_b^{(j)}$ are the harmonic coefficients of the Fourier series, n is the number of the harmonic terms retained, and ω is the meshing frequency. In addition to the deterministic excitation, the gear pair works under random excitation, and random excitation is considered in the model by embedding it into the second side of Eq. 4.7. Therefore, the governing equation of the gear system considering the stochastic excitation takes the following form:

$$M\ddot{q} + C\dot{q} + K_s q + F_{int}(q) = F_{ex} + BW(t) \tag{4.12}$$

$$M = diag(m \quad m \quad m_c) \tag{4.13}$$

$$q = \{y_1 \quad y_2 \quad z\}^T \tag{4.14}$$

$$K_s = diag(k_1 \quad k_2 \quad 0) \tag{4.15}$$

$$F_{int} = \{f(\delta) \quad f(\delta) \quad f(\delta)\} \tag{4.16}$$

$$F_{ex} = \left\{0 \quad 0 \quad \frac{T_{in}}{r_1}\right\} \tag{4.17}$$

$$B = diag(0 \quad 0 \quad \bar{w}_0) \tag{4.18}$$

where M is a mass matrix, C is a damping matrix, K_s is a bearings' stiffness matrix, q the displacement vector, F_{int} is the internal nonlinear meshing force vector, F_{ex} represents the external force vector, and $\bar{w}_0$ and B are the amplitude and amplitude matrix of random excitation, respectively. $W(t)$ is the Gaussian white noise vector with mean and correlation function as follows:

$$E[W(t)] = 0 \tag{4.19}$$

$$E[W(t)]E[W(t+\tau)] = 2\pi S_0 D(\tau) \tag{4.20}$$

where $2\pi S_0$ is the intensity of white noise, $D(\tau)$ is the Dirac delta function, and $E[\cdot]$ indicates the expectation operation for continuous random variables which is defined as:

$$E[\cdot] = \int_{-\infty}^{\infty} [\cdot]\, g(X) dX \tag{4.21}$$

$$g(X) = \frac{1}{\sigma\sqrt{2\pi}} e^{\frac{-(X-X_0)^2}{2\sigma^2}} \tag{4.22}$$

In this paper, proportional damping is assumed, therefore, the damping matrix is given as $C = \Lambda_a M + \Lambda_b K$ where Λ_a and Λ_b are constant numbers. Because the system operates under excitation of non-zero mean external forces, the response of Eq. 4.12 will be a non-zero mean represented by the following equation:

$$q = q_0 + \hat{q} \tag{4.23}$$

where q_0 is the mean value of displacement vector, and $\hat{q}$ is the zero-mean displacement vector. Substituting Eq. 4.23 into Eq. 4.12 is given in equation 4.24 below.

$$M\ddot{q_0} + C\dot{q_0} + K_s q_0 + M\ddot{\hat{q}} + C\dot{\hat{q}} + K_s\hat{q} + F(q_0 + \hat{q}) = F_{ex} + BW(t) \tag{4.24}$$

4.3 Statistical Linearization Formulation

Statistical linearization is one of the most useful methods to solve the nonlinear equations under both deterministic and stochastic excitation. The nonlinear meshing force function, $f(\delta)$, is replaced by the linear function, $f_e(\delta)$, as follows:

$$f_e(\delta) = k_e\hat{\delta} + f_0 \tag{4.25}$$

where k_e is the equivalent stiffness and f_0 denotes the produced deterministic force. By replacing the nonlinear part of Eq. 4.24 with linear function, the governing equiv-

alent linear equation expresses in the following form:

$$M\ddot{q_0} + C\dot{q_0} + K_s q_0 + M\ddot{\hat{q}} + C\dot{\hat{q}} + K_s\hat{q} + K_e\hat{q} + F_0 = F_{ex} + BW(t) \quad (4.26)$$

where matrix K_e and vector F_0 are denoted by the following forms:

$$[K_e] = \begin{bmatrix} k_e & -k_e & k_e \\ -k_e & k_e & -k_e \\ k_e & -k_e & k_e \end{bmatrix} \quad (4.27)$$

$$\{F_0\} = \begin{Bmatrix} f_0 & -f_0 & f_0 \end{Bmatrix}^T \quad (4.28)$$

Taking ensemble average of Eq. 4.26 yields:

$$M\ddot{q_0} + C\dot{q_0} + K_s q_0 + f_0 = F_{ex} \quad (4.29)$$

Subtracting Eq.4.26 from Eq.4.29 gives:

$$M\ddot{\hat{q}} + C\dot{\hat{q}} + (K_s + K_e)\hat{q} = BW(t) \quad (4.30)$$

Equations 4.29 and 4.30 give the mean and standard deviation of the responses, respectively. There are different criteria of linearization to determine the coefficients of an equivalent linear equation, k_e and f_0. In this paper, a energy-based SL is used.

4.3.1 Energy-based criteria

In this criterion, linearization is conducted based on the potential energy of the system. In order to determine the equivalent linear coefficients, this method requires that the mean square of the difference of the potential energies of the original and equivalent model becomes a minimum [20]. From Eq. 4.25, the difference in potential energy of the original and equivalent model is expressed as:

$$\varepsilon_p = P(\delta) - \int (k_e\hat{\delta} + f_0)d\hat{\delta} = P(\delta) - \frac{1}{2}k_e\,\hat{\delta}^2 - f_0\hat{\delta} \tag{4.31}$$

where $P(\delta)$ is the potential energy of the nonlinear part and from Eq. 4.9 it is defined as:

$$P(\delta) = \begin{cases} \frac{1}{2}k_h(t)\delta^2 - k_h(t)b\delta, & \delta \geq b \\ 0, & -b \leq \delta \leq b \\ \frac{1}{2}k_h(t)\delta^2 + k_h(t)b\delta, & \delta \leq -b \end{cases} \tag{4.32}$$

According to the criteria, the minimization of the mean square of ε_p is given as:

$$E\left[\varepsilon_p^2\right] = minimum \tag{4.33}$$

where $E[\,]$ is expectation operation which is denied in Eq. 4.21. By considering this criteria, Eq. 4.33 can be expressed as:

$$E\left[\varepsilon_p^2\right] = E\left[\left(P(\delta) - \frac{1}{2}k_e\,\hat{\delta}^2 - f_0\hat{\delta}\right)^2\right] \tag{4.34}$$

Therefore, to minimize the difference derivative that comes from Eq. 4.34, with respect to k_e and f_0, the equations are expressed as:

$$\frac{\partial E\left[\varepsilon_p^2\right]}{\partial k_e} = 0 \tag{4.35}$$

$$\frac{\partial E\left[\varepsilon_p^2\right]}{\partial f_0} = 0 \tag{4.36}$$

By inserting the Eq. 4.34 into the Eq. 4.35, we have:

$$\frac{\partial}{\partial k_e} E\left[P(\delta)^2 + \frac{1}{4}{k_e}^2\hat{\delta}^4 + {f_0}^2\hat{\delta}^2 - P(\delta)k_e\,\hat{\delta}^2 - 2P(\delta)f_0\hat{\delta} + k_e f_0\hat{\delta}^3\right] = 0 \tag{4.37}$$

Taking the derivative respect to k_e and applying $E(\hat{\delta}^3) = 0$ because of $\hat{\delta}$ is zero mean variable, the Eq. 4.37 expressed in the following form:

$$E\left[\frac{1}{2}k_e\hat{\delta}^4 - P(\delta)\hat{\delta}^2\right] = 0 \tag{4.38}$$

After applying expectation operation and moving all parts except k_e to the other side of the equation, we have:

$$k_e = \frac{2E\left[P(\delta)\hat{\delta}^2\right]}{E\left[\hat{\delta}^4\right]} \tag{4.39}$$

By assuming the δ has the Gaussian distribution, the numerator of Eq. 4.39 can be represented in the form of Eq. 4.40 obtained through the process in which the integration by parts was applied on the expectation of the second-order derivative of

$P(\delta)$. Appendix 4.A.2 explains in detail the mathematics process that leads to Eq. 4.40.

$$E\left[P(\delta)\hat{\delta}^2\right] = \sigma^4 E\left[\nabla^2 P(\delta)\right] + \sigma^2 E\left[P(\delta)\right] \tag{4.40}$$

and because $\hat{\delta}$ is zero mean variables, its fourth-order expectation is equal to:

$$E\left[\hat{\delta}^4\right] = 3\sigma^4 \tag{4.41}$$

Thus, by inserting the Eq.s 4.40 and 4.41 into the Eq. 4.39, k_e is expressed in the following form:

$$k_e = \frac{2}{3} E\left[\frac{\partial^2 P(\delta)}{\partial \delta^2}\right] + \frac{2}{3}\frac{E\left[P(\delta)\right]}{\sigma^2} \tag{4.42}$$

Finally the equivalent mesh stiffness is repressed in the following form:

$$k_e = \frac{2}{3}\left[E\frac{\partial f(\delta)}{\partial \delta} + \frac{E\left(P(\delta)\right)}{\sigma^2}\right] \tag{4.43}$$

Also, by inserting Eq. 4.34 into Eq. 4.36, we have:

$$\frac{\partial}{\partial f_0} E\left[P(\delta)^2 + \frac{1}{4}{k_e}^2\,\hat{\delta}^4 + {f_0}^2\hat{\delta}^2 - P(\delta)k_e\,\hat{\delta}^2 - 2P(\delta)f_0\hat{\delta} + k_e f_0\hat{\delta}^3\right] = 0 \tag{4.44}$$

Taking the derivative respect to f_0 and applying $E(\hat{\delta}^3) = 0$ leads to:

$$E\left[2f_0\hat{\delta}^2 - 2P(\delta)\hat{\delta}\right] = 0 \tag{4.45}$$

getting expectation and moving all parts except f_0 to other side gives:

$$f_0 = \frac{E\left[P(\delta)\hat{\delta}\right]}{E\left[\hat{\delta}^2\right]} \tag{4.46}$$

The numerator of Eq. 4.46 can be rewritten in the following form obtained through the process, which applied the integration by parts on the expectation of the first-order derivative of $P(\delta)$, and Appendix 4.A.1 describes all detail about this mathematical process (Appendix 4.A.1 Eq. 4.74).

$$E\left[P(\delta)\hat{\delta}\right] = \sigma^2 E\left[\frac{\partial P(\delta)}{\partial \delta}\right] \tag{4.47}$$

Inserting Eq. 4.47 into Eq. 4.46 leads:

$$f_0 = \frac{\sigma^2 E\left[\nabla P(\delta)\right]}{E\left[\hat{\delta}^2\right]} \tag{4.48}$$

then after applying $E\left[\hat{\delta}^2\right] = \sigma^2$, the f_0 can be expressed into the following forms:

$$f_0 = E\left[f(\delta)\right] \tag{4.49}$$

Finally, f_0 are represented as the following form, and all detailed calculations are described in Appendix B:

$$f_0 = k_h\left[\frac{\delta_0}{2}(2+erf(V_1)-erf(V_2)) - \frac{\sigma}{\sqrt{2\pi}}\left(e^{-V_1^2}-e^{-V_2{}^2}\right)+\frac{b}{2}(erf(V_1)+erf(V_2))\right] \tag{4.50}$$

where

$$V_i = \frac{(-1)^i b - \delta_0}{\sqrt{2}\sigma} \qquad i = 1, 2$$

4.4 Solution Method

In this paper, the stochastic Newmark family method [21, 22] is used to solve the stochastic dynamic model of a geared system. After applying the linearization technique, the linear equations Eq.s 4.29 and 4.30 are gathered and represented in the following form:

$$M\ddot{q} + C\dot{q} + (K_s + K_e)\, q = F_{ex} + F_0 + BW(t) \tag{4.51}$$

For stochastic Newmark, the following equations are obtained by recasting Eq. 4.51 into state-space form with $\{q(t) \quad \dot{q}(t)\}^T$, and discretizing the time into a series of small time intervals Δt [21].

$$\begin{bmatrix} C+\frac{\Delta t}{2}(K_s+K_e) & M \\ M & -M\frac{\Delta t}{2} \end{bmatrix} \begin{Bmatrix} q_0\,(t_{i+1}) \\ \dot{q_0}\,(t_{i+1}) \end{Bmatrix} = \begin{bmatrix} C-\frac{\Delta t}{2}(K_s+K_e) & M \\ M & M\frac{\Delta t}{2} \end{bmatrix} \begin{Bmatrix} q_0\,(t_i) \\ \dot{q_0}\,(t_i) \end{Bmatrix} + \begin{bmatrix} \frac{\Delta t}{2} & \frac{\Delta t}{2} \\ 0 & 0 \end{bmatrix} \begin{Bmatrix} F_{ex}\,(t_i) - F_0\,(t_i) \\ F_{ex}\,(t_{i+1}) - F_0\,(t_{i+1}) \end{Bmatrix} + \begin{bmatrix} \sqrt{\Delta t}B & 0 \\ 0 & B\frac{\Delta t\sqrt{\Delta t}}{\sqrt{12}} \end{bmatrix} \begin{Bmatrix} \Psi\,(t_i) \\ \Phi\,(t_{i+1}) \end{Bmatrix} \tag{4.52}$$

where $\Psi\,(t_i)$ *and* $\Phi\,(t_i)$ are independent and identically distributed outcomes of standard Gaussian random variables. For convenience, the vectors and the matrices of Eq. 4.52 can be shown as:

$$\{Y(t_{i+1})\} = [N_2]\{Y(t_i)\} + [N_3]\{F(t_i)\} + [N_4]\{W(t_i)\} \tag{4.53}$$

$$\{Y(t_i)\} = \begin{Bmatrix} q(t_i) \\ \\ \dot{q}(t_i) \end{Bmatrix} \tag{4.54}$$

$$[N_1] = \begin{bmatrix} C + \frac{\Delta t}{2}(K_s + K_e) & M \\ \\ M & -M\frac{\Delta t}{2} \end{bmatrix} \tag{4.55}$$

$$[N_2] = [N_1]^{-1} \begin{bmatrix} C - \frac{\Delta t}{2}(K_s + K_e) & M \\ \\ M & M\frac{\Delta t}{2} \end{bmatrix} \tag{4.56}$$

$$[N_3] = [N_1]^{-1} \begin{bmatrix} \frac{\Delta t}{2} & \frac{\Delta t}{2} \\ \\ 0 & 0 \end{bmatrix} \tag{4.57}$$

$$[N_4] = [N_1]^{-1} \begin{bmatrix} \sqrt{\Delta t}B & 0 \\ \\ 0 & B\frac{\Delta t\sqrt{\Delta t}}{\sqrt{12}} \end{bmatrix} \tag{4.58}$$

$$\{F(t_i)\} = \begin{Bmatrix} F_{ex}(t_i) - F_0(t_i) \\ \\ F_{ex}(t_{i+1}) - F_0(t_{i+1}) \end{Bmatrix} \tag{4.59}$$

$$\{V(t_i)\} = \begin{Bmatrix} \Psi(t_i) \\ \\ \Phi(t_{i+1}) \end{Bmatrix} \tag{4.60}$$

The mean response is obtained by taking the ensemble average of Eq. 4.53 and is given as:

$$\langle\{Y(t_{i+1})\}\rangle = [N_2]\langle\{Y(t_i)\}\rangle + [N_3]\langle\{F(t_i)\}\rangle \tag{4.61}$$

where $\langle\rangle$ represent the ensemble average operation. Multiplying Eq. 4.53 with its transpose, and taking the average provides the correlation matrix [22]:

$$[R(t_{i+1})] = [N_2][R(t_i)][N_2]^T + [N_3][D_1][N_3]^T + [N_4][D_2][N_4]^T + [N_2][D_3][N_3]^T + [N_3][D_3]^T[N_2]^T \tag{4.62}$$

where

$$[R(t_i)] = \left\langle \left[Y(t_i)\, Y(t_i)^T \right] \right\rangle$$

$$[D_1] = \left\langle \left[F(t_i)\, F(t_i)^T \right] \right\rangle$$

$$[D_2] = \left\langle \left[V(t_i)\, V(t_i)^T \right] \right\rangle$$

$$[D_3] = \left\langle \left[Y(t_i)\, F(t_i)^T \right] \right\rangle$$

The entries in D_2 are either zero or unity. The relation between the mean responses obtained from Eq. 4.61 and the diagonal elements of $R(t)$ obtained from Eq. 4.62, provide the standard deviation of responses as below:

$$\sigma_j(t) = \sqrt{R_{j,j}(t) - \langle Y_j(t) \rangle^2} \qquad j = x, y, z \tag{4.63}$$

4.5 Monte Carlo simulations

In this study, Monte Carlo simulations [23] were carried out to verify the accuracy of the obtained results by using the energy-based statistical linearization method for the spur gear pair. To perform the MCS, the discretized independent random variables

with identical distribution represent the Gaussian white noise excitation. MATLAB software was used to generate a series of random variables, Υ, with zero mean and variance $\sigma_{\Upsilon}^2 = 2\pi S_0/\Delta t$, and the variable is defined as:

$$\Upsilon = \sqrt{\frac{2\pi}{\Delta t}}\upsilon \tag{4.64}$$

where υ represents an random number with independent and identical distribution. At each time step, one of these random variables was embedded into the nonlinear dynamic equation, Eq.4.12, and then the response $q(t)$ was computed using the deterministic solution scheme. After conducting numerous set simulations that could determine the MCS results' accuracy, the response statistics were computed as follow:

$$\hat{E}[\eta] = \frac{1}{N}\sum_{i=1}^{N}\eta_i \qquad \eta = x, y, z \tag{4.65}$$

$$\hat{\sigma}_\eta = \sqrt{\frac{1}{N-1}\sum_{i=1}^{N}\left(\eta_i - \hat{E}[\eta]\right)^2} \qquad \eta = x, y, z \tag{4.66}$$

where $\hat{E}[\,]$ is expectation operator for discrete random variables, $\hat{\sigma}$ is the variance of discrete random variables, and N is the number of Monte Carlo simulations.

4.6 Simulation Results and Analysis

4.6.1 Parameters

A simulation was carried out with a single gear pair (Figure 4.1), the properties of which are given in Table 4.1. The backlash parameter was considered $b = 20\mu$m. Further, the amplitude of white noise, $\bar{w}_0$, in Eq. 4.51 was set as 100. Depending on the level of input torque, three cases were observed: (a) without impact, (b) single-sided impact, and (c) double-sided impact. The results of the linearization method for all cases are provided. To determine the accuracy of this method, the results were then compared with results obtained from the Monte Carlo simulations. In this study, 20,000 set of simulations with time step $\Delta t = 0.01$ s and $S_0 = 1$ were carried out.

Table 4.1: Gears' Parameters

Parameter	Value	Parameter	Value
a_1	21	I_1 $(kg.m^2)$	3.2
a_2	39	I_2 $(kg.m^2)$	3.2
r_1 (mm)	215.6	k_1 (N/m)	5.9×10^9
r_2 (mm)	400.4	k_2 (N/m)	5.9×10^9
m_1 (kg)	181.6	k_h (N/m)	16.9×10^9
m_2 (kg)	104		

4.6.2 No impact

Tooth separation between the gear pair was not observed when the relative displacement at the gear meshing point, δ (Eq. 4.10), was always greater than the backlash. The geared system meets this condition when the gears are heavily loaded. To study the no-impact condition, a simulation was conducted using the same parameters (Table 4.1), and under the excitation of heavy loads, $T_{in} = 4 \times 10^4 N.m$ and $T_{out} = 7.4 \times 10^4 N.m$, respectively.

The mean and standard deviation of the displacements in the y_1, y_2, and z directions are shown in Figures 4.2-4.4, respectively. These results demonstrate that the value of the mean and standard deviation of the energy-based SL and the Monte Carlo simulations are in agreement. This proves that, in the heavy load condition,

the SL method gives accurate results. A probability density function (PDF) of the system, based on the energy-based SL and MSC for t=0.03 s, is shown in Figure 4.5. From the figure, one can discover that the system solved by the linearization method and the Monte Carlo simulations operate outside of the backlash region. This demonstrates that the heavy load condition system works in the linear condition and that both methods provide similar results.

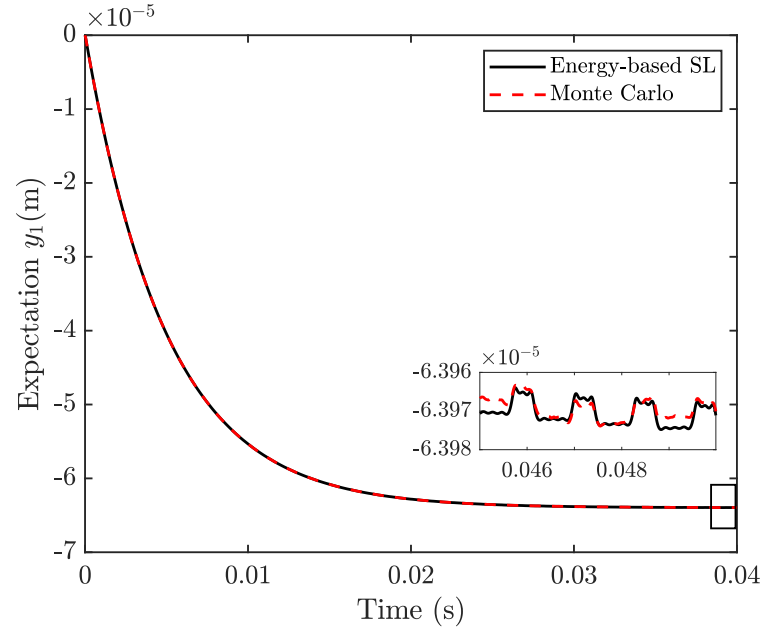

(a) Mean of displacement

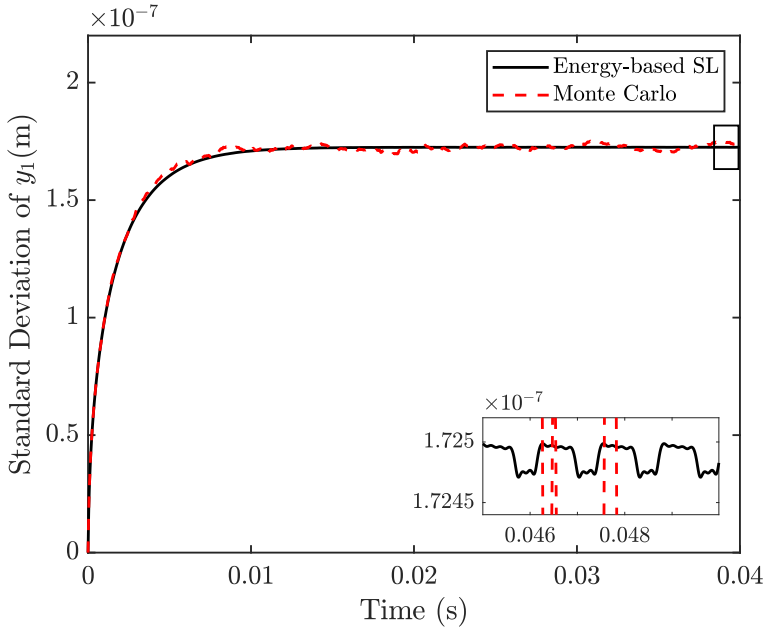

(b) Standard deviation of displacement

Figure 4.2: Displacement obtained by energy-based SL and MCS at y_1 direction for $T_{in} = 4 \times 10^4 N.m.$

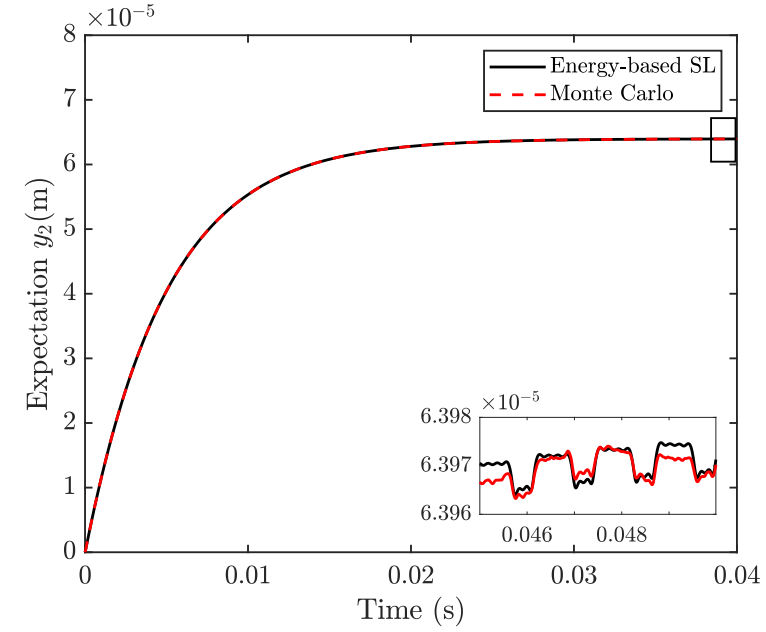

(a) Mean of displacement

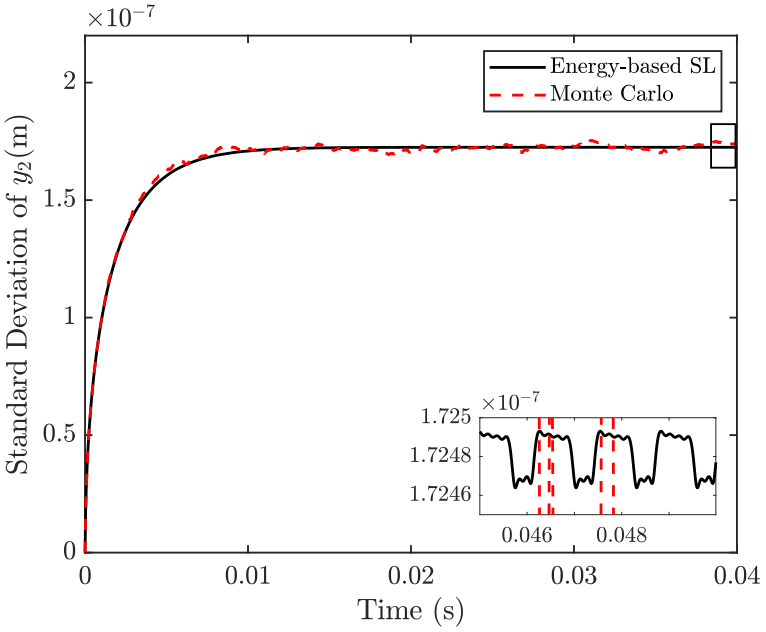

(b) Standard deviation of displacement

Figure 4.3: Displacement obtained by energy-based SL and MCS at y_2 direction for $T_{in} = 4 \times 10^4 N.m.$

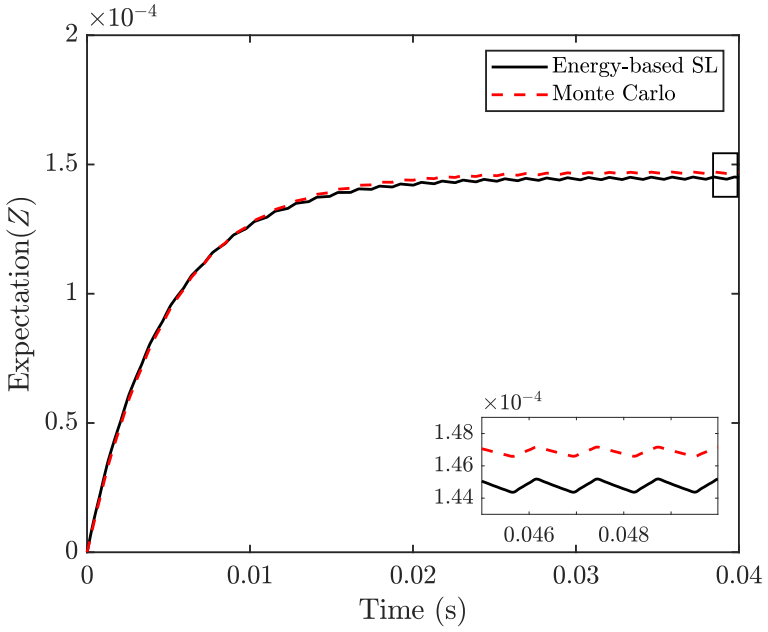

(a) Mean of displacement

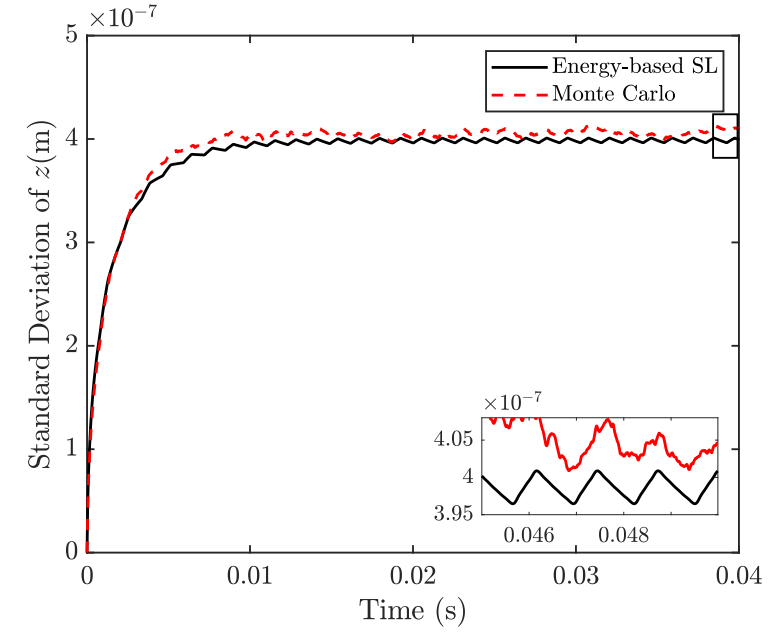

(b) Standard deviation of displacement

Figure 4.4: Displacement obtained by energy-based SL and MCS at z direction for $T_{in} = 4 \times 10^4 N.m.$

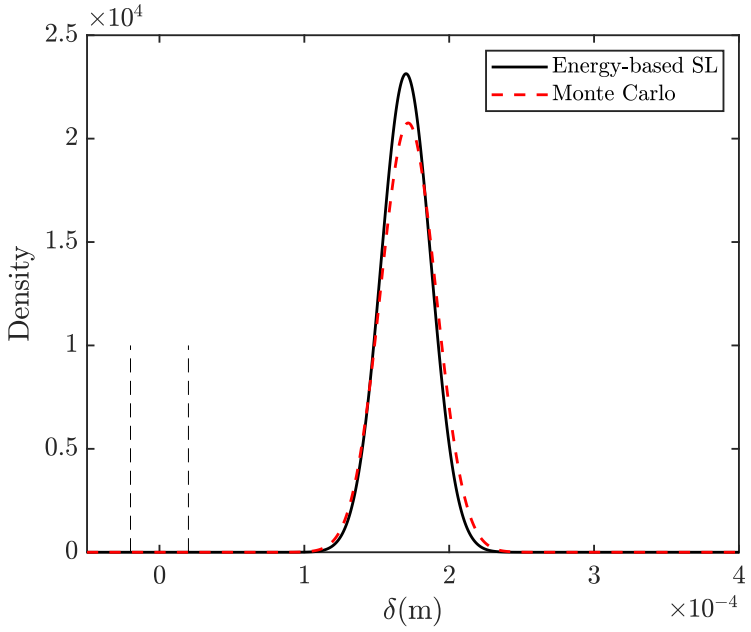

Figure 4.5: Probability density function obtained by energy-based SL and MCS at δ for $T_{in} = 4 \times 10^4 N.m$.

4.6.3 Single-sided impact

Based on Eq. 4.9, the single-sided impact case exist when δ becomes less than b but still greater than $-b$. Thus, in this case, the gear pair works on one side of the backlash region and loses its contact during a particular time. To reach this operating condition, $T_{in} = 4 \times 10^3 N.m$ and $T_{out} = 7.4 \times 10^3 N.m$ are applied.

The mean and standard deviation of displacements are represented in figure 4.6-4.8, and the obtained results in the y_1 and y_2 directions agree well with the the Monte Carlo simulations' results. From Figure 4.8, the mean and standard deviation of displacement of the z direction does not agree well with the Monte Carlo simulations.

This means that the intensity of the load affects the accuracy of the SL method, and when the system operates in backlash zone, the responses included the errors. A probability density function of the system, based on statistical linearization methods and the Monte Carlo simulations for t=0.03 s, is shown in Figure 4.9, and both methods show that the system operates in single-sided impact.

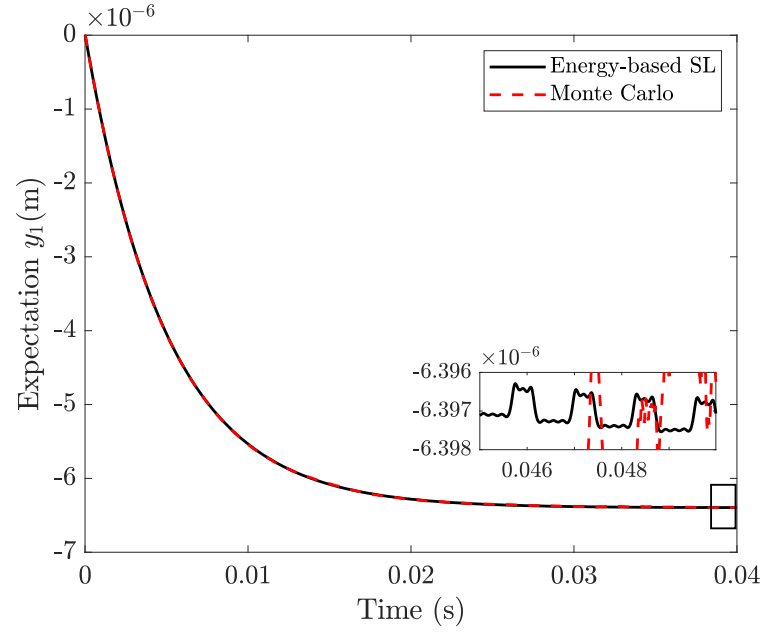

(a) Mean of displacement

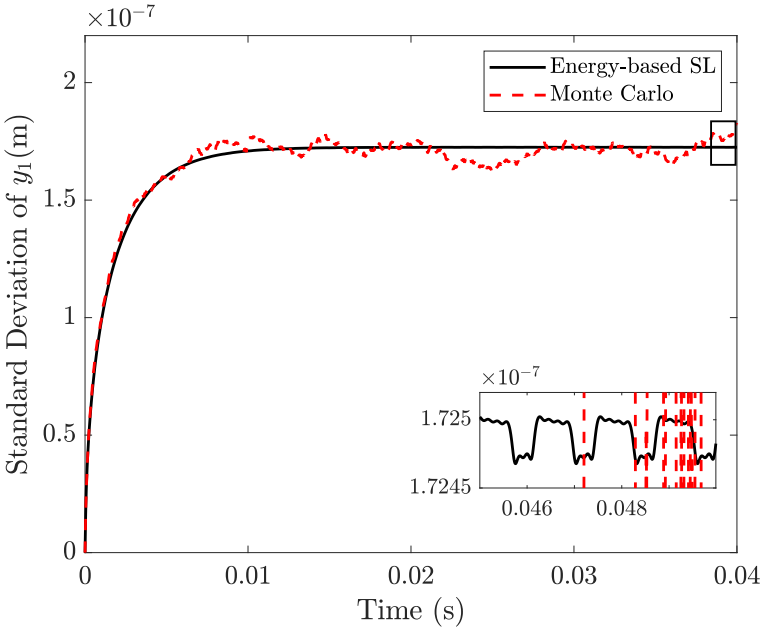

(b) Standard deviation of displacement

Figure 4.6: Displacement obtained by energy-based SL and MCS at y_1 direction for $T_{in} = 4 \times 10^3 N.m.$

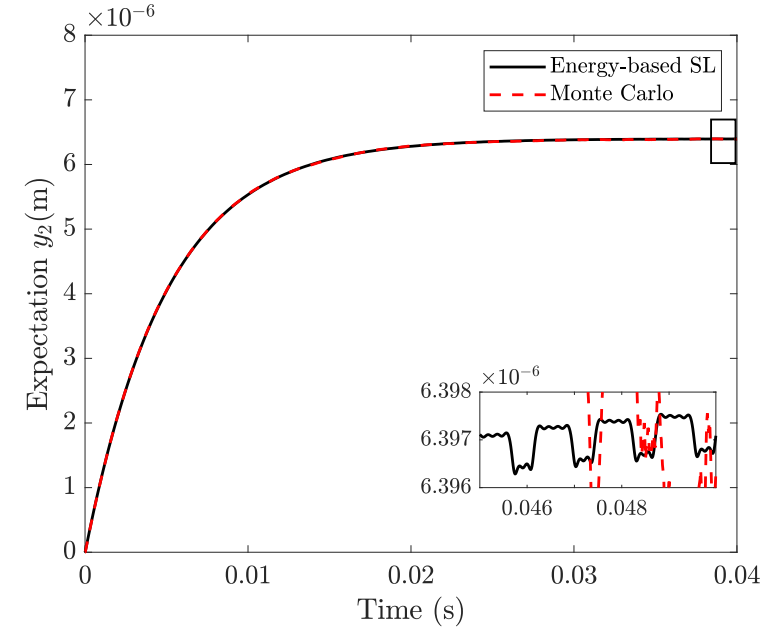

(a) Mean of displacement

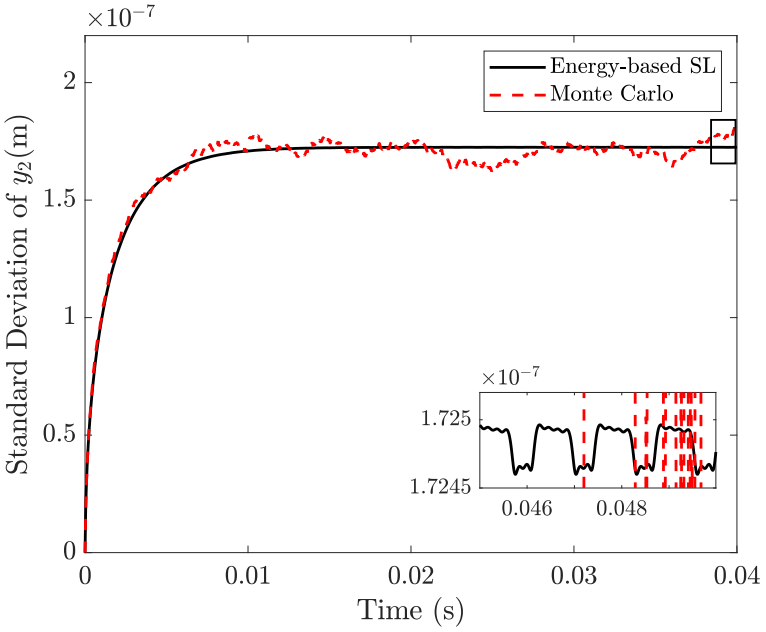

(b) Standard deviation of displacement

Figure 4.7: Displacement obtained by energy-based SL and MCS at y_2 direction for $T_{in} = 4 \times 10^3 N.m.$

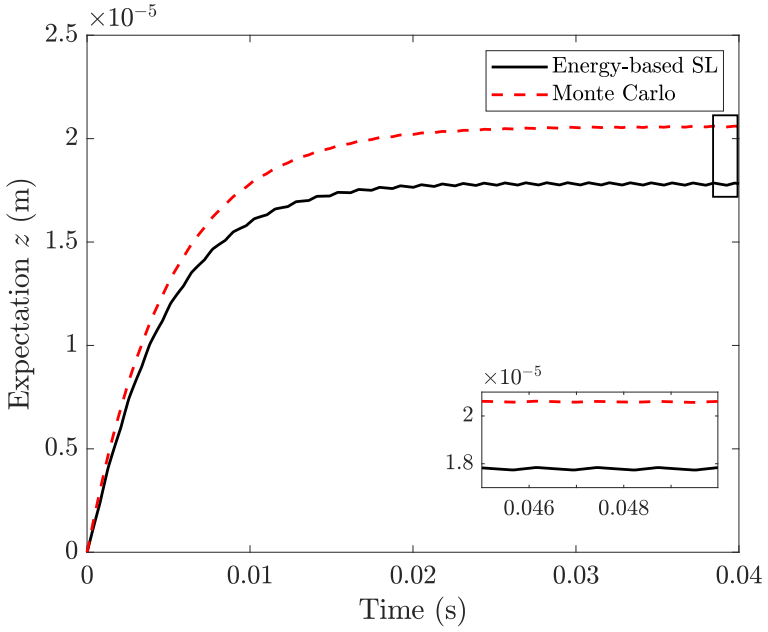

(a) Mean of displacement

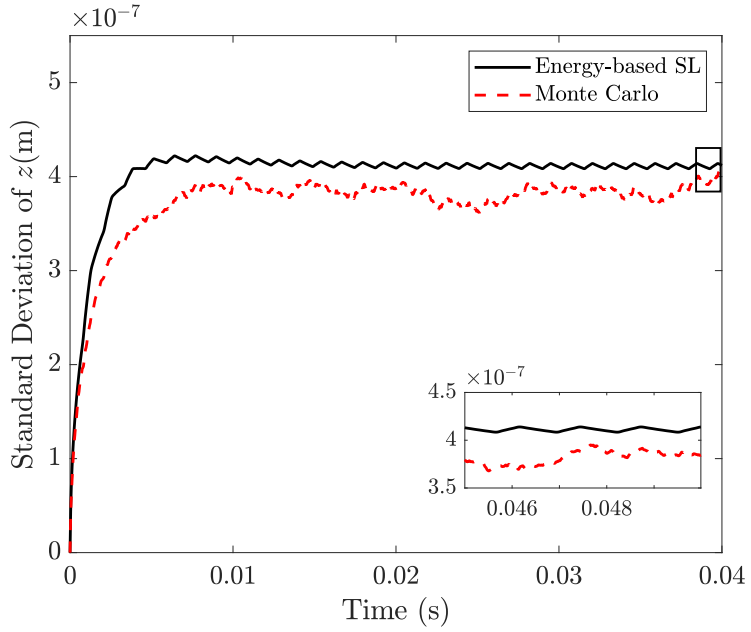

(b) Standard deviation of displacement

Figure 4.8: Displacement obtained by energy-based SL and MCS in z direction for $T_{in} = 4 \times 10^3 N.m.$

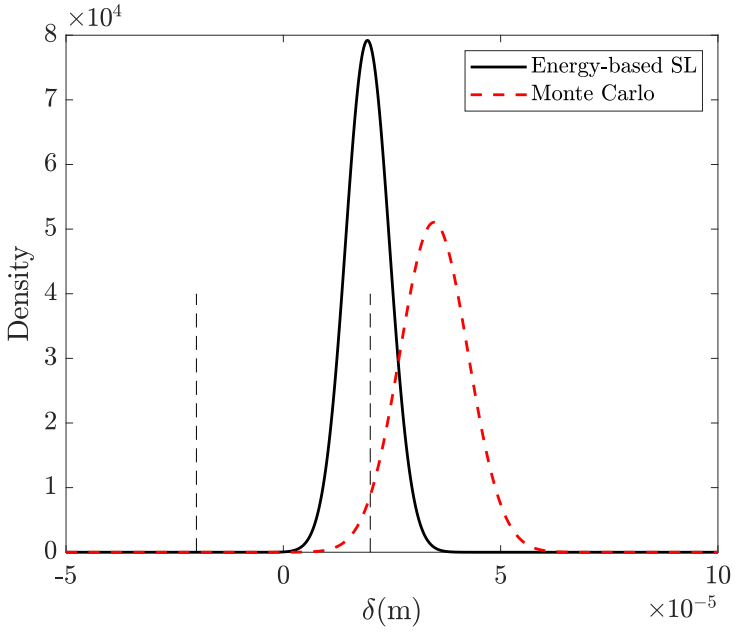

Figure 4.9: Probability density function obtained by energy-based SL and MCS at δ for $T_{in} = 4 \times 10^3 N.m$.

4.6.4 Double-sided impact

According to Eq. 4.9, double-sided tooth impact is observed when δ varies to the region of less than $-b$ during a certain period of time. The light load condition causes the geared system to operate in the entire backlash region. Thus, to have a double-sided impact condition, torques $T_{in} = 800N.m$ and $T_{out} = 1480N.m$ were applied.

The mean and standard deviation of displacements are represented in Figure 4.10-4.12. Although the mean and standard deviation at y_1 and y_2 obtained from energy-based SL are partially in agreement to the obtained results from the Monte Carlo

simulations, in comparison with no impact and single-side impact, the results have more error. From Figure 4.12, there is an error between the mean and standard deviation of displacement in the z direction when using the the Monte Carlo simulations. The reason is that when the geared system is under a light load condition, the system becomes strongly nonlinear. A probability density function of the system is shown in Figure 4.13. The obtained results from statistical linearization and the Monte Carlo simulations show that the system operates in double-sided impact conditions, although the results do not fully agree with the Monte Carlo simulations.

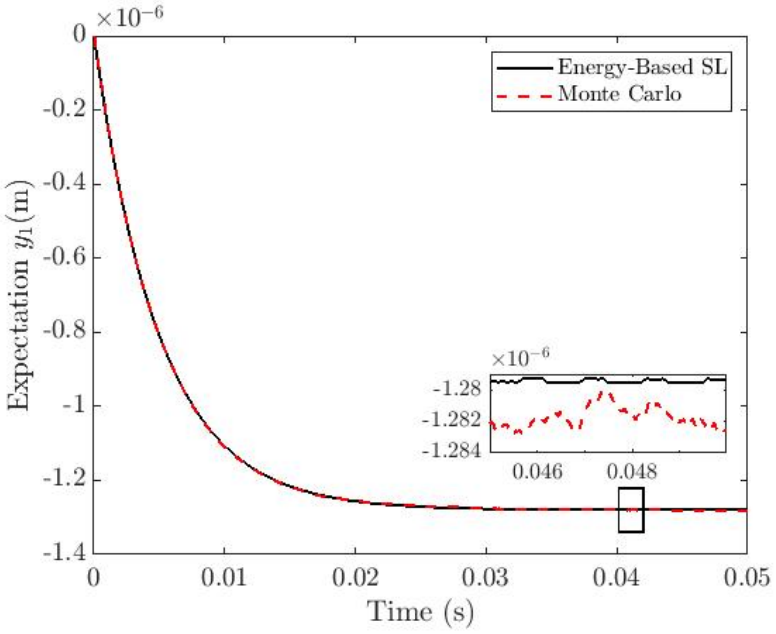

(a) Mean of displacement

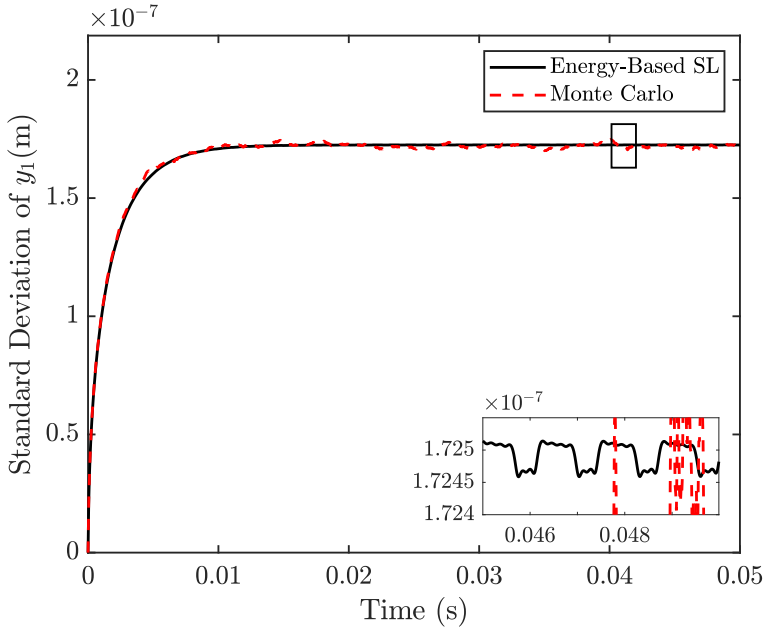

(b) Standard deviation of displacement

Figure 4.10: Displacement obtained by energy-based SL and MCS at y_1 direction for $T_{in} = 800N.m.$

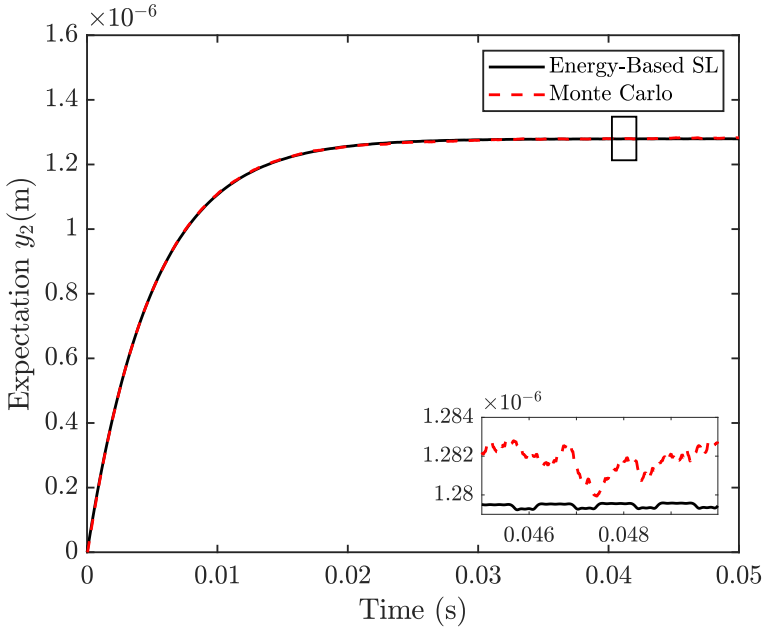

(a) Mean of displacement

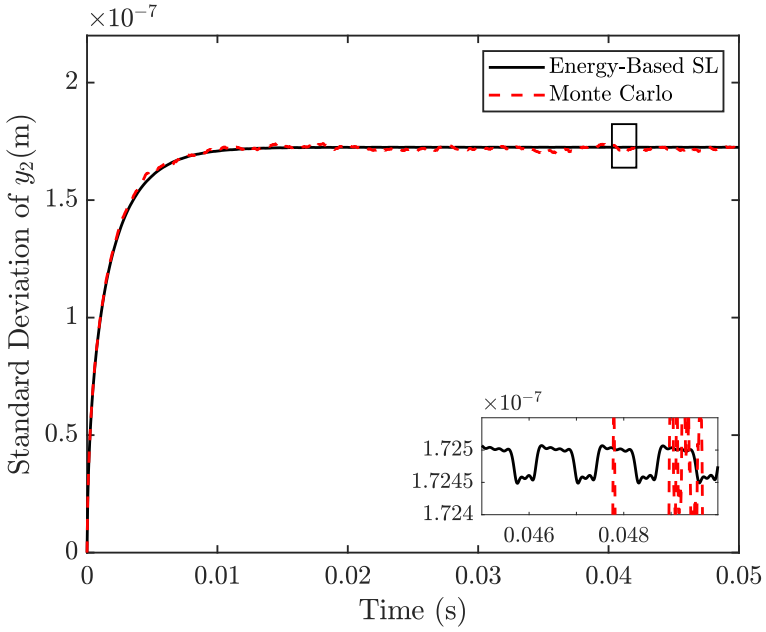

(b) Standard deviation of displacement

Figure 4.11: Displacement obtained by energy-based SL and MCS at y_2 direction for $T_{in} = 800N.m$.

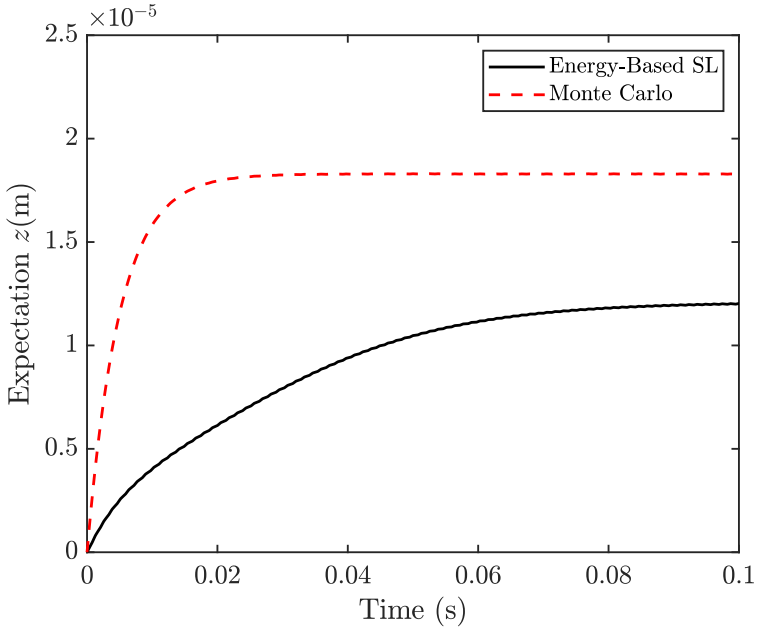

(a) Mean of displacement

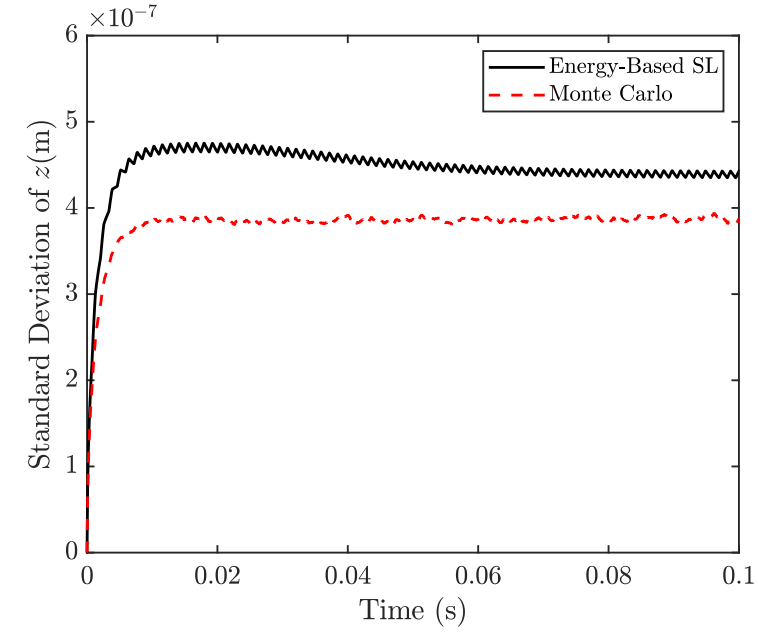

(b) Standard deviation of displacement

Figure 4.12: Displacement obtained by energy-based SL and MCS at z direction for $T_{in} = 800N.m$.

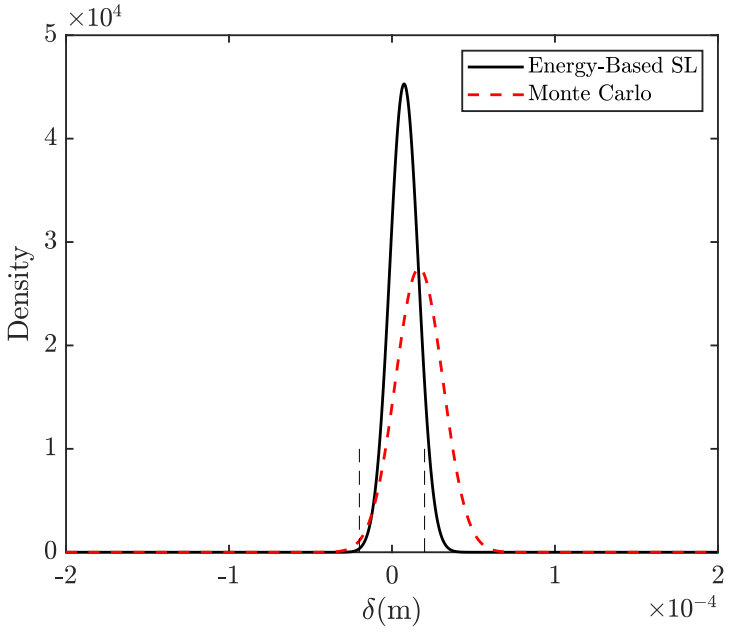

Figure 4.13: Probability density function obtained by energy-based SL and MCS at δ for $T_{in} = 800N.m$.

A comparison of the computational time between the statistical linearization method and Monte Carlo simulations showed that MCS required 8 hours to evaluate the response for 20,000 simulations, and SL methods took 35 seconds for the same function with the same computer (CPU i7-8700 3.2Ghz/16GB RAM).

4.7 Conclusion

The energy-based statistic linearization method is introduced in this paper to analyze the vibration of spur gears under both deterministic and random excitation. The underlying theory of energy-based statistic linearization methods are based on the

potential energy of the system, and give equivalent linear equations for the nonlinear system. The effect of the torque on dynamic behavior was investigated.

A comparison of the results with the Monte Carlo simulations demonstrates the different degrees of accuracy for various excitation levels. In the linear and no-impact conditions, SL returns a very similar result with the Monte Carlo simulations. This is because the linearization technique is more effective when the gears work in the linear conditions; an equivalent system is in agreement to the original system. For single-sided impact conditions, the energy-based SL shows agreement results in y_1 and y_2 directions, although the obtained results in the z direction are slightly different from the Monte Carlo simulations' result. The reason is that the z direction includes the nonlinear part, and the SL method cannot accurately represent the system nonlinearity. In light load conditions, the results show double-sided tooth impact. In this condition, the obtained results from the SL method agree less with the obtained results from the Monte Carlo simulations. This means that, under light load conditions, the SL method cannot precisely represent the nonlinear system. Finally, the results demonstrate that the statistical linearization method is accurate and valid for stochastic nonlinear geared systems under heavy load conditions such as planetary gear transmission in wind turbines.

4.A Appendix A

4.A.1 Expectation of first-order derivative of $P(\delta)$:

ased on Eq. 4.21, an expectation of the first-order derivative of $P(\delta)$ is given as:

$$E\left[\frac{\partial P(\delta)}{\partial \delta}\right] = \int_{-\infty}^{\infty} \frac{\partial P(\delta)}{\partial \delta} g(\delta) d\delta \tag{4.67}$$

By getting the integration by parts of the right side of Eq. 4.67, the following equation is obtained:

$$\int_{-\infty}^{\infty} \frac{\partial P(\delta)}{\partial \delta} g(\delta) d\delta = P(\delta)g(\delta) - \int_{-\infty}^{\infty} P(\delta) \frac{\partial g(\delta)}{\partial \delta} d\delta \tag{4.68}$$

Taking advance of $P(\delta)g(\delta) \to 0$ when the δ trends to infinity and incorporating Eq. 4.68 into Eq. 4.67 leads to:

$$E\left[\frac{\partial P(\delta)}{\partial \delta}\right] = -\int_{-\infty}^{\infty} P(\delta) \frac{\partial g(\delta)}{\partial \delta} d\delta \tag{4.69}$$

The first-order derivative of Gaussian function is given as:

$$\frac{\partial g(\delta)}{\partial \delta} = -\frac{1}{\sigma^2}(\delta - \delta_0) g(\delta) \tag{4.70}$$

Inserting Eq. 4.70 into 4.69 gives:

$$E\left[\frac{\partial P(\delta)}{\partial \delta}\right] = \frac{1}{\sigma^2} \int_{-\infty}^{\infty} P(\delta) \left(\delta - \delta_0\right) g(\delta) d\delta \tag{4.71}$$

Knowing that $\hat{\delta} = \delta - \delta_0$, Eq. 4.71 can be written as:

$$E\left[\frac{\partial P(\delta)}{\partial \delta}\right] = \frac{1}{\sigma^2}\int_{-\infty}^{\infty} P(\delta)\hat{\delta}g(\delta)d\delta \tag{4.72}$$

The right side of the Eq.4.72 is the definition of the expectation thus:

$$E\left[\frac{\partial P(\delta)}{\partial \delta}\right] = \frac{1}{\sigma^2}E\left[P(\delta)\hat{\delta}\right] \tag{4.73}$$

Finally, Eq. 4.73 can be written as:

$$E\left[P(\delta)\hat{\delta}\right] = \sigma^2 E\left[\frac{\partial P(\delta)}{\partial \delta}\right] \tag{4.74}$$

4.A.2 Expectation of second-order derivative of $P(\delta)$:

Taking derivation from Eq. 4.71 gives the expectation of second-order derivative of $P(\delta)$ as:

$$E\left[\frac{\partial^2 P(\delta)}{\partial \delta^2}\right] = -\frac{1}{\sigma^2}\int_{-\infty}^{\infty} \frac{\partial P(\delta)}{\partial \delta}(\delta - \delta_0)g(\delta)d\delta \tag{4.75}$$

By getting the integration by parts of the right side of Eq. 4.75 and taking advance of $P(\delta)g(\delta) \to 0$ when the δ trends to infinity, the following equation is obtained:

$$E\left[\frac{\partial^2 P(\delta)}{\partial \delta^2}\right] = \frac{-1}{\sigma^2}\int_{-\infty}^{\infty} P(\delta)\frac{\partial}{\partial \delta}\left[(\delta - \delta_0)\, g(\delta)\right] d\delta \tag{4.76}$$

The derivative part of the right side of Eq. 4.76 is given as:

$$\frac{\partial}{\partial\delta}\left(\left(\delta-\delta_0\right)g(\delta)\right)=g(\delta)-\frac{\left(\delta-\delta_0\right)^2}{\sigma^2}g(\delta) \tag{4.77}$$

Inserting Eq. 4.77 into Eq. 4.76 and applying $\hat{\delta}=\delta-\delta_0$ gives:

$$E\left[\frac{\partial^2 P(\delta)}{\partial\delta^2}\right]=\frac{1}{\sigma^2}\int_{-\infty}^{\infty}P(\delta)g(\delta)\left(\frac{\hat{\delta}^2}{\sigma^2}-1\right)d\delta \tag{4.78}$$

Based on expectation definition (Eq. 4.21), the Eq. 4.78 can be written as:

$$E\left[\frac{\partial^2 P(\delta)}{\partial\delta^2}\right]=\frac{1}{\sigma^4}E\left[P(\delta)\hat{\delta}^2\right]-\frac{1}{\sigma^2}E\left[P(\delta)\right] \tag{4.79}$$

Also, Eq. 4.79 can be written in following form:

$$E\left[P(\delta)\hat{\delta}^2\right]=\sigma^4 E\left[\frac{\partial^2 P(\delta)}{\partial\delta^2}\right]+\sigma^2 E\left(P(\delta)\right) \tag{4.80}$$

4.B Appendix B

Applying the definition of expectation on Eq. 4.9 gives:

$$E\left[f(\delta)\right]=\int_{-\infty}^{-b}k_h(\delta+b)g(\delta)d\delta+\int_{b}^{\infty}k_h(\delta-b)g(\delta)d\delta \tag{4.81}$$

$$E\left[f(\delta)\right]=k_h\left[\int_{-\infty}^{\infty}\delta g(\delta)d\delta-\int_{-b}^{b}\delta g(\delta)d\delta+b\int_{-\infty}^{-b}g(\delta)d\delta-b\int_{b}^{\infty}g(\delta)d\delta\right] \tag{4.82}$$

$$V=\frac{\delta-E\left[\delta\right]}{\sqrt{2}\sigma} \tag{4.83}$$

$$E\left[f(\delta)\right]=k_h\left[\frac{1}{\sqrt{2\pi\sigma}}\int_{-\infty}^{\infty}(\sqrt{2}\sigma V+\mu)e^{-y^2}\sqrt{2}\sigma dV-\frac{1}{\sqrt{2\pi\sigma}}\int_{V_1}^{V_2}(\sqrt{2}\sigma V+\mu)e^{-V^2}\sqrt{2}\sigma dV\right.$$
$$\left.+\frac{b}{\sqrt{2\pi}\sigma}\left(\int_{-\infty}^{V_1}e^{-V^2}\sqrt{2}\sigma dV-\int_{V_2}^{\infty}e^{-V^2}\sqrt{2}\sigma dV\right)\right] \quad (4.84)$$

$$E[f(\delta)]=k_h\left[E\left[\delta\right]-\frac{E\left(\delta\right)}{2}(erf(V_2)-erf(V_1))-\frac{\sigma}{\sqrt{2\pi}}(e^{-V_1^2}-e^{-V_2^2})+\frac{b}{2}(erf(V_1)+erf(V_2))\right] \quad (4.85)$$

Incorporating $E\left[f(\delta)\right]=f_0$ and $E\left[\delta\right]=\delta_0$:

$$f_0=k_h\left[\frac{\delta_0}{2}\left(2+erf\left(V_1\right)-erf\left(V_2\right)\right)-\frac{\sigma}{\sqrt{2\pi}}\left(e^{-V_1^2}-e^{-V_2{}^2}\right)+\frac{b}{2}\left(erf\left(V_1\right)+erf\left(V_2\right)\right)\right] \quad (4.86)$$

References

[1] Özgüven H N, Houser DR. Mathematical models used in gear dynamics—a review. Journal of sound and vibration. 1988; 121(3): 383–411

[2] Wang J, Li and R, Peng X. Survey of nonlinear vibration of gear transmission systems. Applied Mechanics Reviews. 2003 May 1;56(3):309-29.

[3] Zhang Y, Spanos P D. Efficient response determination of a mdof gear model subject to combined periodic and stochastic excitations. International Journal of Non-Linear Mechanics. 2020; 120: 103378

[4] Cooley CG, Parker RG. A review of planetary and epicyclic gear dynamics and vibrations research. Applied Mechanics Reviews. 2014 Jul 1;66(4).

[5] Philippe V. On the modelling of spur and helical gear dynamic behaviour. Mechanical Engineering. 2012 Apr 11:75.

[6] Kahraman A, Blankenship GW. Experiments on nonlinear dynamic behavior of an oscillator with clearance and periodically time-varying parameters. Journal of Applied Mechanics. 1997 Mar 1;64:217-26.

[7] Remmers EP. Gear mesh excitation spectra for arbitrary tooth spacing errors, load and design contact ratio. Journal of Mechanical Design. 1978 Oct 1;100(4):715-22.

[8] Booton RC. Nonlinear control systems with random inputs. IRE Transactions on Circuit Theory. 1954 Mar;1(1):9-18.

[9] Brückner A, Lin YK. Generalization of the equivalent linearization method for non-linear random vibration problems. International journal of non-linear mechanics. 1987 Jan 1;22(3):227-35.

[10] Elishakoff I, Fang J, Caimi R. Random vibration of a nonlinearly deformed beam by a new stochastic linearization technique. International journal of solids and structures. 1995 Jun 1;32(11):1571-84.

[11] Sobiechowski C, Socha L. Statistical linearization of the Duffing oscillator under non-Gaussian external excitation. Journal of Sound and vibration. 2000 Mar 16;231(1):19-35.

[12] TOBE T, SATO K. Statistical analysis of dynamic loads on spur gear teeth. Bulletin of JSME. 1977;20(145):882-9.

[13] TOBE T, SATO K, TAKATSU N. Statistical analysis of dynamic loads on spur gear teeth: experimental study. Bulletin of JSME. 1977;20(148):1315-20.

[14] Yang J. Vibration analysis on multi-mesh gear-trains under combined deterministic and random excitations. Mechanism and Machine Theory. 2013 Jan 1;59:20-33.

[15] Kahnamouei, J. T., Yang, J.: Development and verification of a computationally efficient stochastically linearized planetary gear train model with ring elasticity, Mechanism and Machine Theory. 2021 Jan 1; 155, 104061.

[16] Neriya S, Bhat R, Sankar T. On the dynamic response of a helical geared system subjected to a static transmission error in the form of deterministic and filtered white noise inputs. Journal of Vibration and Acoustics. 1988 Oct 1;110(4):501–506.

[17] Naess A, Kolnes FE, Mo E. Stochastic spur gear dynamics by numerical path integration. Journal of sound and vibration. 2007 May 22;302(4-5):936-50.

[18] Hasnijeh SG, Poursina M, Leira BJ, Karimpour H, Chai W. Stochastic dynamics of a nonlinear time-varying spur gear model using an adaptive time-stepping path integration method. Journal of Sound and Vibration. 2019 May 12;447:170-85.

[19] Maatar M , Velex P. An analytical expression for the time-varying contact length in perfect cylindrical gears: some possible applications in gear dynamics. The Journal of Mechanical Design. 1996 December 1; 118(4): 586-589.

[20] Socha L. Linearization methods for stochastic dynamic systems. Springer Science & Business Media; 2007 December 20.

[21] Bernard P, Fleury G. Stochastic newmark scheme. Probabilistic engineering mechanics. 2002 Jan 1;17(1):45-61.

[22] Zhang L, Zu J, Zheng Z. The stochastic newmark algorithm for random analysis of multi-degree-of-freedom nonlinear systems. Computers & structures. 1999 Mar 1; 70(5): 557–568

[23] Bucher C. Computational analysis of randomness in structural mechanics: Structures and infrastructures book series, vol. 3. Crc Press (2009)

Chapter 5

Free Vibration Properties of Ring Gears

Jalal Taheri Kahnamouei, Ph.D. Candidate

Jianming Yang, Associate Professor

Faculty of Engineering and Applied Science, Memorial University ofNewfoundland,

St. John's, NL, Canada AlB 3X5

This chapter was presented as a paper to the Canadian Society for Mechanical Engineering and CFD Society of Canada International Congress 2019 (CSME-CFDSC Congress 2019), June 2-5, 2019, London, On, Canada.

In this chapter, the new model was proposed to represent an elastic ring gear accurately. In addition, analytical results from published paper verified the accuracy of the curve beam element for modeling smooth ring, and compare results with Ansys to determine the accurate model were conducted.

Abstract

Ring gears are used in many applications, planetary gear trains (PGTs) in particular. The ring gear dynamic properties have a significant effect on the overall dynamics of the system with ring gears installed. This paper proposes two models developed to compute the natural frequencies and mode shapes of a ring gear. In Model I, the ring gear is modeled as a smooth ring without attached masses, and in Model II, the ring gear modeled as a smooth ring with attached masses. In both models, curved beam elements are used to model the smooth ring. The results are compared against those from ANSYS, and show that Model II gives more accurate results.

Keywords: curve beam element, natural frequency, ring gear

5.1 Introduction

Planetary gear trains (PGTs) are widely used in many fields, such as aerospace, automation, and energy. The dynamics of PGTs in operation is critical to safety and performance; thus, many studies have been conducted on the general aspects of PGT dynamics [1, 2].

With increasing operational speeds, the dynamic deformation of ring gear has become an outstanding issue. Thus, the free vibration characteristics of the ring, including natural frequencies and mode shapes, need to be examined carefully in the design stage. In the open literature, most research modeled the ring gear as

a smooth curved beam or as a thin-walled circular ring. For example, Mallik and Mead [3] analyzed the natural frequencies and mode shapes of the in-plane vibration of thin-wall rings by using a wave technique. Davis et al. [4] considered the shear deformation of ring gear and employed the two-node curved beam finite element model. Yand [5] and Wu [6] applied the finite element method to dynamic responses with the curved beam theory. Petyt, and Fleischer [7] carried out an analysis of the free radial vibration of the ring by using a 3D finite element model with curved beam elements under different boundary conditions. Sabir, and Ashwell [8] studied the in-plane vibration of a curved beam using the finite element method. A real ring gear, in fact, is not smooth; rather, there are gear teeth on the ring. Some researchers have noticed that a smooth ring with a uniform cross-section might be an oversimplification; thus, the results based on this model are questionable in some cases. Tanna, and Lim [9] compared the modal frequencies and vibration modes of smooth rings against real ring gears, and Chen et al. [10, 11] studied the dynamic responses of elastic ring gear modeled by a curved Timoshenko beam.

This paper investigates the free vibration of a ring gear using proposed models to calculate a quantitative figure of the effect of the gear teeth on ring dynamics. First, the ring gear is modeled as a smooth ring with no attachments. Second, the ring gear is assumed to have rim and teeth, where the rim is modeled as a smooth ring, and lumped-masses represent each tooth. In both models, the finite element method is used. The results obtained from the two methods are then compared against data

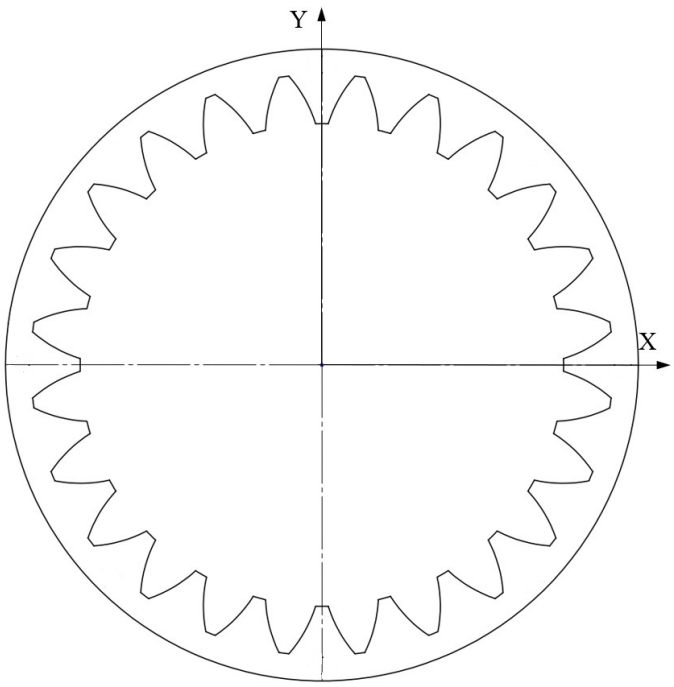

Figure 5.1: Model of a ring gear

from a published paper [12]. It indicates that the results from the second method are more accurate than the first method.

5.2 Dynamic Model

A ring gear under investigation in this paper is shown in Figure 5.1. For the purpose of FE modeling in later sections, a global coordinate frame XYZ is placed at the ring's center, with the Z-axis perpendicular to the XY plane.

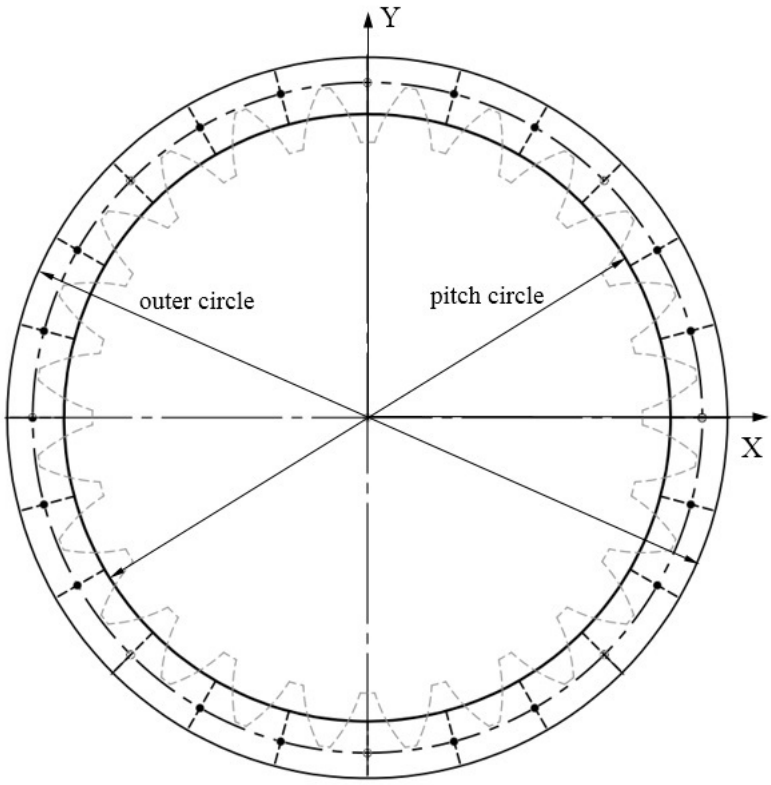

(a) A smooth ring model

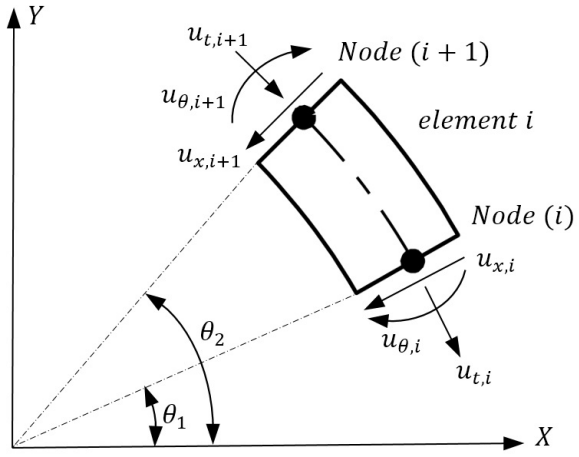

(b) A curved-beam element of ring

Figure 5.2: Model I

5.2.1 Model I

In this model, the ring gear is modeled as a smooth elastic ring with a uniform cross-section. The outer diameter (OD) of the ring is taken as the same as the ring gear, while the inner diameter (ID) of the ring is taken as the diameter of the pitch circle, as shown in Figure 5.2a. The ring is first divided into curved beam elements. For convenience, the number of elements is chosen to be equal to the number of teeth. An element is shown in Figure 5.2b, and a local coordinate frame, including the radial, tangential, and rotational directions, is defined. The six degrees of freedom of the element include u_x, u_t, and u_θ for both nodes. The method in [13] is employed to achieve the element mass and stiffness matrices, which gives:

$$[k] = \frac{EI}{R^3}\,[V]\,[Q]^{-1} \tag{5.1}$$

$$[m] = \rho R[Q]^{-1^T}\int_{\theta_1}^{\theta_2}[P]^T[\Lambda][P]d\theta[Q]^{-1} \tag{5.2}$$

where m is mass matrices, and k is the stiffness matrices. I is the moment of inertia, E is the module of elasticity, and ρ is the and the mass density of the material. Λ, Q, V, and P are complex parameters, which are not provided here to save space

(interested readers can find these parameters in [13] in the following).

$$[V] = \begin{bmatrix} 0 & 0 & 0 & 2\sin\theta_1 & 0 & 2\cos\theta_1 \\ 0 & 0 & 0 & 2\cos\theta_1 & 1 & 2\sin\theta_1 \\ R & 0 & 0 & 2R\cos\theta_1 & R^{-1} & 2R\sin\theta_1 \\ 0 & 0 & 0 & 2\sin\theta_2 & 0 & 2\cos\theta_2 \\ 0 & 0 & 0 & 2\cos\theta_2 & 1 & 2\sin\theta_2 \\ R & 0 & 0 & 2R\cos\theta_2 & R^{-1} & 2R\sin\theta_2 \end{bmatrix} \tag{5.3}$$

$$[Q] = \begin{bmatrix} 1 & \cos\theta_1 & \sin\theta_1 & \theta_1\sin\theta_1 & 0 & \theta_1\cos\theta_1 \\ J\theta_1 & \sin\theta_1 & -\cos\theta_1 & \sin\theta_1 - \theta_1\cos\theta_1 & 1 & \cos\theta_1 + \theta_1\sin\theta_1 \\ J\theta_1 R^{-1} & 0 & 0 & 2R^{-1}\sin\theta_1 & R^{-1} & 2R^{-1}\cos\theta_1 \\ 1 & \cos\theta_2 & \sin\theta_2 & \theta_2\sin\theta_2 & 0 & \theta_2\cos\theta_2 \\ J\theta_2 & \sin\theta_2 & -\cos\theta_2 & \sin\theta_2 - \theta_2\cos\theta_2 & 1 & \cos\theta_2 + \theta_2\sin\theta_2 \\ J\theta_2 R^{-1} & 0 & 0 & 2R^{-1}\sin\theta_2 & R^{-1} & 2R^{-1}\cos\theta_2 \end{bmatrix} \tag{5.4}$$

$$[P] = \begin{bmatrix} 1 & \cos\theta & \sin\theta & \theta\sin\theta & 0 & \theta\cos\theta \\ J\theta & \sin\theta & -\cos\theta & \sin\theta - \theta\cos\theta & 1 & \cos\theta + \theta\sin\theta \\ J\theta R^{-1} & 0 & 0 & 2R^{-1}\sin\theta & R^{-1} & 2R^{-1}cos\theta \end{bmatrix} \tag{5.5}$$

$$J = 1 + \left(\frac{I}{AR^2}\right) \tag{5.6}$$

$$[\Lambda] = diag(A \;\; A \;\; I) \tag{5.7}$$

Assembling the equations of all elements gives the global equation:

$$[M]\left\{\ddot{U}\right\} + [K]\{U\} = 0 \tag{5.8}$$

where M is the global mass, K is the stiffness matrices, and U is the global displacement vector, which is defined as:

$$U = \{u_{x,1} \;\; u_{t,1} \;\; u_{\theta,1} \;\; \cdots \;\; u_{x,i} \;\; u_{t,i} \;\; u_{\theta,i}\} \tag{5.9}$$

5.2.2 Model II

In this model, the ring gear is modeled as a smooth ring with attached lumped masses, which represent the effect of the teeth. Each tooth is considered a lumped mass, including mass, m_T, and the moment of inertia around the axis through the center of the tooth, J_T, as shown in Figure 5.3a. The smooth ring is determined with an OD equivalent to that used in Model I, and an ID equal to the diameter of the dedendum circle. The mass and stiffness matrices of the smooth ring can be computed in the same way as Model I using Eqs. 5.1 and 5.2.

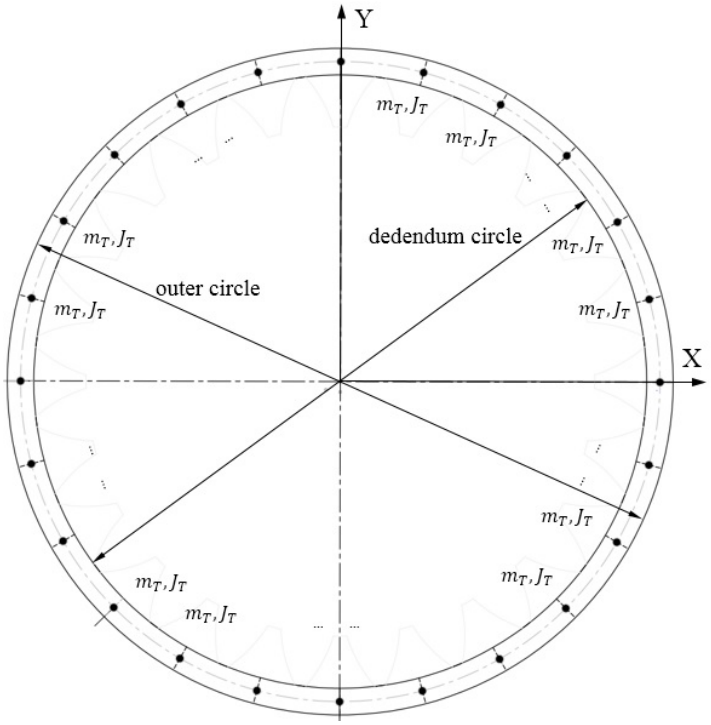

(a) A smooth ring with lumped-mass model

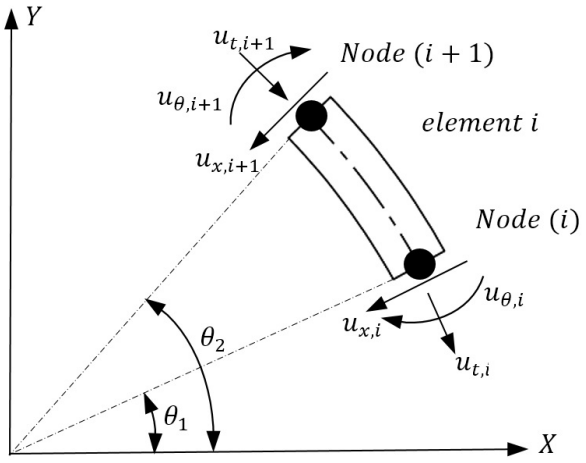

(b) A curved-beam element of ring

Figure 5.3: Model II

With the tooth masses and moments of inertia considered as lumped masses at-

tached to the FEM notes, as shown in Figure 5.4, then the internal forces at the two nodes of an element can be represented by the following:

$$F_{x,i} = F_{x,i+1} + m_T \ddot{u}_{x,i} \tag{5.10}$$

$$F_{t,i} = F_{t,i+1} + m_T \ddot{u}_{t,i} \tag{5.11}$$

$$M_{\theta,i} = M_{\theta,i+1} + J_T \ddot{u}_{\theta,i} \tag{5.12}$$

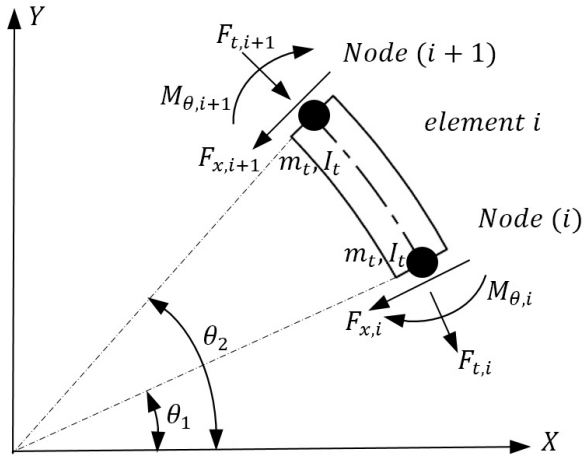

Figure 5.4: Internal forces of curved-beam element

$F_{x,i}$, $F_{t,i}$ and $M_{\theta,i}$ are the internal forces and moments of the elements and are given as:

$$F_x = F_t' \tag{5.13}$$

$$F_t = \frac{EA}{R}(u_x + u_t')\frac{M_\theta}{R} \tag{5.14}$$

$$M_\theta = \frac{EI}{R}(u_x + u_x'') \tag{5.15}$$

Based on Eqs. 5.10 to 5.12, assembling the equation of elements and boundary conditions gives the global equation as:

$$[M + M_T]\left\{\ddot{U}\right\} + [K]\{U\} = 0 \tag{5.16}$$

where

$$[M_T] = diag(m_T^1 \quad m_t^2 \quad \cdots \quad m_T^N) \tag{5.17}$$

$$[m_t] = diag(m_T \quad m_t \quad \cdots \quad m_T) \quad i = 1, \cdots, N \tag{5.18}$$

5.3 Simulation and Results

In this study, numerical examples have been conducted on a ring gear using both Model I and Model II. For comparison purposes, ANSYS is used in the analysis. The results and comparison against ANSYS are provided (see Figure 5.6). The geometry and material properties of the ring gear in the simulation are given in Table 5.1. Matlab software was used to determine the natural frequencies of both models.

Table 5.1: Ring gear properties

Parameters	Value
Outer radius (mm)	201.14
Root radius (mm)	182.8
$m_T(kg)$	0.028
$I_T(kg.m^3)$	554.8×10^{-9}
$\rho(kg/m^3)$	7858
$E(Pa)$	205×10^9
Number of teeth	64

Modal Analysis of ANSYS was used to determine the mode shapes and natural frequencies of the elastic ring gear. Three-dimensional solid model of ring gear was generated in SOLIDWORK and then exported to ANSYS. In the analysis, the material properties of gear were defined as material properties listed in Table 5.1 . According to the characteristics of the ring gear, 3-D 20-Node Structural Solid (SOLID186) was used in the model. The finite element model consisted of 2,672 elements and 16448 nodes. During the mesh generation process, numbers of elements have been chosen to obtain acceptable convergence, where the results' values improved unnecessarily by increasing the number of elements. The elaborated FE model of elastic ring gear was shown in Figure 5.5 . Because the models I and II are studied using in-plane vibration of the ring gear, mode shapes and natural frequencies - which are

bounded to in-plane- were considered. In addition, frequencies bounded to rigid body motion were ignored. Analysis of the obtained natural frequencies and modal shapes was conducted in the following section.

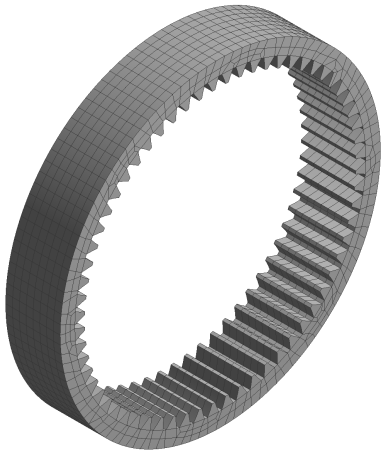

Figure 5.5: Ring gear finite element model

For validation of the curved beam element method, we compared the results Model I against published data [12]. In comparison, the natural frequencies were transformed into dimensionless values. All the dimensions and material properties used were taken from Wu [12]. Table 5.2 shows that the results from [12] and the curved beam element matched very well.

Table 5.2: Dimensionless natural frequencies of equally-supported rings compared with published data [12]

$\omega\sqrt{\frac{\rho AR^4}{EI_y}}$					
$\omega_{1,2}$	$\omega_{1,2}$[12]	$\omega_{3,4}$	$\omega_{3,4}$[12]	ω_5	ω_5[12]
1.640	1.643	7.529	7.589	10.205	10.465

Although the curved beam element is accurate in its computation of the dynamics of a smooth ring, its applicability to ring gear still needs to be verified. For the ring gear given in Table 5.1, the natural frequencies are calculated using Models I, II, and ANSYS. All results are given in Table 5.3. The relative errors of Models I and II against the ANSYS results are provided in Table 5.4. From Table 5.3, it is clear that all the results are quite close to those from ANSYS, however, the accuracies are different.

Table 5.3: Natural frequencies of ring gear obtained from Model I, II, and ANSYS

	Natural frequencies		
	ANSYS	Model I	Model II
1	590	641	601
2	1650	1811	1697
3	3129	3474	3242
4	4977	5631	5216
5	7166	8309	7605
6	9652	11527	10390

If ANSYS results are taken as benchmarks, the comparison in Table 5.4 clearly shows that Model II has much higher accuracy than that of Model I. For example, the relative error of Model I for the first six frequencies ranges from 8.6% to 19.4%, while for Model II the same problem gives a relative error between 1.8% and 7.6%.

Table 5.4: Errors between Model I, Model II, and ANSYS Results

	Natural frequencies		
	ANSYS vs. Model I	ANSYS vs. Model II	Model I vs. II
1	8.6 %	1.8 %	6.6 %
2	9.7 %	2.8 %	6.7 %
3	11.0 %	3.6 %	7.1 %
4	13.1 %	4.8 %	7.9 %
5	15.9 %	6.1 %	9.2 %
6	19.4 %	7.6 %	10.9 %

It is observed that all the natural frequencies from Model I are higher than those from Model II. This makes sense given that, in Model I, the tooth effect is neglected. While in Model II, each tooth is modeled as an attached mass and moment of inertia; thus, more accurate results can be obtained. It is reasonable to deduce that with the decrease of rim thickness, the results from Model I would have given even higher errors, and Model II would become a better model for ring gear dynamics. Figure 5.6 shows the mode shapes of the ring gear for the first six natural frequencies. As expected, mode shapes are less affected by the model methods.

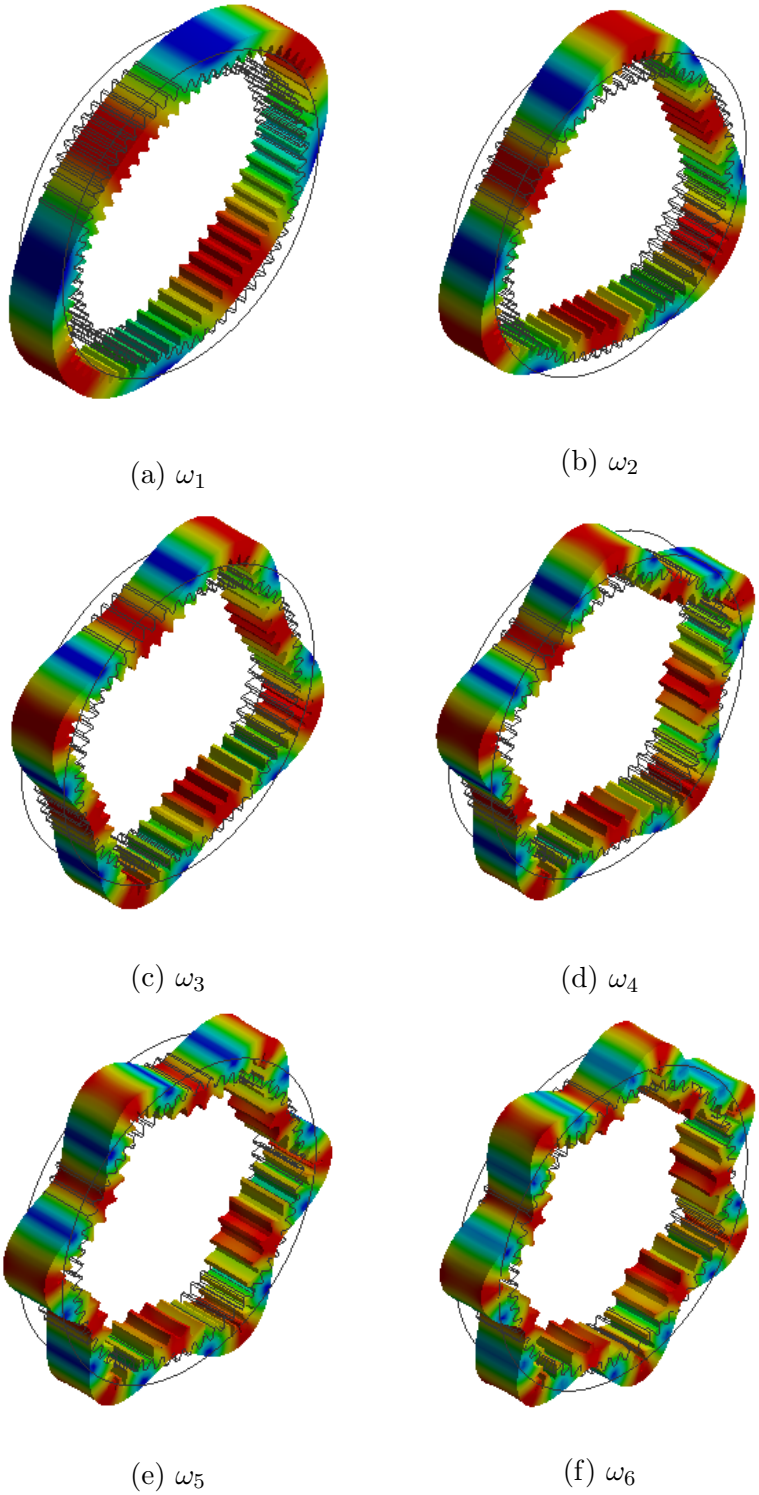

(a) ω_1 (b) ω_2

(c) ω_3 (d) ω_4

(e) ω_5 (f) ω_6

Figure 5.6: Ring gear's mode shapes from ANSYS

5.4 Conclusions

In this paper, free vibration of ring gears is studied using two models. Model I simplifies a ring gear as a smooth ring with the pitch circle diameter as the ID. Model II, however, treats ring gear as a smooth ring with the dedendum circle diameter as the ID, and each tooth is modeled as a mass and a moment of inertia. For computation, in both models, curved beam elements were used. And for verification purposes, the results were compared with ANSYS results as well. It is indicated that Model II is a better description of ring gear dynamics.

References

[1] Cooley CG, Parker RG. A review of planetary and epicyclic gear dynamics and vibrations research. Applied Mechanics Reviews. 2014 Jul 1;66(4).

[2] Yang J, Dai L. Survey of dynamics of planetary gear trains. International Journal of Materials and Structural Integrity. 2008 Jan 1;1(4):302-22.

[3] Mallik AK, Mead DJ. Free vibration of thin circular rings on periodic radial supports. Journal of Sound and Vibration. 1977 Sep 8;54(1):13-27.

[4] Davis R, Henshell RD, Warburton GB. Constant curvature beam finite elements for in-plane vibration. Journal of Sound and Vibration. 1972 Dec 22;25(4):561-76.

[5] Yang F, Sedaghati R, Esmailzadeh E. Free in-plane vibration of general curved beams using finite element method. Journal of sound and vibration. 2008 Dec 23;318(4-5):850-67.

[6] Wu JS, Lin FT, Shaw HJ. Free in-plane vibration analysis of a curved beam (arch) with arbitrary various concentrated elements. Applied Mathematical Modelling. 2013 Aug 1;37(14-15):7588-610.

[7] Petyt M, Fleischer CC. Free vibration of a curved beam. Journal of Sound and Vibration. 1971 Sep 8;18(1):17-30.

[8] Sabir AB, Ashwell DG. A comparison of curved beam finite elements when used in vibration problems. Journal of sound and vibration. 1971 Oct 22;18(4):555-63.

[9] Tanna RP, Lim TC. Modal frequency deviations in estimating ring gear modes using smooth ring solutions. Journal of sound and vibration. 2004;269(3-5):1099-110.

[10] Chen Z, Shao Y, Su D. Dynamic simulation of planetary gear set with flexible spur ring gear. Journal of sound and vibration. 2013 Dec 23;332(26):7191-204.

[11] Chen Z, Shao Y. Mesh stiffness of an internal spur gear pair with ring gear rim deformation. Mechanism and Machine Theory. 2013 Nov 1;69:1-2.

[12] Wu X, Parker RG. Vibration of rings on a general elastic foundation. Journal of Sound and Vibration. 2006 Aug 8;295(1-2):194-213.

[13] Wu JS, Chiang LK. Dynamic analysis of an arch due to a moving load. Journal of Sound and Vibration. 2004 Jan 22;269(3-5):511-34.

Chapter 6

Random Vibration Analysis of Thin-Walled Elastic Rings under Multiple Moving Loads

Jalal Taheri Kahnamouei, Ph.D. Candidate

Jianming Yang, Associate Professor

Faculty of Engineering and Applied Science, Memorial University ofNewfoundland,

St. John's, NL, Canada AlB 3X5

This chapter was submitted as a full research paper to the Journal of Proceedings of the Institution of Mechanical Engineers, Part C: Journal of Mechanical Engineering Science in November 2019 and currently is under review.

In this chapter, the influence of the random moving load on the ring gear deformation was studied. Our review of the previous literature about ring gear revealed a lack of research on random moving load on the ring. Therefore, I studied the elastic ring dynamic behavior under multiple random moving loads. Also, the analysis was carried out for various angular load velocities.

Abstract

This paper investigates the random vibration of a thin-walled ring subjected to multiple moving loads applied from the inside of the ring. A ring gear in a planetary gear train with three equally-spaced planets is taken as an example. The ring is discretized with the finite element method of curved beam elements. The supports of the ring gear are treated as three linear springs to mimic the general bolt connection. The stochastic Newmark algorithm is used to solve the equations, and to obtain the mean and variance of the responses. Monte Carlo simulations are also conducted to verify the results from the stochastic Newmark scheme. A parametric study is conducted to examine the effect of design parameters on the responses.

6.1 Introduction

Thin-walled ring structures are widely used in various engineering applications. Some of them are subjected to multiple moving loads. Typical examples include stators in electrical machinery, such as motors and generators, and ring gears in a planetary gear train (PGT). In some cases, the excitation loads have a random component. For example, the ring gear in a PGT of wind turbines is subjected to sequential meshing forces at the ring-planet mesh, which contains a periodic component and a random one. The dynamics of the ring in such applications significantly affects the performance of the machines in which it is embedded, and, thus, deserves a systematic

investigation.

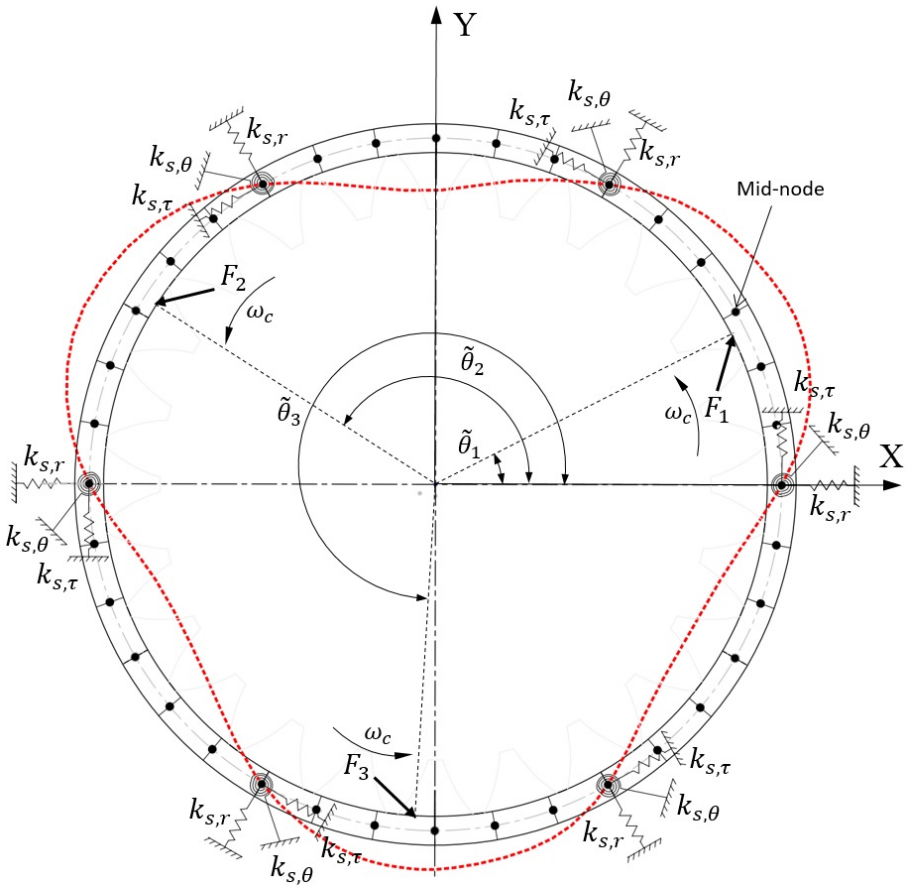

Figure 6.1: Ring Model (— represents the original ring, - - - represents the ring after deformation)

Interest in the ring dynamics is traced back to the 1970s. Plentiful of publications can be found in scientific journals and conference proceedings. Chidamparam and Leissa [1] reviewed the published works before 1993. Some recent representative works are as follows. Wu and Parker [2] studied the modal properties and natural frequencies of a thin-walled ring supported by a general flexible foundation using

Galerkin and perturbation methods. Tanna and Lim [3] studied the deviation of smooth rings and ring gears in free vibration characteristics. Wang et al. [4] examined the mode contamination and stability problems of a symmetric ring. Hu et al. [5] used the baseline model to predict the deformation of the ring gear and to analyze the influence of ring deformation on the dynamic response of planetary gearboxes.

Research on the vibration of rings (or curved beams) under moving loads is also found in the literature, such as [6-9]. In addition, Metrikine and Tochilin [10] investigated the steady-state response of an elastic ring under a moving load by an analytic method. They analyzed the effect of the load moving velocity on the ring patterns. Forbes and Randall [11] investigated the dynamic responses of a flexible ring under a moving load and analyzed the resonance phenomenon caused by the moving loads. Karttunen and Hertzen [12] analyzed the vibration response of a cylinder cover under circumferential-moving loads. They modeled the cover as a viscoelastic material and investigated the influence of single and twin loads with three different distributions. Canchi and Parker[13, 14] employed a rotating and non-rotating thin-walled ring to model and analyze the vibration and instability of a ring gear due to moving springs.

Despite the above-cited publications, there are no research works on the vibration of rings under random moving loads. This paper takes the ring gear of a PGT as the object and investigates its vibration under multiple moving random loads. The ring gear is simplified as a smooth ring which is modeled with curved beam elements. Three springs represent the supports of the ring gear. The multiple moving loads,

containing both random and deterministic components, are applied to the ring from the inside. The stochastic Newmark method is utilized to solve the equations. In addition, Monte Carlo Simulations (MCS) is also conducted to verify the results obtained from the Newmark method. The parametric study follows to investigate the effect of the main parameters on the vibration response.

6.2 Dynamical Model

A ring with a radius of R and a sectional area of A is illustrated in Figure 6.1. A certain number of loads, generally 3 to 5 for a PGT, move along the circumference with a constant speed, ω_c. The ring is assumed to be connected to the housing with a certain number of bolts, each of which is represented by three springs, k_r, k_τ and k_θ. A global coordinate frame XY is placed with the origin coincident with the center of the ring. Other parameters are as shown in the figure.

The finite element model (FEM) with curved beam elements is used to model the ring. A typical element with a local coordinate system r, τ is schematically shown in Figure 6.2a. Each node has three degrees of freedom $u_{r,l}, u_{\tau,l}$ and $u_{\theta,l}$. The second subscript, l, represents the node index. θ_1 and θ_2 are the angular coordinate of the two nodes of the element.

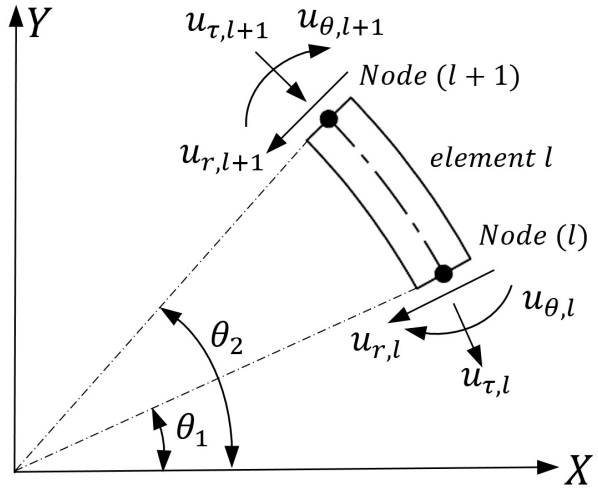

(a) Element displacement

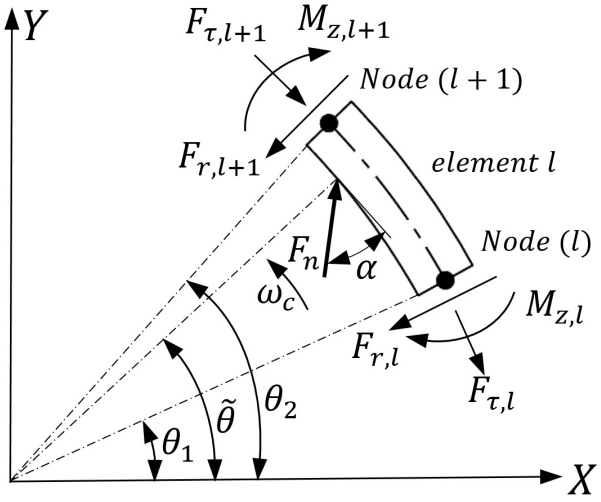

(b) Element forces

Figure 6.2: Curve beam element

6.2.1 Shape function

Different researchers have proposed various shape functions for curved beam elements. In this paper, the one introduced by Wu [7] as below is used:

$$u_r = G_1 + G_2 \cos\tilde{\theta} + G_3 \sin\tilde{\theta} + G_4\tilde{\theta}\sin\tilde{\theta} + G_6\tilde{\theta}\cos\tilde{\theta} \tag{6.1}$$

$$u_\tau = G_1\left(1 + \left(\frac{I}{AR^2}\right)\right)\tilde{\theta} + G_2\sin\tilde{\theta} - G_3\cos\tilde{\theta} + G_4\left(sin\tilde{\theta} - \tilde{\theta}\cos\tilde{\theta}\right) + G_5 + G_6\left(\cos\tilde{\theta} + \tilde{\theta}\sin\tilde{\theta}\right) \tag{6.2}$$

$$u_\theta = G_1\left(1 + \left(\frac{I}{AR^2}\right)\right)R^{-1}\tilde{\theta} + 2G_4R^{-1}\sin\tilde{\theta} + G_5R^{-1} + 2G_6R^{-1}\cos\tilde{\theta} \tag{6.3}$$

where G_1 - G_6 are constants of integration, which are determined by applying the boundary conditions to the Eqs (6.1) to (6.3). $\tilde{\theta}$ is the instant angle of the moving force on the element, and I is the moment of inertia. To write the equations in a more compact matrix form gives:

$$\{u\} = \left[S(\tilde{\theta})\right]\{u_l\} \tag{6.4}$$

where $[S(\tilde{\theta})]$ is shape function matrix defined as below:

$$\left[S(\tilde{\theta})\right] = [P] \times [Q]^T \tag{6.5}$$

where P is obtained from the displacement functions of a curved beam, Q is obtained by applying the boundary conditions of the curved element, and are given as:

$$[Q] = \begin{bmatrix} 1 & \cos\theta_1 & \sin\theta_1 & \theta_1\sin\theta_1 & 0 & \theta_1\cos\theta_1 \\ J\theta_1 & \sin\theta_1 & -\cos\theta_1 & \sin\theta_1 - \theta_1\cos\theta_1 & 1 & \cos\theta_1 + \theta_1\sin\theta_1 \\ J\theta_1 R^{-1} & 0 & 0 & 2R^{-1}\sin\theta_1 & R^{-1} & 2R^{-1}\cos\theta_1 \\ 1 & \cos\theta_2 & \sin\theta_2 & \theta_2\sin\theta_2 & 0 & \theta_2\cos\theta_2 \\ J\theta_2 & \sin\theta_2 & -\cos\theta_2 & \sin\theta_2 - \theta_2\cos\theta_2 & 1 & \cos\theta_2 + \theta_2\sin\theta_2 \\ J\theta_2 R^{-1} & 0 & 0 & 2R^{-1}\sin\theta_2 & R^{-1} & 2R^{-1}\cos\theta_2 \end{bmatrix} \tag{6.6}$$

$$[P] = \begin{bmatrix} 1 & \cos\tilde{\theta} & \sin\tilde{\theta} & \tilde{\theta}\sin\theta & 0 & \tilde{\theta}\cos\tilde{\theta} \\ J\tilde{\theta} & \sin\tilde{\theta} & -\cos\tilde{\theta} & \sin\tilde{\theta} - \tilde{\theta}\cos\tilde{\theta} & 1 & \cos\tilde{\theta} + \tilde{\theta}\sin\tilde{\theta} \\ J\tilde{\theta}R^{-1} & 0 & 0 & 2R^{-1}\sin\tilde{\theta} & R^{-1} & 2R^{-1}cos\tilde{\theta} \end{bmatrix} \tag{6.7}$$

$$J = 1 + \left(\frac{I}{AR^2}\right) \tag{6.8}$$

u and u_l are the displacement vectors at the point of the moving force and the two nodes of the element. They are defined as:

$$\{u\} = \{u_r \quad u_\tau \quad u_\theta\}^T \tag{6.9}$$

$$\{u_l\} = \left\{u_{r,l} \;\; u_{\tau,l} \;\; u_{\theta,l} \;\; u_{r,l+1} \;\; u_{\tau,l+1} \;\; u_{\theta,l+1}\right\}^T \tag{6.10}$$

6.2.2 Transformation of moving loads

The forces on a curved beam element of the ring are displayed in Figure 6.2b. The meshing force, traveling with a constant angular velocity, ω_c, is transformed to nodal forces through the shape function as below:

$$\{F_l(t)\} = \left[a(\tilde{\theta}_n)\right]^T \begin{Bmatrix} F_{n,r}(t) \\ \\ F_{n,\tau}(t) \end{Bmatrix} \tag{6.11}$$

where $F_l(t)$ represents the nodal force array transformed from the moving load. It has the following form.

$$\{F_l(t)\} = \begin{Bmatrix} F_{r,l} & F_{\tau,l} & M_{z,l} & F_{r,l+1} & F_{\tau,l+1} & M_{z,l+1} \end{Bmatrix}^T \tag{6.12}$$

The subscripts l and n are the index of the element number and the moving force number respectively. $F_{n,r}(t)$ and $F_{n,\tau}(t)$ are the radial and tangential components of moving load, respectively, and are defined as:

$$F_{n,r}(t) = -F_n(t)\sin\alpha \tag{6.13}$$

$$F_{n,\tau}(t) = -F_n(t)\cos\alpha \tag{6.14}$$

where α is the pressure angle of the ring gear as shown in Figure 6.2b. $a(\tilde{\theta}_n)$ is a matrix defined as:

$$\left[a(\tilde{\theta}_n)\right] = \begin{bmatrix} S_{11}(\tilde{\theta}_n)\ S_{12}(\tilde{\theta}_n)\ \cdots\ S_{16}(\tilde{\theta}_n) \\ S_{21}(\tilde{\theta}_n)\ S_{22}(\tilde{\theta}_n)\ \cdots\ S_{26}(\tilde{\theta}_n) \end{bmatrix} \tag{6.15}$$

where $S_{i,j}(\tilde{\theta}_n), i = 1, 2, j = 1-6$, is the shape function matrix's component as defined by Eq. (6.5). Clearly, the node forces of an element transformed from the moving loads vary with time because the instant position of the force, $\tilde{\theta}_n$, changes with time. If an element does not have a moving force applied at a time moment, then the transformed node force would be zero.

6.2.3 Representation of moving loads

The multiple moving loads, $F_n(t)$, are equally separated and composed of a periodical component and a random one. If the random component is represented as white noise, then a moving force can be expressed as:

$$F_n(t) = F_d(t + \frac{n-1}{N\omega_c}2\pi) + \bar{b}_n W(t) \qquad n = 1, ..., N \tag{6.16}$$

where $F_d(t)$ is a deterministic moving force, ω_c is the constant angular velocity of the moving load, N is the total number of moving loads, $W(t)$ is white noise, and $\bar{b}$ is white noise intensity. The multiple white noises are assumed independent from each other (uncorrelated). The deterministic meshing forces can be obtained from the results of deterministic vibration analysis, and be approximated as a harmonic form.

$$F_d(t) = F_0 + f_a \sin \omega \; t \tag{6.17}$$

where F_0 is the average of the force, f_a is the amplitude of the moving harmonic load, and ω is the meshing frequency of the planet-ring mesh.

6.2.4 Element and global equations

For a curved beam element, the governing equation of motion can be represented as:

$$[m]\{\ddot{u}_l\} + [k]\{u_l\} = \left\{F_l(t, \tilde{\theta}_n)\right\} \delta \left(\tilde{\theta}_n - (l-1)\frac{2\pi}{L} - \omega_c t\right)$$
$$n = 1, ..., N, \quad l = 1, ..., L \tag{6.18}$$

where m and k are mass and stiffness matrices of the element, and δ is the Dirac delta function which is used to represent the instant position of the moving force. The element mass and stiffness matrices are given below. The detail of derivation is not given for the sake of space saving; interested readers are referred to [7].

$$[k] = \frac{EI}{R^3}[V][Q]^{-1} \tag{6.19}$$

$$[m] = \rho R [Q]^{-1^T} \int_{\theta_1}^{\theta_2} \left([P]^T [\Lambda] [P] \, d\theta\right) [Q]^{-1} \tag{6.20}$$

where ρ is the density of the material. E is the module of elasticity. Λ, and V are given as:

$$[V] = \begin{bmatrix} 0 & 0 & 0 & -2\sin\theta_1 & 0 & -2\cos\theta_1 \\ 0 & 0 & 0 & 2\cos\theta_1 & 1 & -2\sin\theta_1 \\ -R & 0 & 0 & -2R\cos\theta_1 & R^{-1} & 2R\sin\theta_1 \\ 0 & 0 & 0 & 2\sin\theta_2 & 0 & -2\cos\theta_2 \\ 0 & 0 & 0 & -2\cos\theta_2 & 1 & -2\sin\theta_2 \\ R & 0 & 0 & 2R\cos\theta_2 & R^{-1} & -2R\sin\theta_2 \end{bmatrix} \tag{6.21}$$

$$[\Lambda] = diag\,(A \quad A \quad I) \tag{6.22}$$

The global governing equation of motion of the whole ring can be obtained by assembling the element ones and taking consideration of the boundary conditions. After inserting Rayleigh damping, the equation takes the following form.

$$[M]\{\ddot{U}\} + [C]\{\dot{U}\} + [K]\{U\} = \{F(t, \tilde{\theta})\} \tag{6.23}$$

where M, K, and C are the global mass matrix, global stiffness matrix, and global damping matrix. Proportional damping is assumed in this paper so that $C = \lambda_M M + \lambda_K K$. λ_M and λ_K are two constants.

The stiffness matrix K consists of two parts as $[K] = [K_R] + [K_S]$. K_R is assembled

through element equations, and K_S is the part of the boundary conditions.

$$[K_S] = diag\,(k_r\ k_\tau\ k_\theta \cdots 0 \cdots k_r\ k_\tau\ k_\theta \cdots 0) \tag{6.24}$$

$F(t, \tilde{\theta})$ is the global force vector and for a specific time step is given as:

$$F(t_i, \tilde{\theta}) = \{F_{r,1}\ F_{\tau,1}\ M_{z,1}; \cdots;\ F_{r,n}\ F_{\tau,n}\ M_{z,n}\ \cdots; F_{r,L}\ F_{\tau,L}\ M_{z,L}\}^T \tag{6.25}$$

All the entries in the above are zero except for those related to the elements with the moving loads applied at the specific moment. U is the global node displacement vector in the form below:

$$U = \{u_{r,1}\ \ u_{\tau,1}\ \ u_{\theta,1}\ \cdots\ u_{r,n}\ \ u_{\tau,n}\ \ u_{\theta,n} \cdots u_{r,L+1}\ u_{\tau,L+1}\ u_{\theta,L+1}\}^T \tag{6.26}$$

where L is the total number of elements.

6.3 Solution Procedure

Eq. (6.23) is solved by the stochastic Newmark algorithm developed by Bernardan and Fleury [15]. Before applying the scheme, the excitation force is first split into a deterministic component and a random one according to Eqs. (6.16) and (6.17). Then Eq. (6.23) becomes:

$$[M]\{\ddot{U}(t)\} + [C]\{\dot{U}(t)\} + ([K])\{U(t)\} = \{F_d(t, \tilde{\theta})\} + [B]\{W(t)\} \tag{6.27}$$

Eq. (6.27) is first recast into state-space form with $\{Y(t)\} = \{U(t), \dot{U}(t)\}^T$, and the time is discretized into a series of small-time interval Δt. The following recursive equation can be obtained through the Newmark scheme.

$$\{Y\left(t_{i+1}\right)\} = [T_1]\{Y\left(t_i\right)\} + [T_2]\{H\left(t_i\right)\} + [T_3]\{W\left(t_i\right)\} \tag{6.28}$$

where the vectors and the matrices are defined as:

$$\{Y(t_i)\} = \begin{Bmatrix} U\left(t_i\right) \\ \\ \dot{U}\left(t_i\right) \end{Bmatrix} \tag{6.29}$$

$$[T_1] = \begin{bmatrix} C + \frac{\Delta t}{2}K & M \\ \\ M & -M\frac{\Delta t}{2} \end{bmatrix}^{-1} \begin{bmatrix} C - \frac{\Delta t}{2}K & M \\ \\ M & M\frac{\Delta t}{2} \end{bmatrix} \tag{6.30}$$

$$[T_2] = \begin{bmatrix} C + \frac{\Delta t}{2}K & M \\ \\ M & -M\frac{\Delta t}{2} \end{bmatrix}^{-1} \begin{bmatrix} \frac{\Delta t}{2} & \frac{\Delta t}{2} \\ \\ 0 & 0 \end{bmatrix} \tag{6.31}$$

$$[T_3] = \begin{bmatrix} C + \frac{\Delta t}{2}K & M \\ \\ M & -M\frac{\Delta t}{2} \end{bmatrix}^{-1} \begin{bmatrix} \sqrt{\Delta t}B & 0 \\ \\ 0 & B\frac{\Delta t\sqrt{\Delta t}}{\sqrt{12}} \end{bmatrix} \tag{6.32}$$

$$\{H\left(t_i\right)\} = \begin{Bmatrix} F_d\left(t_i\right) \\ \\ F_d\left(t_{i+1}\right) \end{Bmatrix} \tag{6.33}$$

$$\{W(t_i)\} = \begin{Bmatrix} \Omega(t_{i+1}) \\ \\ \Phi(t_{i+1}) \end{Bmatrix} \tag{6.34}$$

where $\Omega(t_i)$ and $\Phi(t_i)$ are independent standard Gaussian random variables. Taking ensemble average of Eq. (6.28) gives the mean response as below.

$$\langle Y(t_{i+1})\rangle = T_1 \langle Y(t_i)\rangle + T_2 \langle H(t_i)\rangle \tag{6.35}$$

$\langle\rangle$ represents the ensemble average operation. Note that the zero mean of white noise has been used in achieving the above. Multiplying Eq. (6.28) with its transpose, and taking average gives the correlation matrix:

$$[R(t_{i+1})] = [T_1][R(t_i)][T_1]^T + [T_2][G_1][T_2]^T + [T_3][G_2][T_3]^T + [T_1][G_3][T_2]^T + [T_2][G_3]^T[T_1]^T \tag{6.36}$$

where

$$[R(t_i)] = \left\langle Y(t_i)\, Y(t_i)^T \right\rangle \tag{6.37}$$

$$[G_1] = \left\langle H(t_i)\, H(t_i)^T \right\rangle \tag{6.38}$$

$$[G_2] = \left\langle W(t_i)\, W(t_i)^T \right\rangle \tag{6.39}$$

$$[G_3] = \left\langle Y(t_i)\, H(t_i)^T \right\rangle \tag{6.40}$$

The entries in G_2 are either zero or unity. Standard deviation can be obtained by:

$$\sigma_j(t) = \sqrt{R_{j,j}(t) - \langle Y_j(t)\rangle^2} \tag{6.41}$$

6.4 Simulation and Result Analysis

With the dynamic model and the solution procedure presented in the above section, simulation is conducted on a ring gear taken from a wind turbine PGT in which three equally spaced planets are included. The parameters of the ring are as follows:

$E = 210\ GPa$, outer radius = 520 mm, $\alpha = 20°$, face width= 230 mm, $\rho = 7800\ kg/m^3$, and root radius = 492.5 mm.

The ring is connected to the housing through 6 bolts. The stiffness in the three directions are $k_r = 1.362\times10^{12}\ N/m$, $k_\tau = 1.362\times10^{12}\ N/m$ and $k_\theta = 3.405\times10^{10}\ N\cdot m/rad$. The ring is divided into 36 curved beam elements with the bolt connections positioned at nodes. The noise level is assumed as $\bar{b} = 10^5$. The load moves at an angular speed $\omega_c = 2.8rad/s$. Meshing frequency is equal to $\omega = 100.8rad/s$. The period equal to the time in which the moving load is traversing the ring gear for one rotation cycle. The average of the deterministic force is equal to $F_0 = 1\times10^6 N$, and f_a is equal to $6.5\times10^5 N$. For verification purpose, simulation is conducted with both the stochastic Newmark and Monte Carlo Simulations.

Figure 6.3 shows the mean and standard deviation of displacement, u_r, of a moving point where F_1 is applied. Clearly, both the mean and the standard deviation experience six cycles in one revolution. This is reasonable because of the six supports of the ring gear. Also, low and high-frequency signals can be observed in the response, especially in Figure 6.3a. The source of high frequencies is the meshing

frequency of the applied moving harmonic forces. The mean and Standard deviation of displacement, u_r, at the mid-node of a segment between two supports is shown in Figure 6.4. It can be seen that the dominant lower frequency is three in one revolution which is different from Figure 6.3. This makes sense because there are three planets in the specific case. Another observation from both figures is that the results from the stochastic Newmark and MCS agree very well.

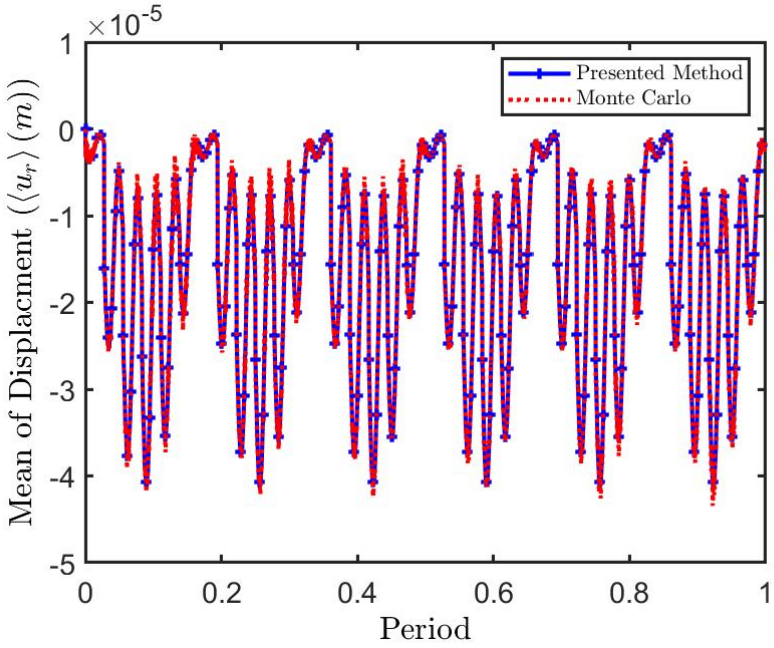

(a) Mean of displacement

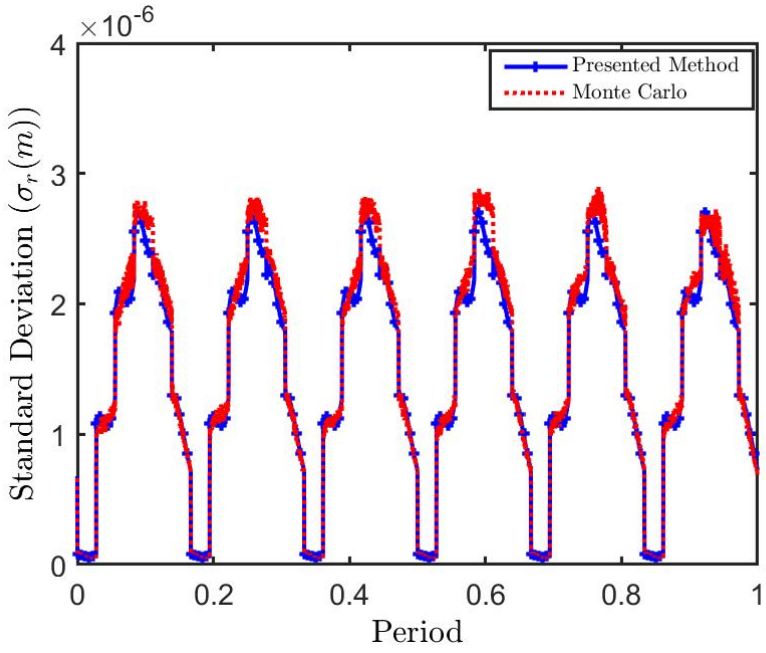

(b) Standard deviation

Figure 6.3: Response of contact point of moving load, F_1 for one rotation cycle of force inside the ring

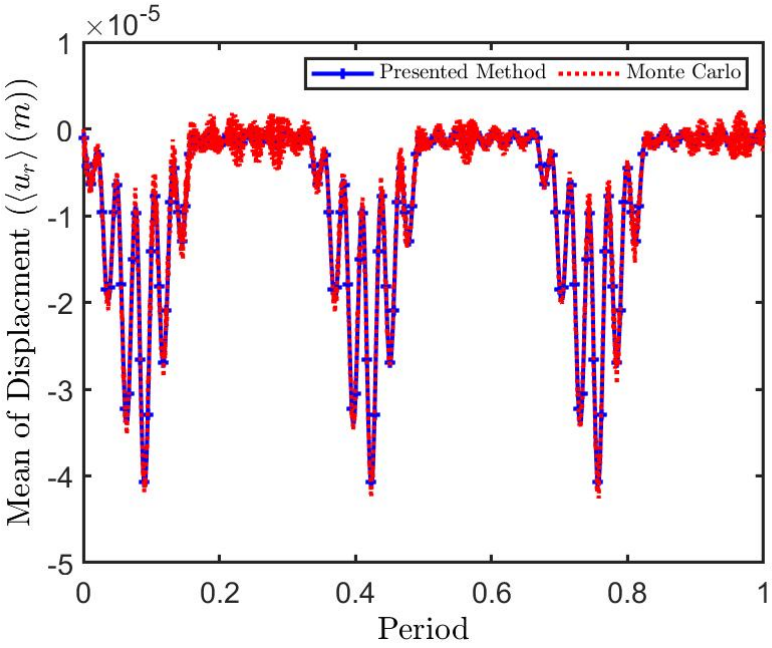

(a) Mean of displacement

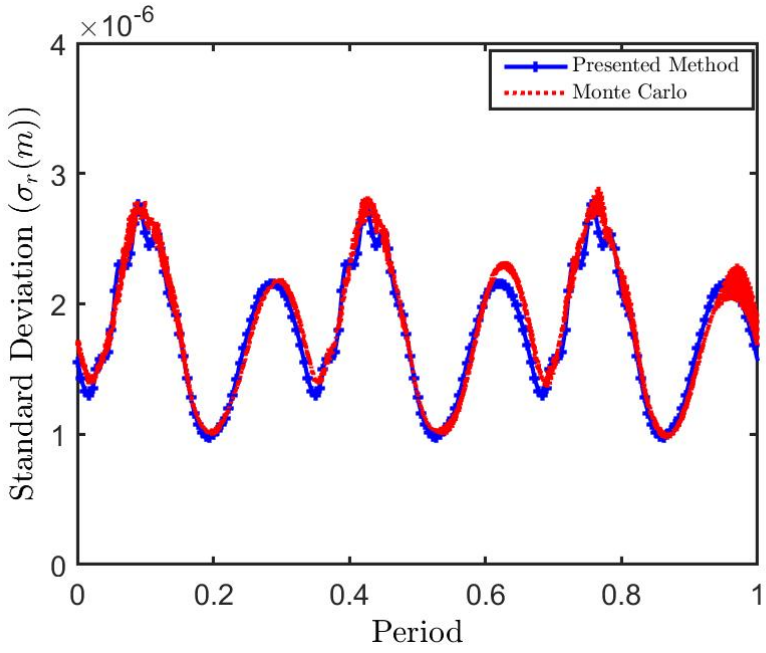

(b) Standard deviation

Figure 6.4: Response of a mid-node

6.4.1 Effect of Speed

In this section, in order to study the effect of the load's speed on dynamic responses of the ring, analysis is done for three angular load velocities, $\omega_{c1} = 22\ rad/s$, $\omega_{c2} = 30\ rad/s$, and $\omega_{c3} = 50\ rad/s$. The computed mean values for various load speeds from Eq. 6.35 is illustrated in Figure 6.5a for the moving point and Figure 6.6a for the mid-node. Figures 6.5b and 6.6b depict the standard deviation of displacement obtained from Eq. 6.41 for the same load speeds for the moving point and the mid-node, respectively. From the figures, we see that alterations of the load velocity change the ring's deflection amount and standard deviation, but this alteration for various load speeds has different trends for the mean and standard deviation. Moreover, from the figure, one can conclude that by increasing the load speed, the relative amount of variation of the mean and standard deviation are different.

Figure 6.6a shows that the maximum amount of mean of displacement increases from 4.76×10^{-5} to 9.59×10^{-5} ,which is a almost two times growth, by increasing the load speed from $\omega_{c1} = 22\ rad/s$ to $\omega_{c2} = 30\ rad/s$. Then it decreases to 4.12×10^{-5} when the load velocity increases from $\omega_{c2} = 30\ rad/s$ to $\omega_{c3} = 50\ rad/s$. This trend happens because when the speed of the deterministic forces approach the critical speed ($31.3 rad/s$), the mean of displacement increases; then when the load moves with a velocity above the critical speed, the mean of displacement decreases.

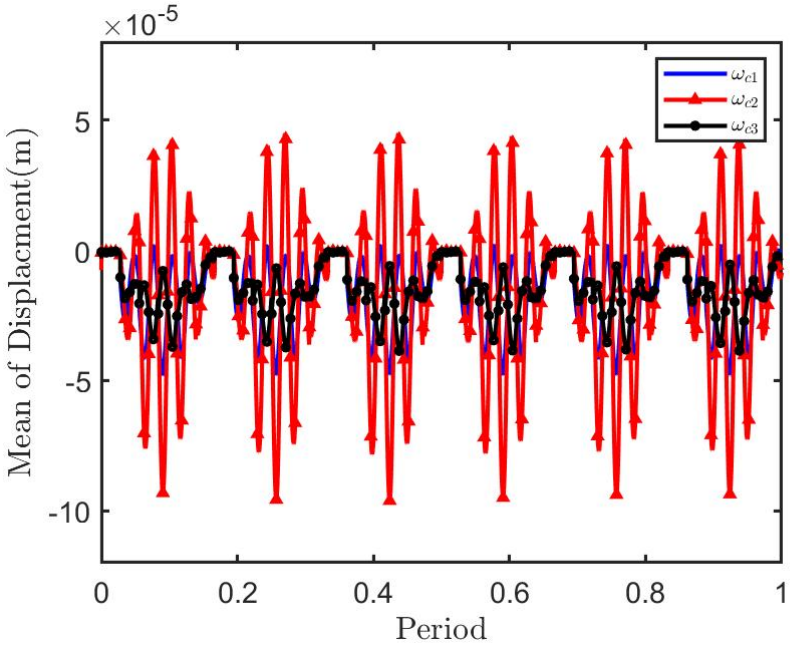

(a) Mean of displacement

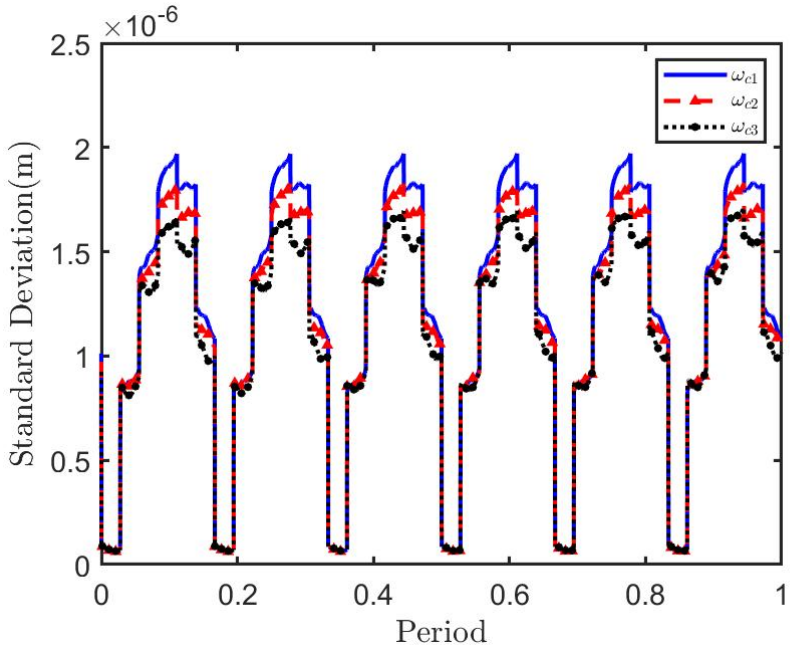

(b) Standard deviation of displacement

Figure 6.5: Response of contact point of moving load, F_1, under various load speeds

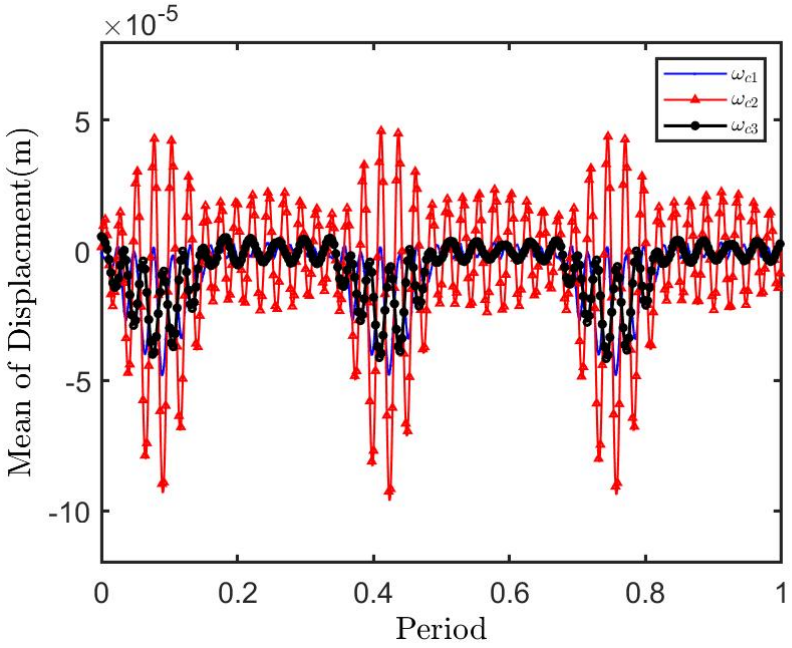

(a) Mean of displacement

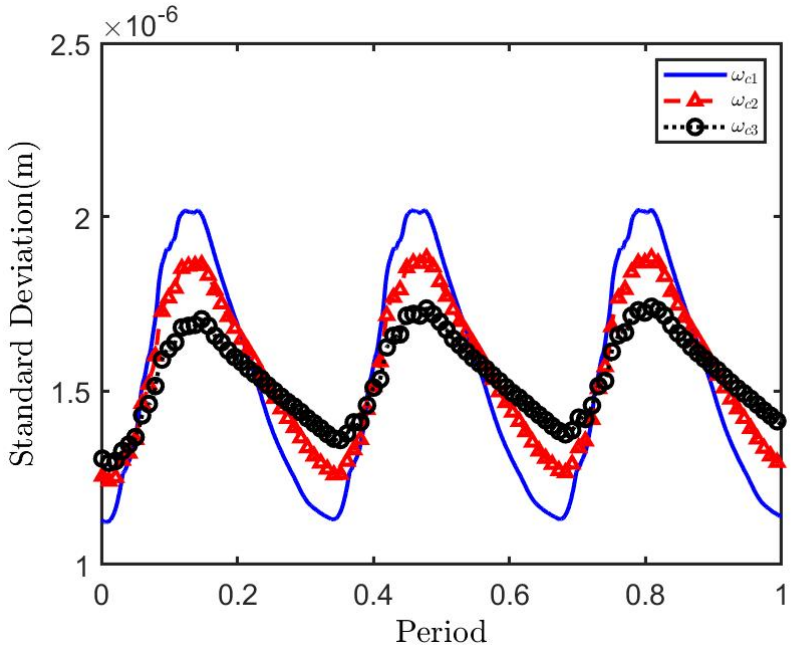

(b) Standard deviation of displacement

Figure 6.6: Response of mid-node under various moving-load speeds

Figure 6.6b shows that the standard deviation of displacement decreases as load speed increases. The maximum standard deviation diminishes from 1.97×10^{-6} to 1.82×10^{-6}, which is 7 percent reduction, when load speed increases from $\omega_{c1} = 22\ rad/s$ to $\omega_{c2} = 30\ rad/s$. Then by increasing load speed to $\omega_{c3} = 50\ rad/s$ standard deviation decreases to 1.66×10^{-6}, which is 9 percent reduction. It can be found that when the white noise force speed increases the random effect of is decrease on ring displacement. The same trend result is shown by Fryba [16] and Yoshimura [17] for beam and Zibdeh [18] for rotating beam under white noise excitation. The standard deviation is independent of the load speed and affects by white noise intensity, damping, and stiffness of the ring which are constant in this section. Therefore, the reason for slightly decreasing of the standard deviation with increasing the speed is how much the load speed increase, the acting time of the load vibration on ring decrease.

In addition, numerical studies have been carried out for moving load with speed 2.8 rad/s to 50 rad/s to study the critical speeds. We take the responses of the mid-node point as an example. The results of the mean and standard deviation for different load angular velocities are illustrated in Figures 6.7. For comparison purposes, results are normalized by the maximum mean and standard deviation of mid-node displacement associated with load speed, $\omega_c = 2.8\ rad/s$. The factors ξ_m and ξ_{sd} represent the normalized mean and standard deviation, respectively. In addition, the critical speed of the ring is obtained from a free vibration analysis of

the ring and the equation $\omega_{cr} = L_c w_0/\pi R$, where L_c is the length of ring, and w_0 is the fundamental natural frequency of the ring. Thus, based on the analysis the critical speed is $\omega_{cr} = 2378.8$. Since we consider the harmonic force excitation in the model, the critical speeds related to the frequency of harmonic excitation (meshing frequency) are observed, as well.

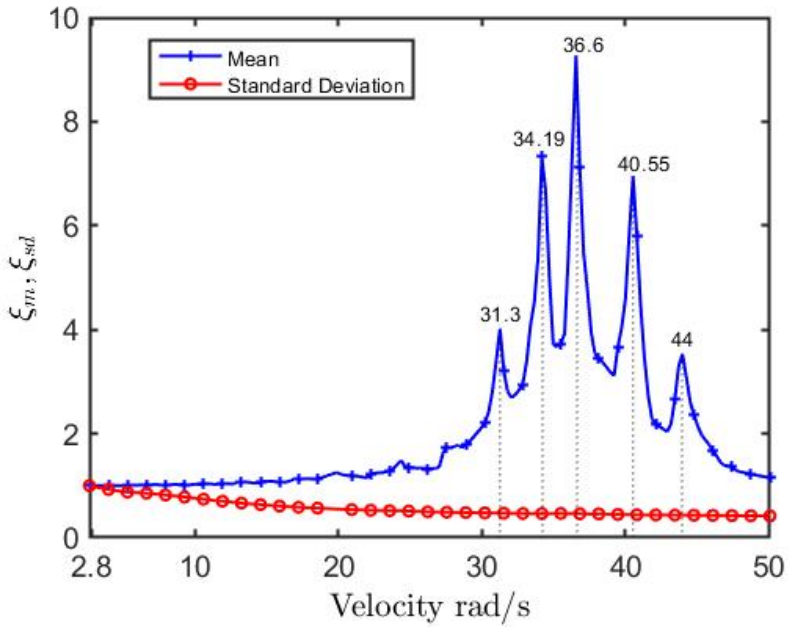

Figure 6.7: Critical Speed

Figure 6.7 shows that the maximum of the mean of the displacement varies non-uniformly by alteration of the load speed. At the low load speed, less than 8, the maximum mean of the displacement does not change significantly. In load speeds, $\omega_c = 31.3,\ 36.6, and\ 44\ rad/s$, the resonance happens, and the mean of the dis-

placement of the mid-node is maximum. These speeds are the critical speeds of the system since they are equal to the ω_{cr}/n, where n is an integer number. In addition, Figure 6.7 shows that at load speeds, $\omega_c = 34.19\ rad/s$ and $\omega_c = 40.55\ rad/s$, the resonance occur. These speeds are considered the critical speed caused by the resonance associated with meshing frequency. Thus, when the moving-load speed approaches the critical speeds, the maximum mean of deflection of a ring increases, and when loads move faster than critical speed, the maximum deflection decrease.

From Figure 6.7, one sees that the maximum Standard deviation of displacement decreases smoothly from low speed to high speed. The reason for the sightly reduction of the standard deviation by increasing the velocity can be that at high speed, there is not enough time for sizeable dynamic displacement. Furthermore, this trend shows the independency of the maximum standard deviation of displacement from the critical speeds.

6.4.2 Effect of white noise intensity

In this section effect of the white noise intensity $(\bar{b}_1, \bar{b}_2, \bar{b}_3)$ on the dynamic response of the ring under moving load is analyzed. The analysis is conducted for a different amount of white noise intensity. Since the mean of displacement is not affected by the variation of the random force, in this section only Standard deviation of displacement is discussed. Figure 6.8 shows the Standard deviation of displacement of the mid-node of the ring under three different white noise intensity for three different

load speed, $\omega_c = 22\ rad/s$, $\omega_c = 30\ rad/s$, and $\omega_c = 50\ rad/s$. It can be seen that by increasing the intensity of the white noise the amount of the standard deviation increases. Figures 6.8a to 6.8c display that different amount of standard deviation is obtained for different load speeds under the same white noise intensity. From these figures, one sees that by increasing the load speed, standard deviation of displacement of mid-node of ring decreases; therefore higher load speed has a lower standard deviation. The reason is that at lower load speeds, the random load has more acting time on ring; therefore its effects become more obvious. It can be concluded that random load effect on dynamic response of the system is under influence of the load speed and white noise intensity.

6.4.3 Effect of supports

In this section, the influence of the types of supports for different load speeds on the dynamics response of the ring has been investigated. For this purpose, three boundary conditions are considered. The bolt supports which used in previous sections are named case 1 and the supports without torsional spring, which represents the pin supports, with same radial and tangential stiffnesses are case 2. The case in which the pin supports assumed with following stiffnesses, $k_r = 5\times10^{10}\ N/m$, $k_\tau = 5\times10^{10}\ N/m$ are named case 3. In this section for brevity, only standard deviation of the mid-node displacement is presented.

Figure 6.9a shows the Standard deviation of displacement for mid-node of the ring

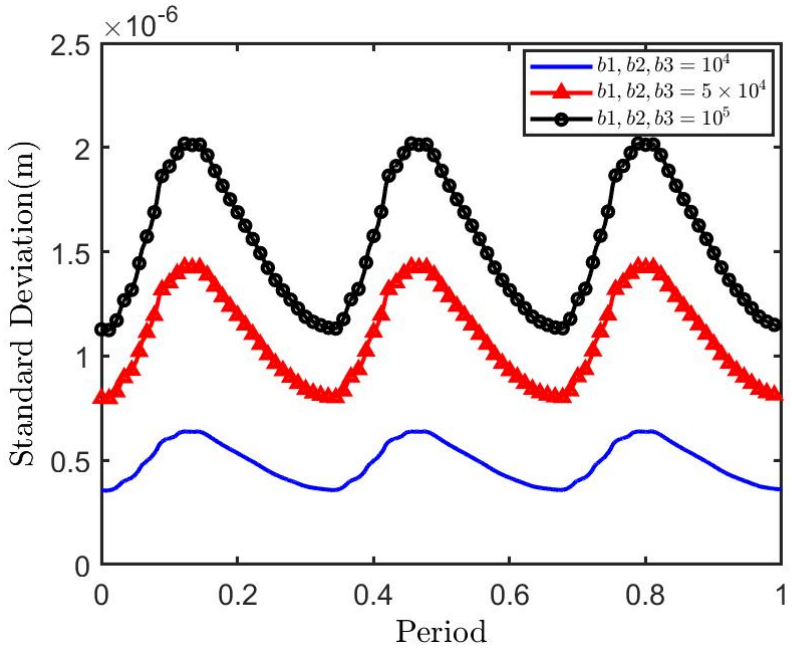

(a) Load speed $\omega_c = 22\ rad/s$

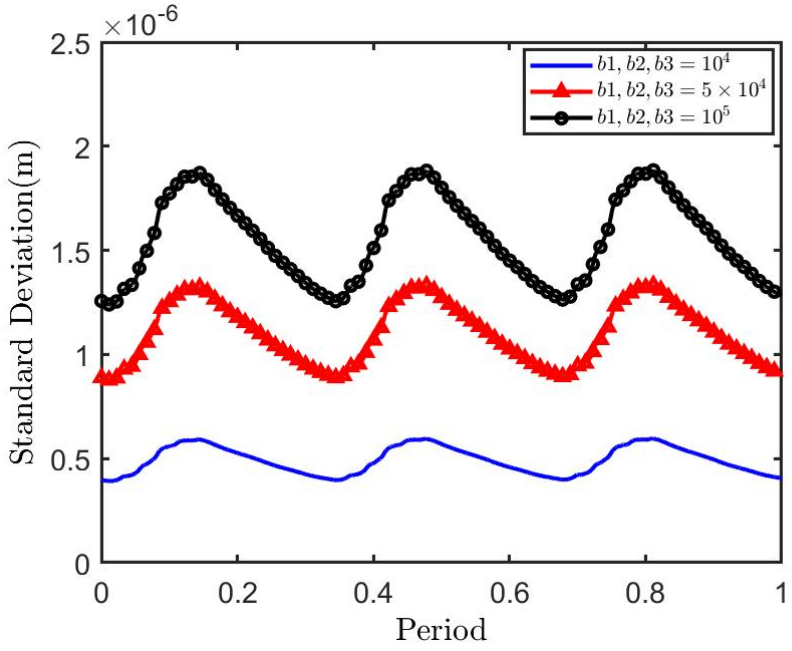

(b) Load speed $\omega_c = 30\ rad/s$

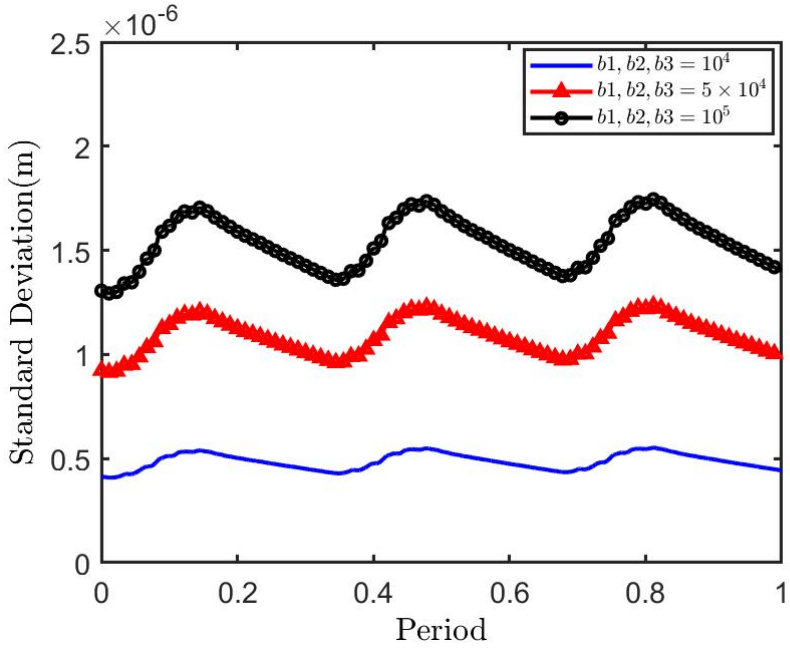

(c) Load speed $\omega_c = 50\ rad/s$

Figure 6.8: Standard deviation of displacement of mid-node under moving-load speeds for various noise level

under load speed $\omega_{c1} = 22\ rad/s$ for three cases. It can be seen that the standard deviation of displacement for cases 1 and 2 are almost the same. That is because the stiffness of radial and tangential directions is high and same, thus the bolt and pin support almost show the same responses. At case 3 amount of the standard deviation increase, on the other hand, the amplitude of standard deviation decrease. This means that when the stiffness of the supports decreases the effect of the moving forces increase.

The same analysis has been conducted to the two other load speeds, $\omega_{c2} = 30\ rad/s$ and $\omega_{c3} = 50\ rad/s$, with different boundary conditions and the results are shown in

Figures 6.9b and 6.9c. The almost same trend is shown in both figures. In addition, at load speed $\omega_{c3} = 50\ rad/s$ case 1 and case 2 give a different response. This shows that at higher speeds pin support has less standard deviation in compare with bolt support with same amount of stiffnesses.

Types of support and the stiffness of the support which presents the tightness of the supports have an impact effect on the dynamic behavior of the ring gear under moving loads.

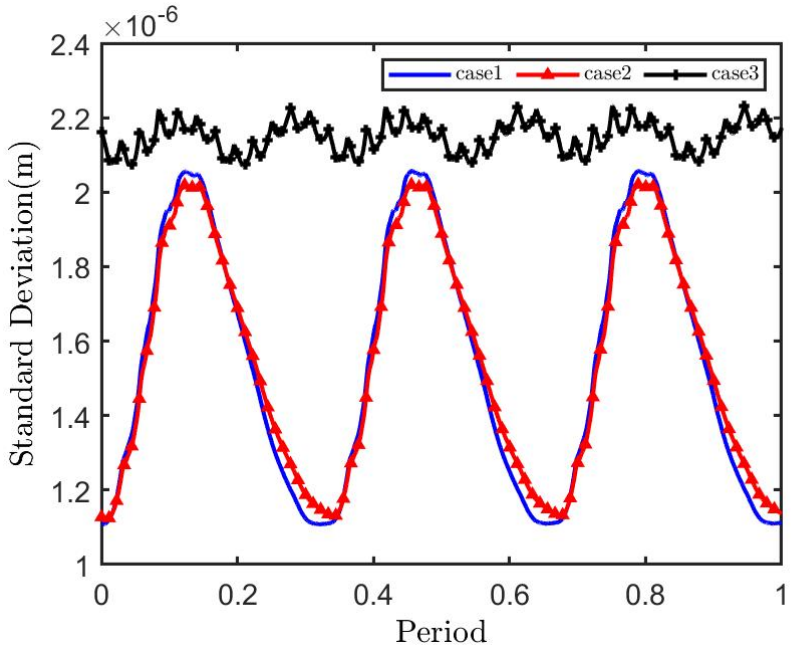

(a) Load speed $\omega_c = 22\ rad/s$

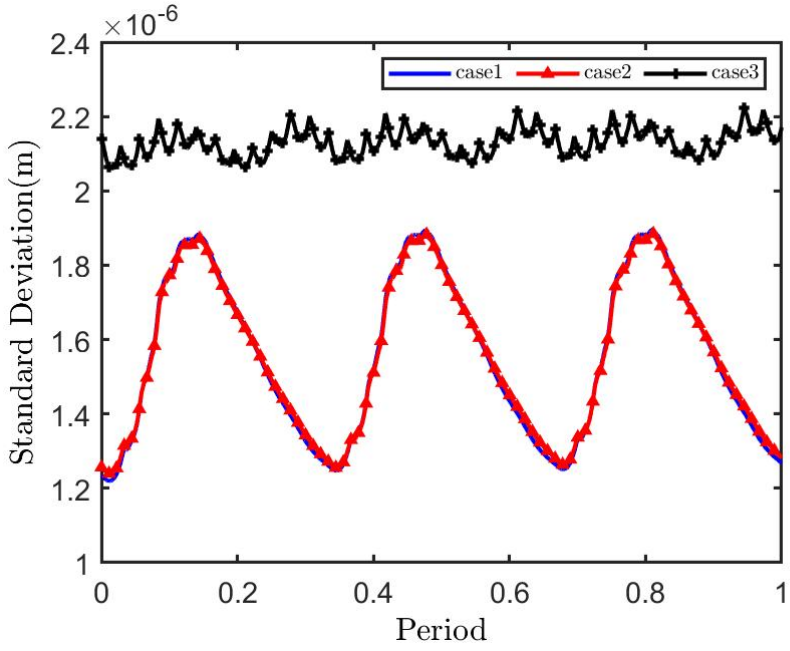

(b) Load speed $\omega_c = 30\ rad/s$

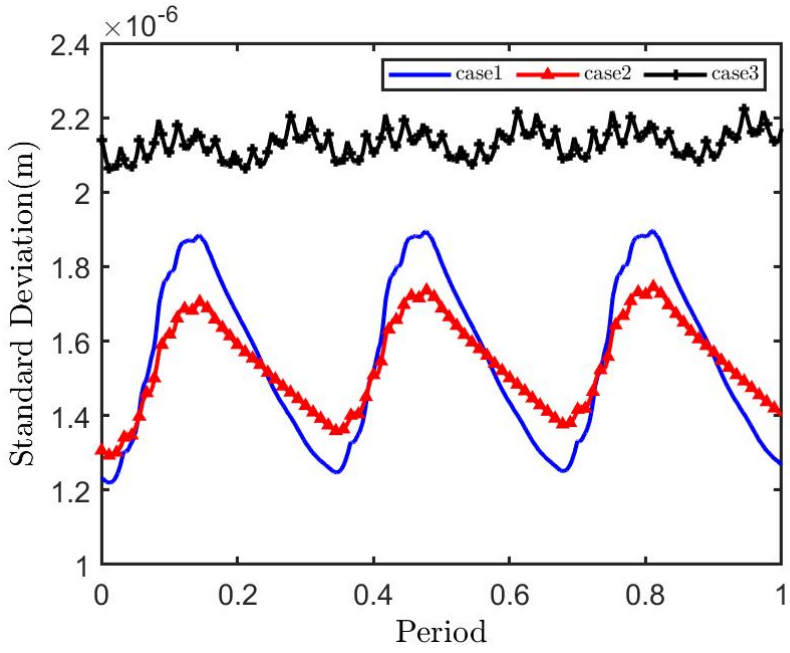

(c) Load speed $\omega_c = 50\ rad/s$

Figure 6.9: Standard deviation of displacement of mid-node under moving-load speeds for various supports

6.5 Conclusions

The object of this research is to analyze the effect of moving random loads on the ring's dynamic responses. The finite element model with a curved beam element is used for modeling the ring. In the model, fixed springs are applied at the boundary condition to represent the supports. The ring is excited by both deterministic and random moving loads, and they transfer to the nodal forces by shape function. We use the stochastic Newmark algorithm to compute the statistics of the results.

For verification of the presented method, Monte Carlo simulations were carried out. The comparison indicates that the results obtained from the presented method match well with the results obtained from the Monte Carlo simulations.

The effect of the load speed on dynamic responses of the ring is analyzed for three load speeds. The results show that by increasing the load speed, initially mean of displacement increases and then decreases. In contrast, the standard deviation of displacement shows a slightly decreasing by increasing the load speed. Thus, the increment of the speed has a lower influence on the standard deviation of displacement in comparison with the mean of displacement.

The critical speed of the moving load has been investigated. It has been shown that there are several critical speed associated with the system and the frequency excitation of harmonic force. A comparison between trends of the means and standard deviations shows that the variation of the standard deviation is much lower than the

mean. The general trend of the mean of displacement is affected by the critical speed. In contrast, the standard deviation of displacement is not influenced by the critical speeds.

The effects of white noise intensity and supports on the dynamic response of the ring under random moving load has been analyzed. The obtained results show that loads speed has significant role in the random load and supports stiffness efficacy on ring dynamic behavior. It can be concluded that at the higher speed pin support gives lower the standard deviation of displacement in comparison with the bolt.

References

[1] Chidamparam P, Leissa AW. Vibrations of planar curved beams, rings, and arches. ASME: Applied Mechanics Reviews. 1993 Sep1;46(9):467–483.

[2] Wu X, Parker RG. Modal properties of planetary gears with an elastic continuum ring gear. Journal of Applied Mechanics. 2008 May 1;75(3).

[3] Tanna RP, Lim TC. Modal frequency deviations in estimating ring gear modes using smooth ring solutions. Journal of sound and vibration. 2004;269(3-5):1099-110.

[4] Wang S, Sun W, Wang Y. Instantaneous mode contamination and parametric combination instability of spinning cyclically symmetric ring structures with ex-

panding application to planetary gear ring. Journal of Sound and Vibration. 2016 Aug 4;375:366-85.

[5] Hu Y, Talbot D, Kahraman A. A Gear Load Distribution Model for a Planetary Gear Set With a Flexible Ring Gear Having External Splines. Journal of Mechanical Design. 2019 May 1;141(5).

[6] Zupan E, Zupan D. Dynamic analysis of geometrically non-linear three-dimensional beams under moving mass. Journal of Sound and Vibration. 2018 Jan 20;413:354-67.

[7] Wu JS, Chiang LK. Dynamic analysis of an arch due to a moving load. Journal of Sound and Vibration. 2004 Jan 22;269(3-5):511-34.

[8] Nikkhoo A, Kananipour H. Numerical solution for dynamic analysis of semicircular curved beams acted upon by moving loads. Proceedings of the Institution of Mechanical Engineers, Part C: Journal of Mechanical Engineering Science. 2014 Sep;228(13):2314-22.

[9] Huang CS, Tseng YP, Hung CL. An accurate solution for the responses of circular curved beams subjected to a moving load. International Journal for Numerical Methods in Engineering. 2000 Aug 30;48(12):1723-40.

[10] Metrikine AV, Tochilin MV. Steady-state vibrations of an elastic ring under a moving load. Journal of Sound and Vibration. 2000 May 4;232(3):511-24.

[11] Forbes GL, Randall RB. Resonance phenomena of an elastic ring under a moving load. Journal of sound and vibration. 2008 Dec 23;318(4-5):991-1004.

[12] Karttunen AT, Von Hertzen R. Steady-state vibration of a viscoelastic cylinder cover subjected to moving loads. European Journal of Mechanics-A/Solids. 2016 Jul 1;58:202-10.

[13] Canchi SV, Parker RG. Parametric instability of a circular ring subjected to moving springs. Journal of Sound and Vibration. 2006 May 30;293(1-2):360-79.

[14] Canchi SV, Parker RG. Parametric instability of a rotating circular ring with moving, time-varying springs. Journal of Vibration and Acoustics. 2006 April; 128(2):231-43.

[15] Bernard P, Fleury G. Stochastic newmark scheme. Probabilistic engineering mechanics. 2002 Jan 1;17(1):45-61.

[16] Frýba L. Non-stationary response of a beam to a moving random force. Journal of sound and vibration. 1976 Jun 8;46(3):323-38.

[17] Yoshimura T, Hino J, Kamata T, Ananthanarayana N. Random vibration of a non-linear beam subjected to a moving load: a finite element method analysis. Journal of Sound and Vibration. 1988 Apr 22;122(2):317-29.

[18] Zibdeh SH, Juma SH. Dynamic response of a rotating beam subjected to a

random moving load. Journal of sound and vibration. 1999 Jun 24;223(5):741-58.

Chapter 7

Conclusion and Future Work

7.1 Conclusion

This dissertation studied planetary gearboxes' dynamic behavior with elastic ring gear under random excitation. The focus of this research was on the planetary gearboxes of horizontal axis wind turbines under the condition of wind turbulence excitation. In addition, a discrete analysis was conducted for ring gear and single gear-pair, to gain a better understanding of the elastic ring gear dynamics under moving load and the efficiency of the different statistical linearization criteria.

7.1.1 Dynamics of Planetary Gear Trains

This thesis is the first research to propose a nonlinear stochastic dynamic model of PGT considering elastic ring gear and backlash nonlinearity. The developed project model included a flexible ring gear, backlash, and time-variant mesh stiffness of the planetary gear. For efficient and accurate modeling, both the lumped-parameter and the finite element method were combined in the proposed model. In addition, the dynamic model included a nonlinear phenomenon, which was a result of the backlash

between gear meshes. This model was used to study planetary gears in wind turbines by considering wind turbulence, backlash, and ring gear elasticity and will improve our understanding of nonlinear random vibration in planetary gears.

Then a statistical linearization method was used and applied to the hybrid nonlinear stochastic model. The results demonstrated that the statistical linearization method could be a suitable method to linearize the nonlinearity of complex geared systems. In addition, the results showed that the ring gear's rim thickness, and the way the ring is connected to the frame, have a significant effect on the dynamic behavior of the gearbox.

7.1.2 Moving load

This thesis studied the random vibration of a thin-walled ring gear of PGT under three equally-spaced moving loads. A finite element method with curved-beam elements was used to model the ring. Three springs were then applied to the boundary of the elements to represent each bolt connection. A parametric study was carried out to examine the effect of moving random loads' speed on the dynamic behavior of the ring. The results showed that by increasing the load speed, the mean of displacement increased and then decreased. In contrast, the standard deviation of displacement showed a slight decrease when the load speed was increased. Thus, the increment of the load speed had a lower influence on the standard deviation of displacement in comparison with the mean of displacement.

The results demonstrated that several critical speeds were associated with the characteristic of the system or the frequency excitation of harmonic force. The obtained results showed, that for the same random load intensity and support connection, increasing load speed gave a lower standard deviation of displacement. This thesis gives a tool to allow computationally efficient, yet accurate, prediction of the effect of moving load speed on vibration displacement.

7.1.3 Gear pairs

A new criterion of the statistic linearization method was used to study the nonlinear behavior of a single gear pair. In this thesis, the backlash is not the sole source of nonlinearity, and time-varying mesh stiffness is the source of the nonlinearity. Energy-based statistic linearization methods, which minimize the error in potential energy between the original and equivalent linear systems, gave an equivalent linear equation for the nonlinear equation. Parametric studies were then conducted and the effect of the input torque level on the dynamic response of the gear pair was analyzed. Monte Carlo simulations were carried out to verify the accuracy of the method.

The results showed that in high input torque, the obtained results were close to the original systems. This proves that the gear system worked in the linear conditions under heavy load conditions. In addition, in lower input torque, some errors between the obtained results from the SL method and MCS were observed. The reason for the errors is, in the lower torque condition, the system works in a backlash, which

caused the system to become nonlinear, and linearization methods fail to estimate representations of the original system. Thus, we can conclude that the statistical linearization method is accurate and is a valid method to solve stochastic nonlinear equations under heavy load conditions.

7.2 Future Work

This dissertation, prioritized many important factors of PGTs in wind turbines. Some factors were ignored that might potentially have a significant effect on PGT response, and these are listed in this section. Also, there are different techniques and solution methods to treat the nonlinearity that might also be suitable for complex geared systems. Thus, the following suggestions are presented for future work:

- In this thesis the backlash and the time-varying meshing stiffness between gear pairs in the planetary gear transmission were considered as a system nonlinearity. In future work, other types of nonlinearity, such as bearing clearance, might be of interest. The carrier's mean bearing and the high-speed shaft's bearings clearance are one of the main concerns of the PGT design. In addition, tooth crack affects the mesh stiffness and would have a direct influence on geared systems dynamic behavior.

- In the case of randomness, there are different sources of randomness in a geared system, and this study only considered one source. For example, since man-

ufacturing errors always exist in gear production, the backlash can become a random variable. In addition, if offshore wind turbines are studied, the ocean waves might be considered as random force instead of the wind turbulence.

- In this thesis, force-based and potential energy-based linearization methods are used. For future work, the energy-based linearization method only applied to single gear mesh in this thesis, and it can be applied to PGT research. Results obtained from an energy-based linearization method can be compared with the results obtained from force-based linearization method to discover which method is more suited for complex gear systems.

- The elastic ring gear properties have a significant effect on the overall dynamics of planetary gear transmissions. In this thesis, the ring gear is modeled as a smooth ring. For future work, to increase the accuracy of the PGT simulation, the ring can be modeled as a smooth ring, and lumped-masses can represent each tooth. A ring gear under a moving loads with an attached mass could then be analyzed.

Appendix

This appendix includes the obtained results from the linearized model and Monte Carlo Simulations for PGT. In section 3.7.1 only the selected responses of PGT components were presented; All the mean and variance of displacement responses of the ring gear, planet gear, sun gear, and carrier are shown in this appendix.

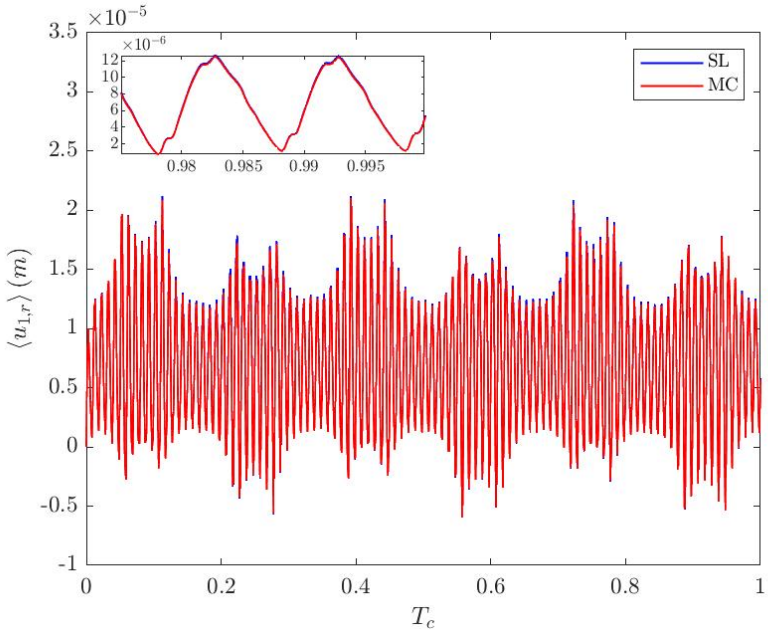

(a) Mean of displacement

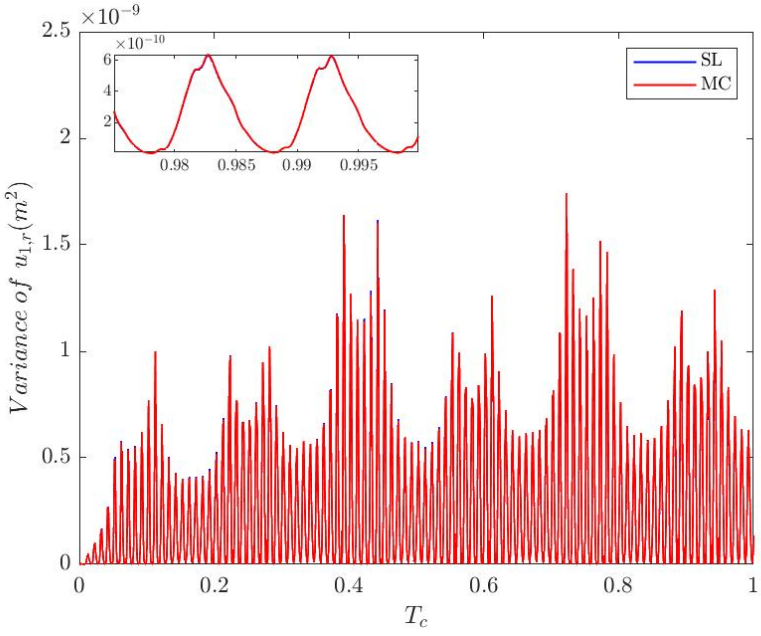

(b) Variance of displacement

Figure A.1: Displacement of Node (1) in the radial direction

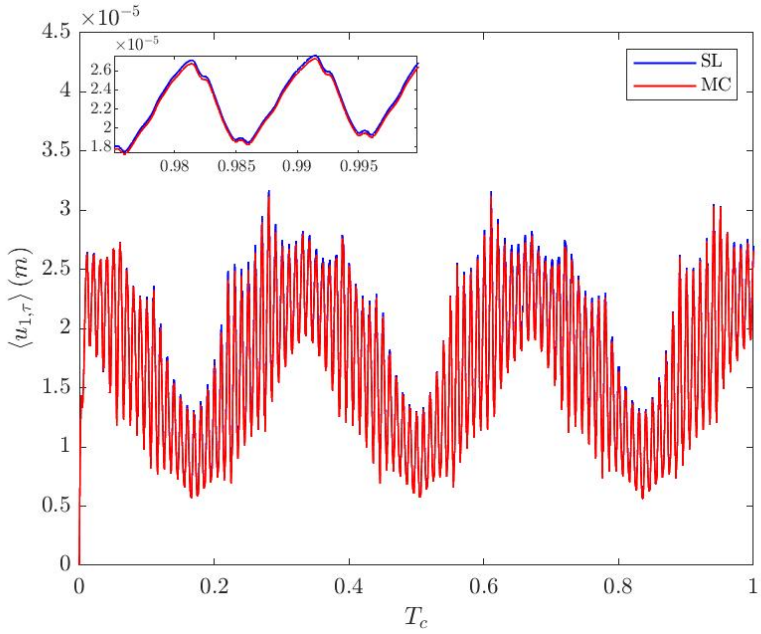

(a) Mean of displacement

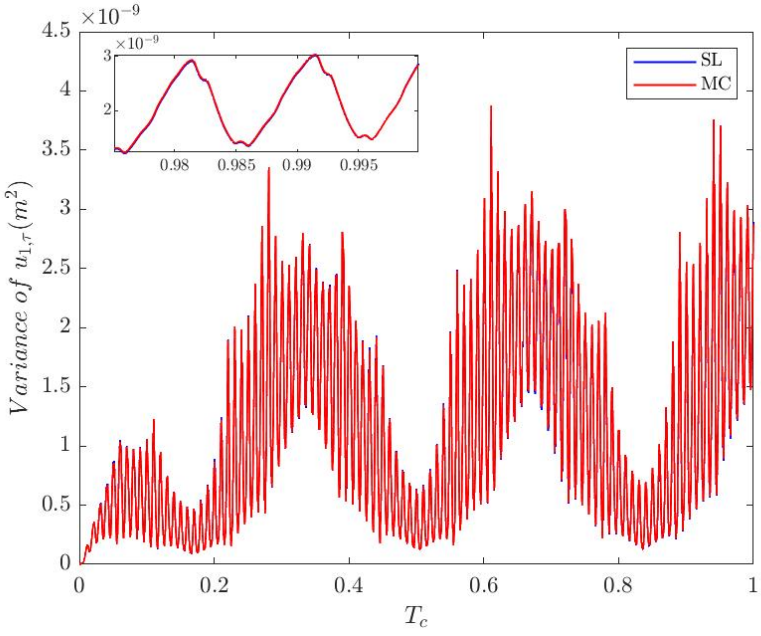

(b) Variance of displacement

Figure A.2: Displacement of Node (1) in the tangential direction

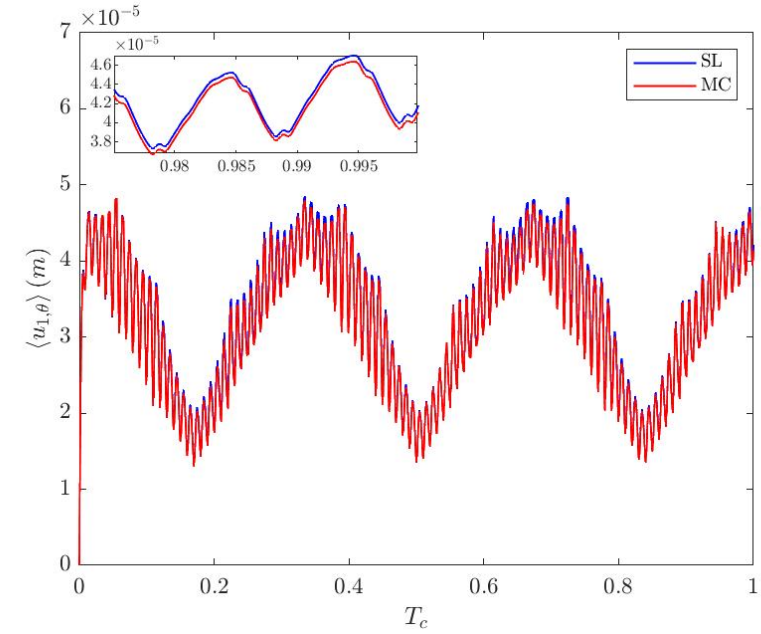

(a) Mean of displacement

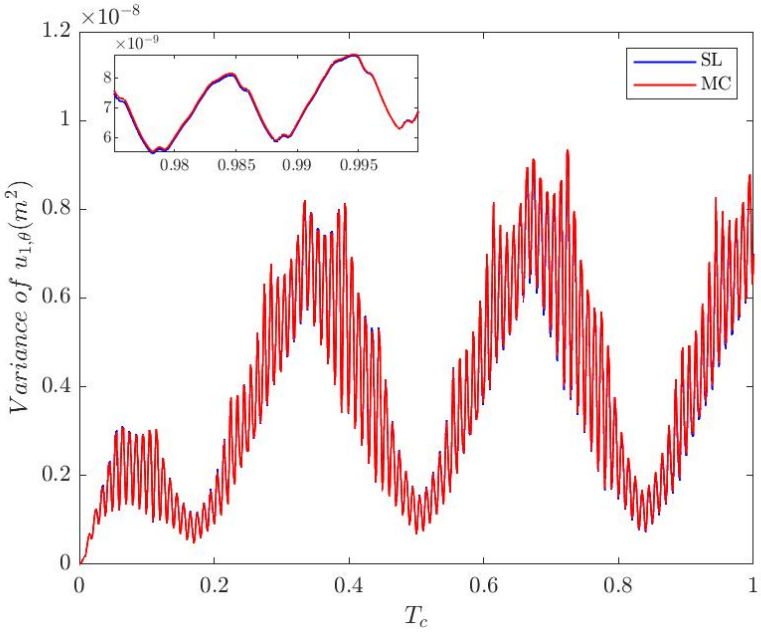

(b) Variance of displacement

Figure A.3: Displacement of Node (1) in the rotational direction

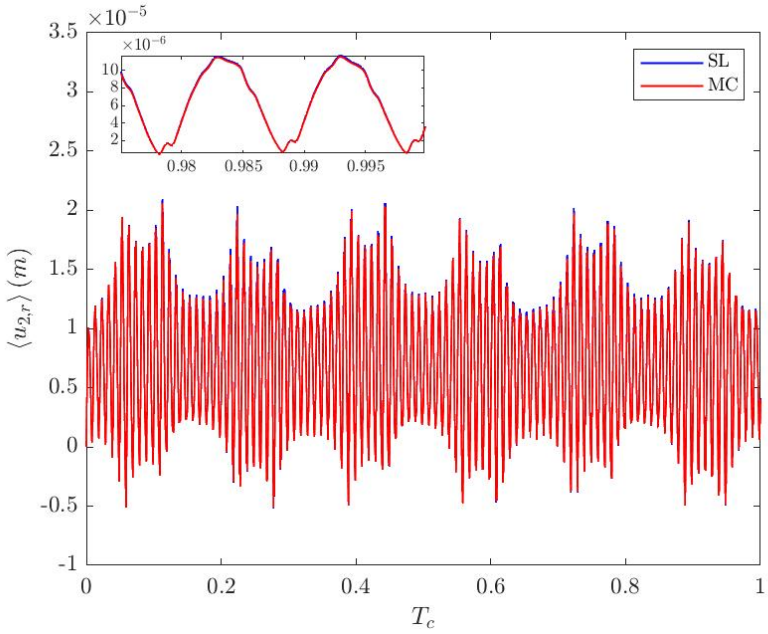

(a) Mean of displacement

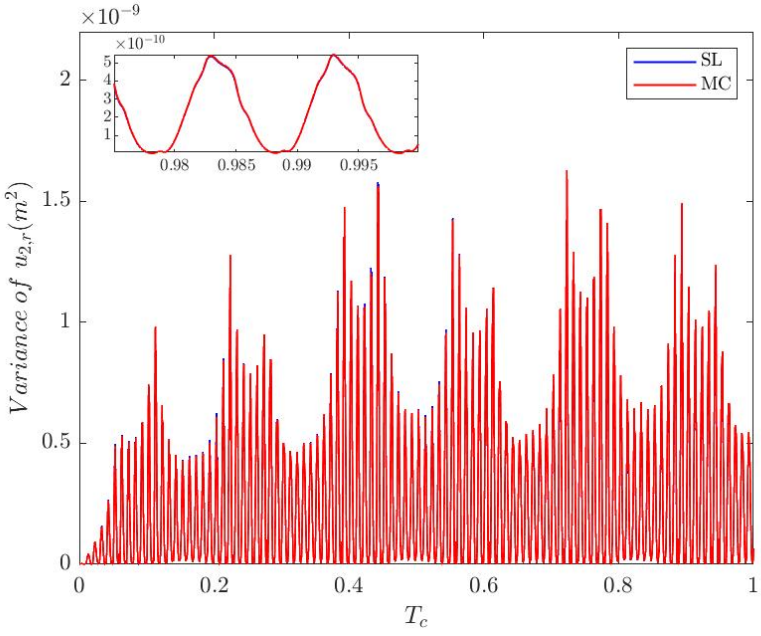

(b) Variance of displacement

Figure A.4: Displacement of Node (2) in the radial direction

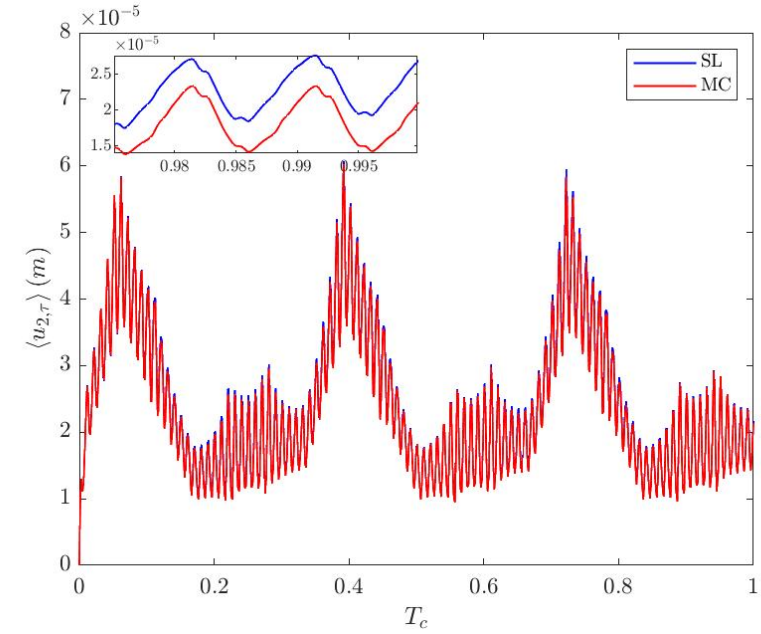

(a) Mean of displacement

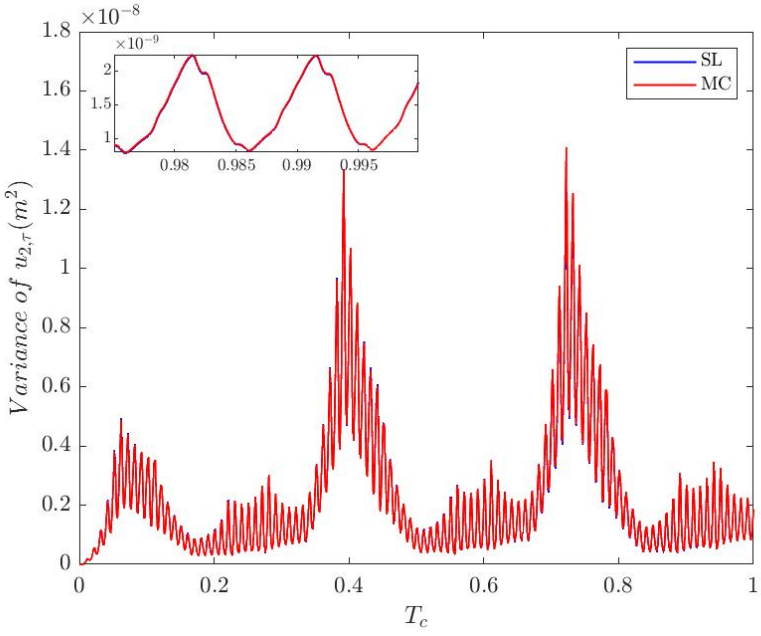

(b) Variance of displacement

Figure A.5: Displacement of Node (2) in the tangential direction

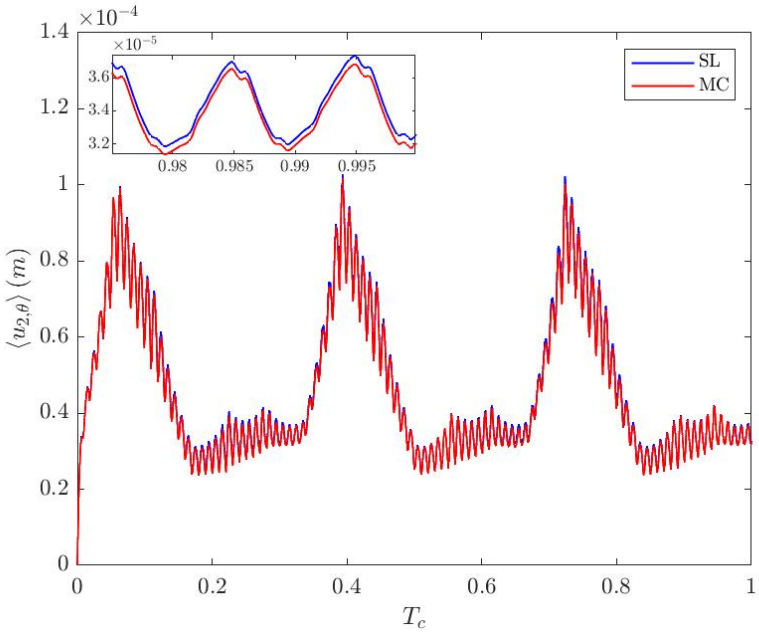

(a) Mean of displacement

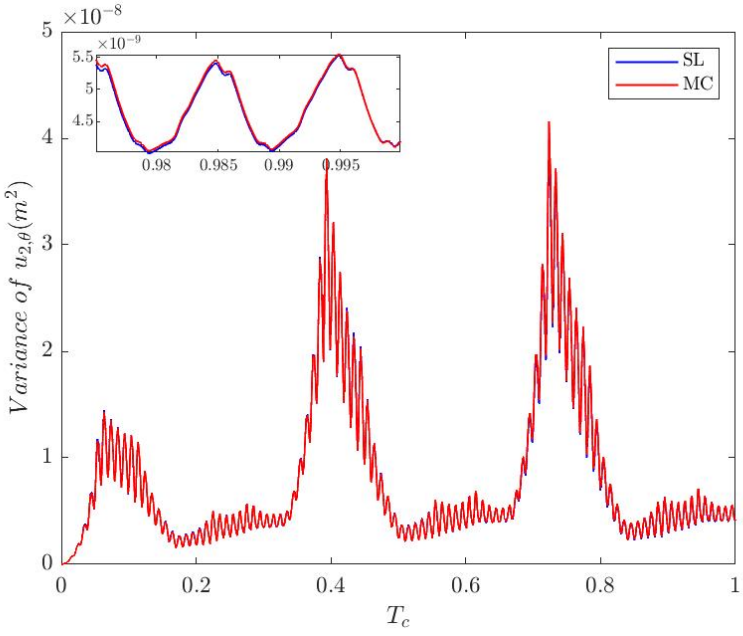

(b) Variance of displacement

Figure A.6: Displacement of Node (2) in the rotational direction

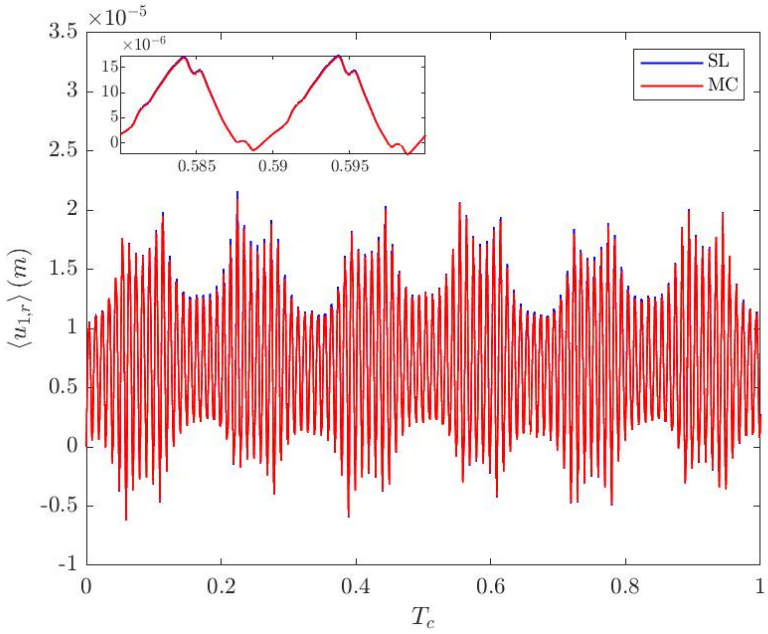

(a) Mean of displacement

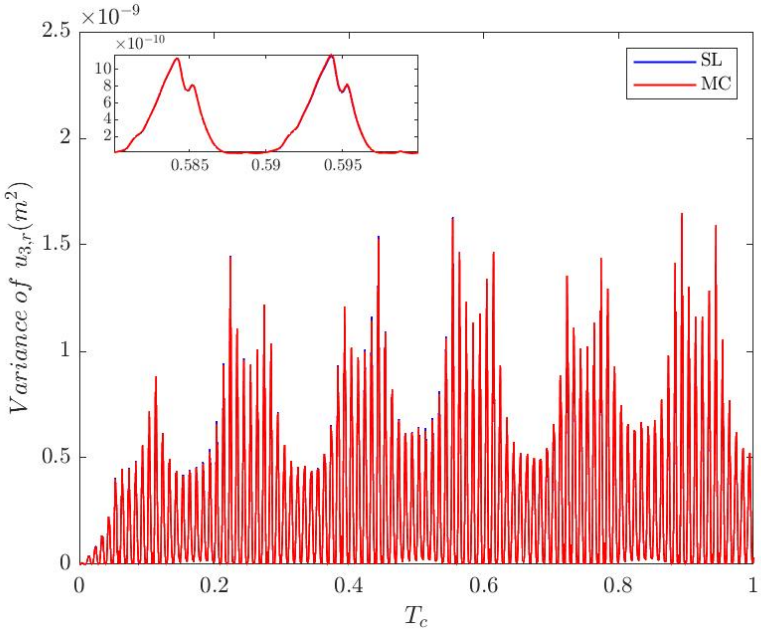

(b) Variance of displacement

Figure A.7: Displacement of Node (3) in the radial direction

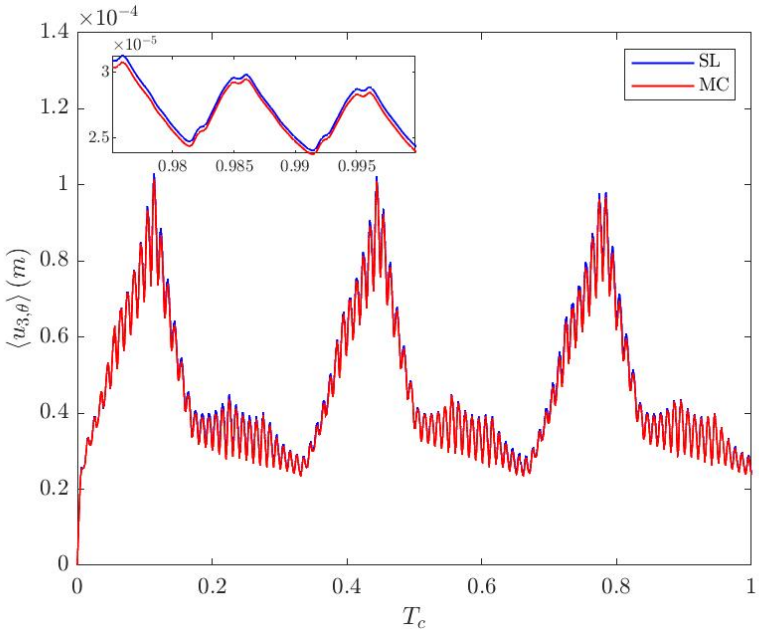

(a) Mean of displacement

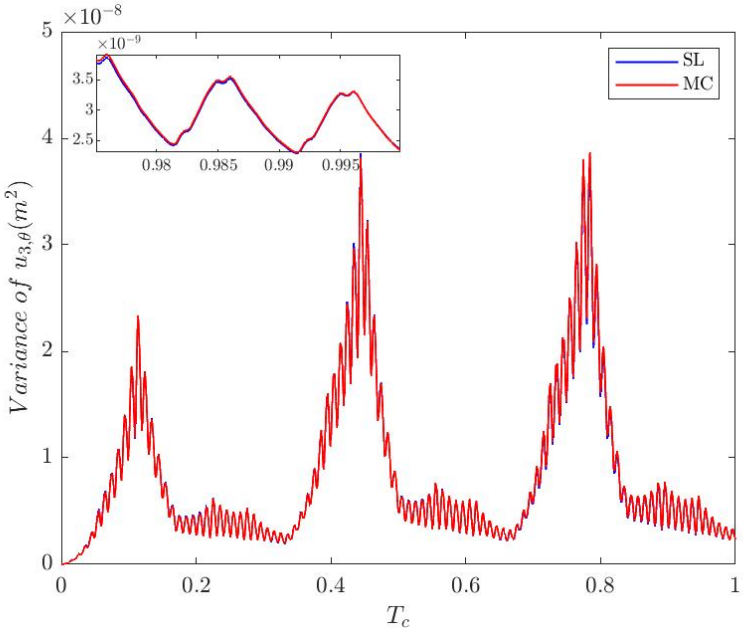

(b) Variance of displacement

Figure A.9: Displacement of Node (3) in the rotational direction

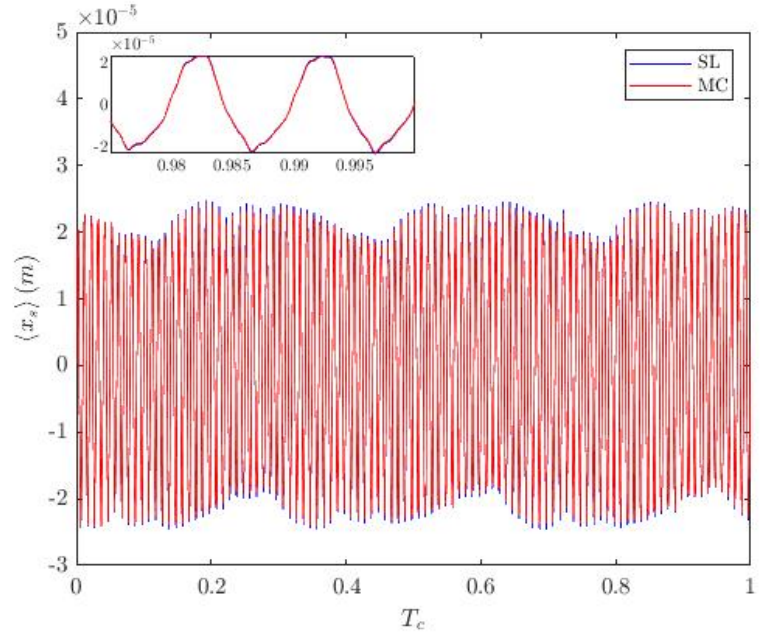

(a) Mean of displacement

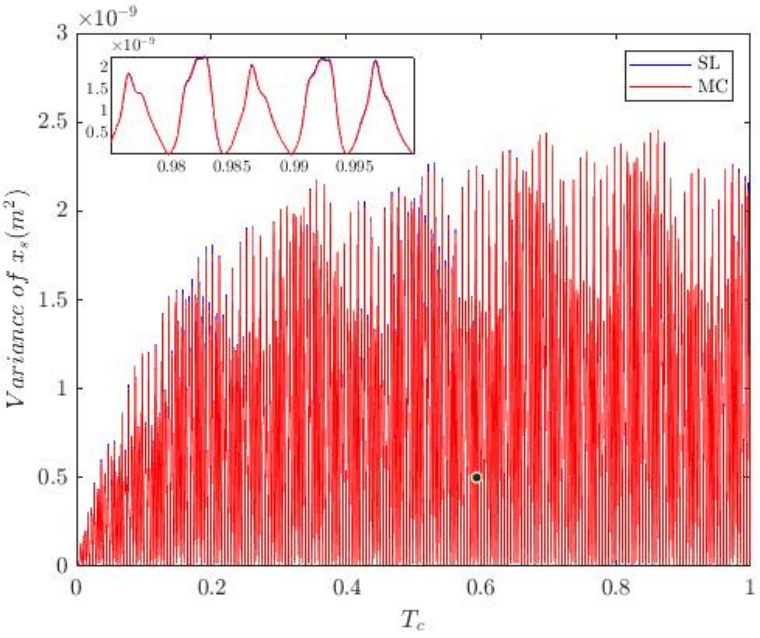

(b) Variance of displacement

Figure A.10: Displacement of sun gear at x direction

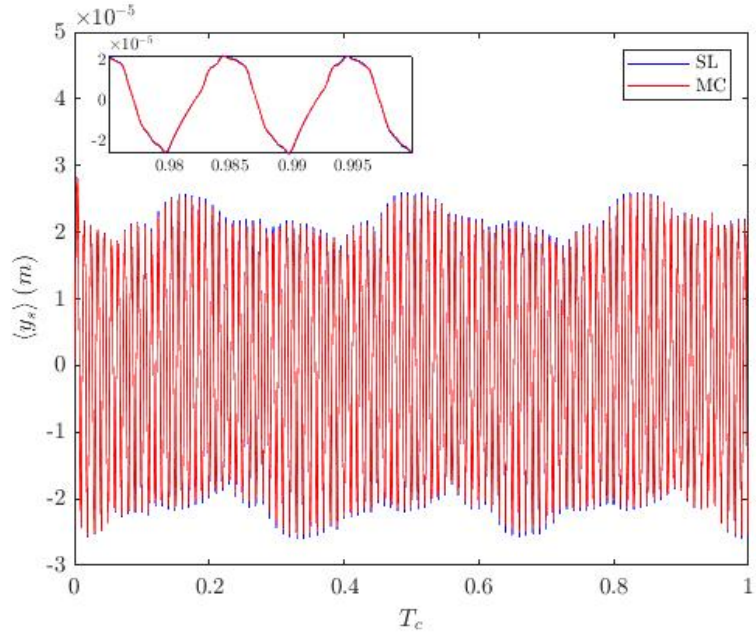

(a) Mean of displacement

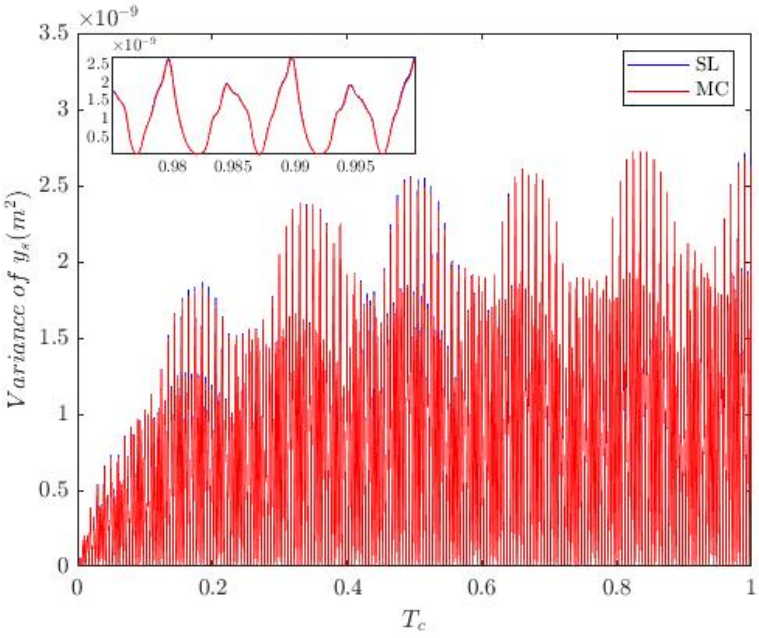

(b) Variance of displacement

Figure A.11: Displacement of sun gear at y direction

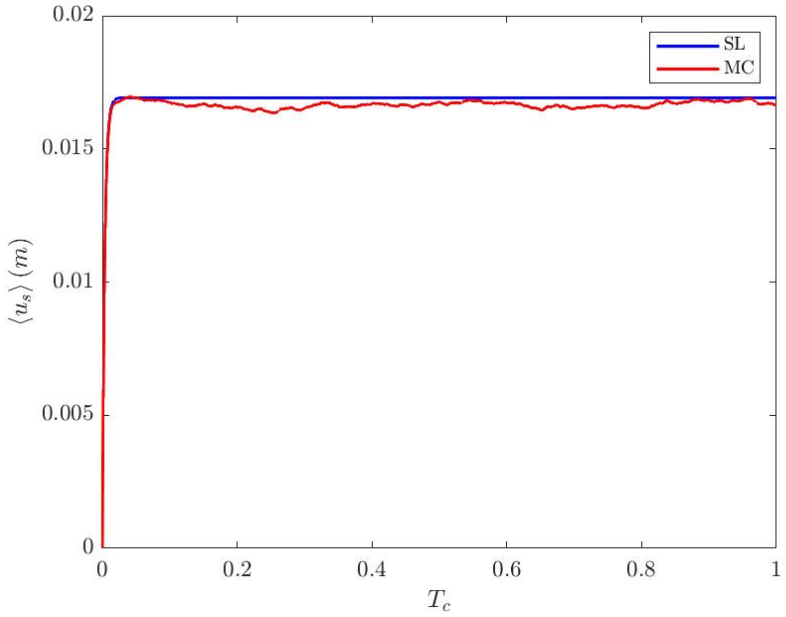

(a) Mean of displacement

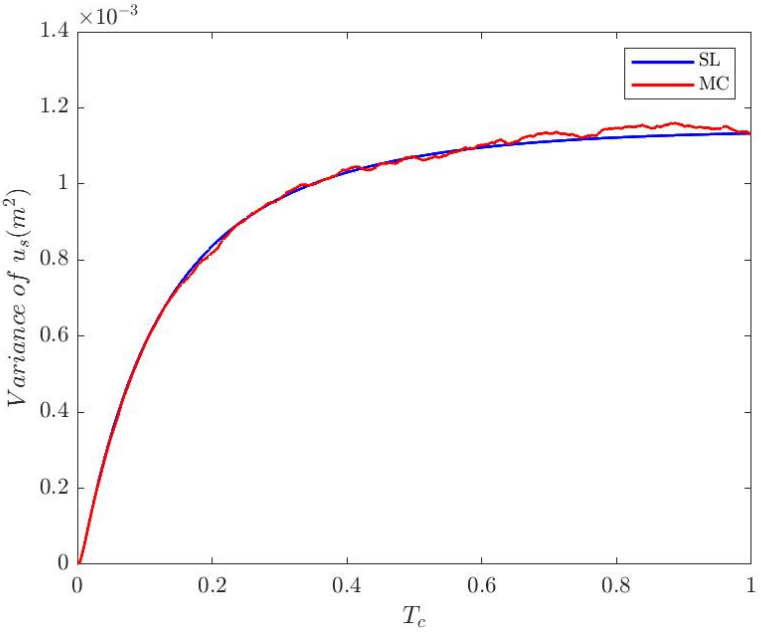

(b) Variance of displacement

Figure A.12: Displacement of sun gear at θ direction

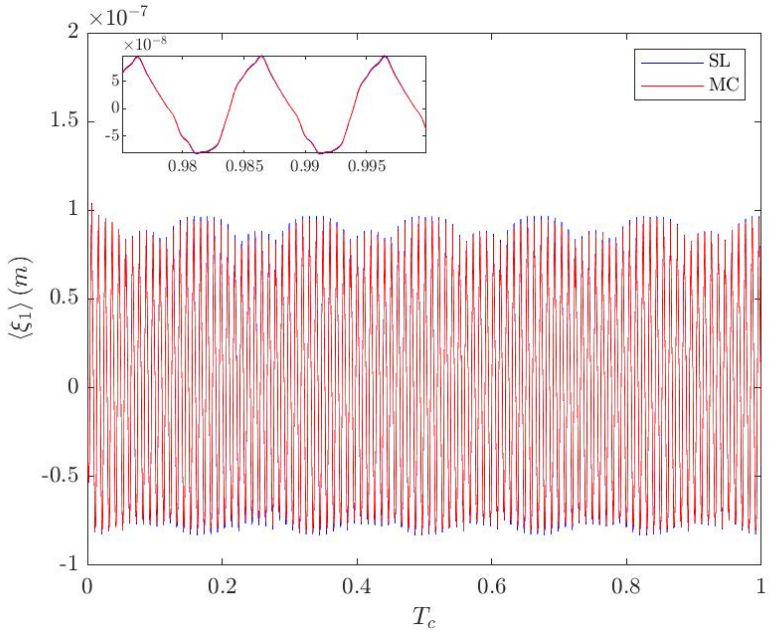

(a) Mean of displacement

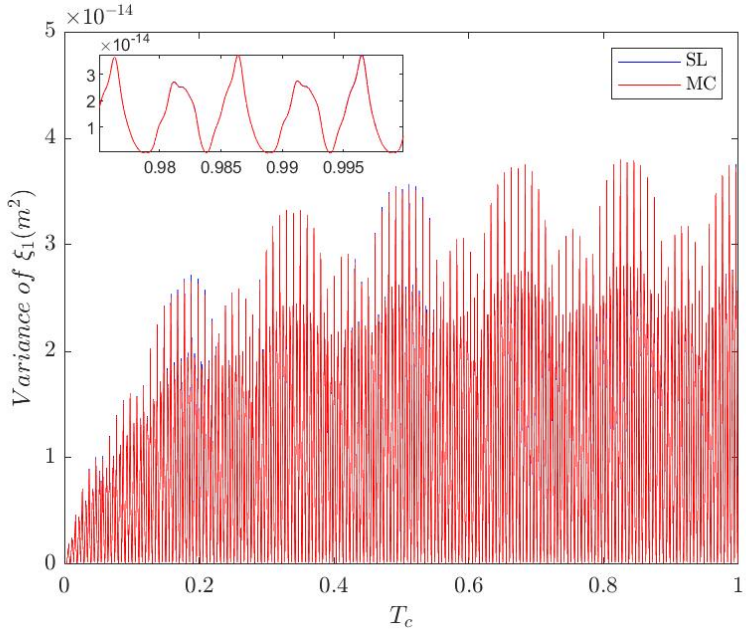

(b) Variance of displacement

Figure A.13: Displacement of planet gear at ξ direction

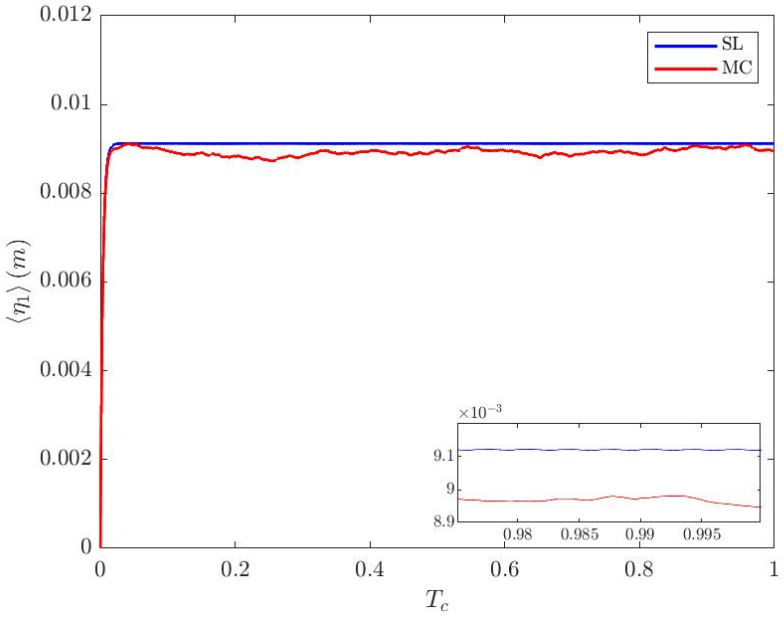

(a) Mean of displacement

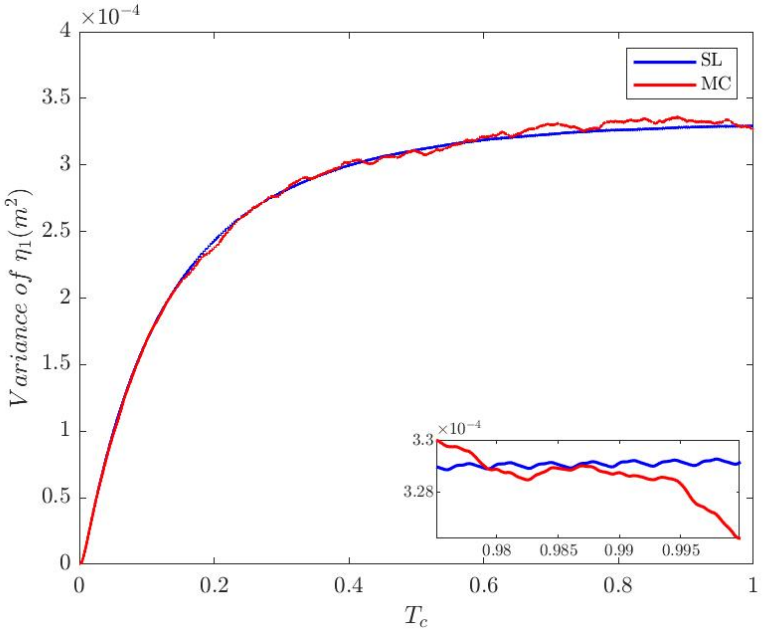

(b) Variance of displacement

Figure A.14: Displacement of planet gear at η direction

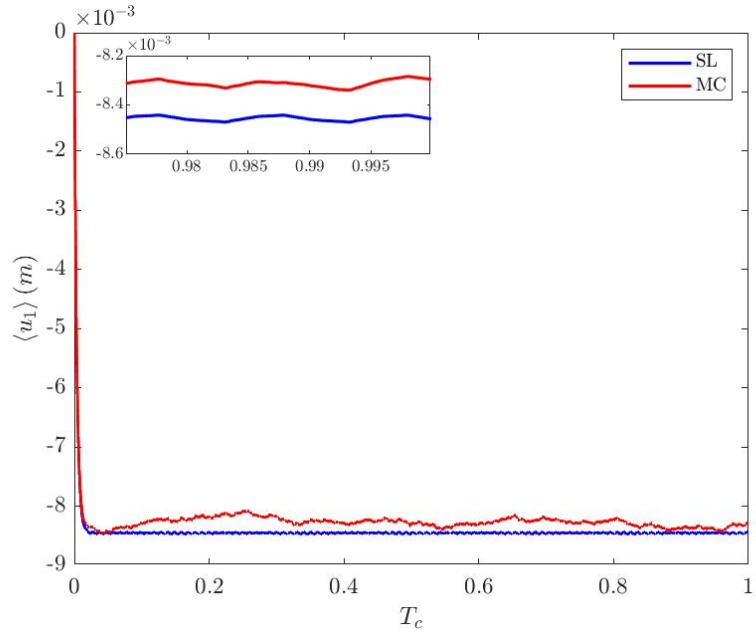

(a) Mean of displacement

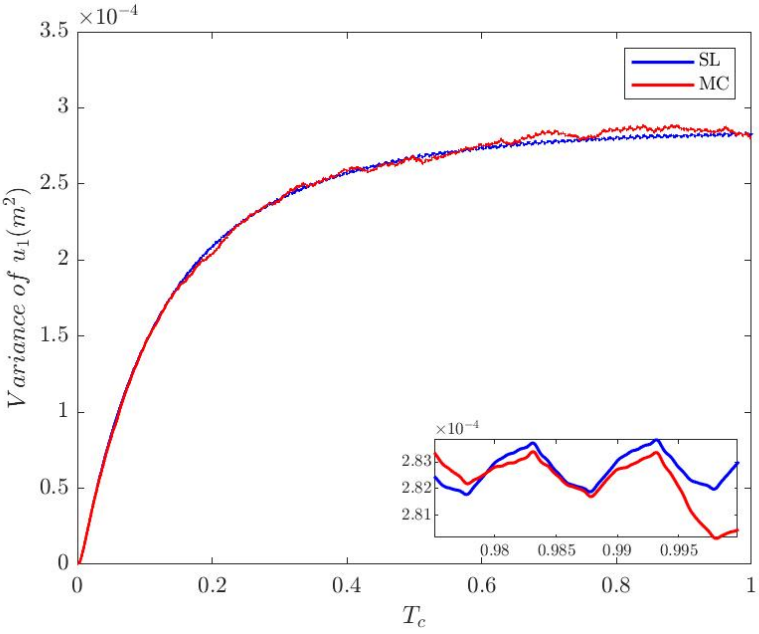

(b) Variance of displacement

Figure A.15: Displacement of planet gear at θ direction

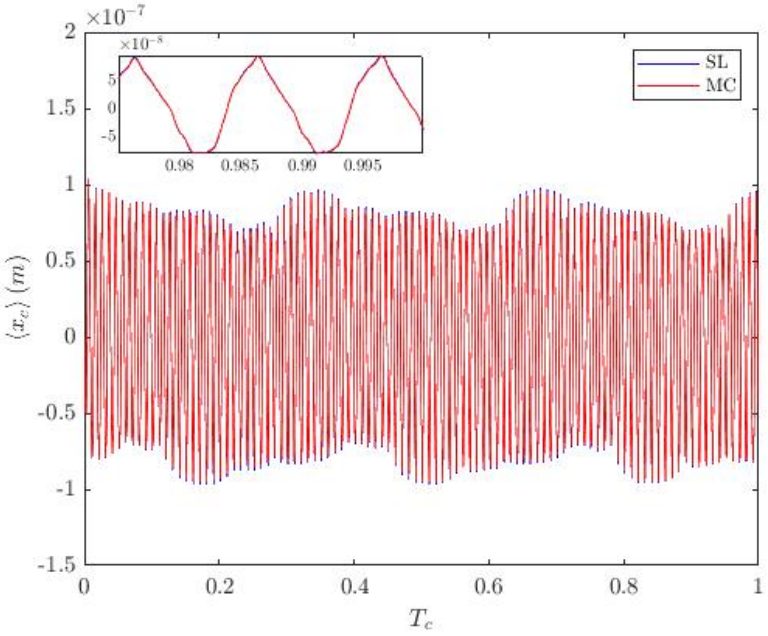

(a) Mean of displacement

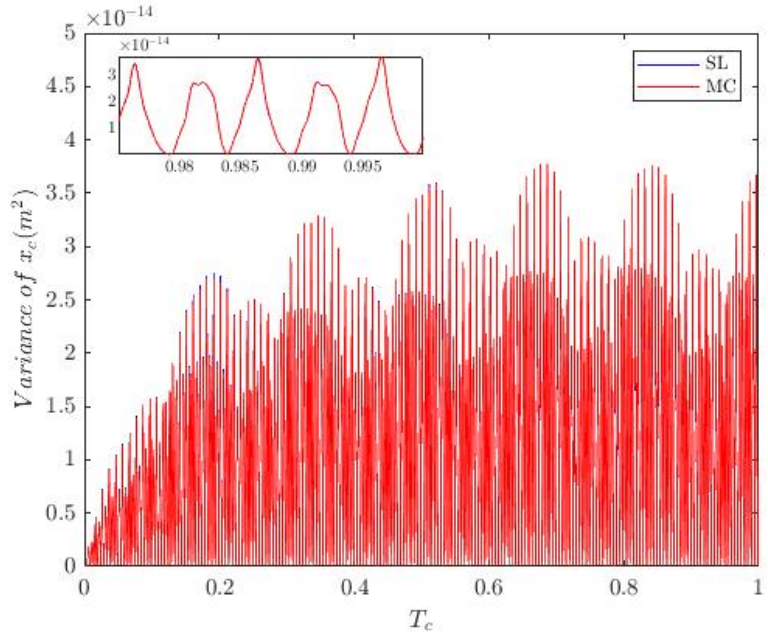

(b) Variance of displacement

Figure A.16: Displacement of carrier at x direction

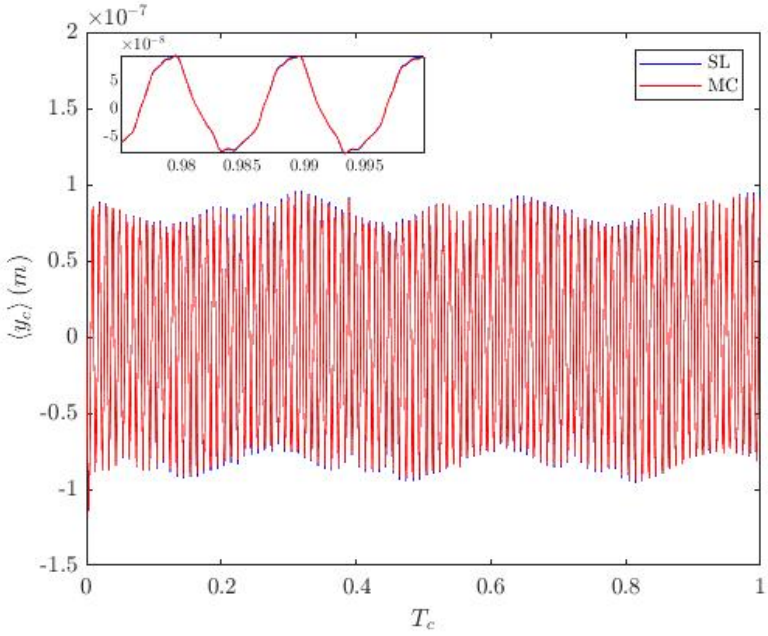

(a) Mean of displacement

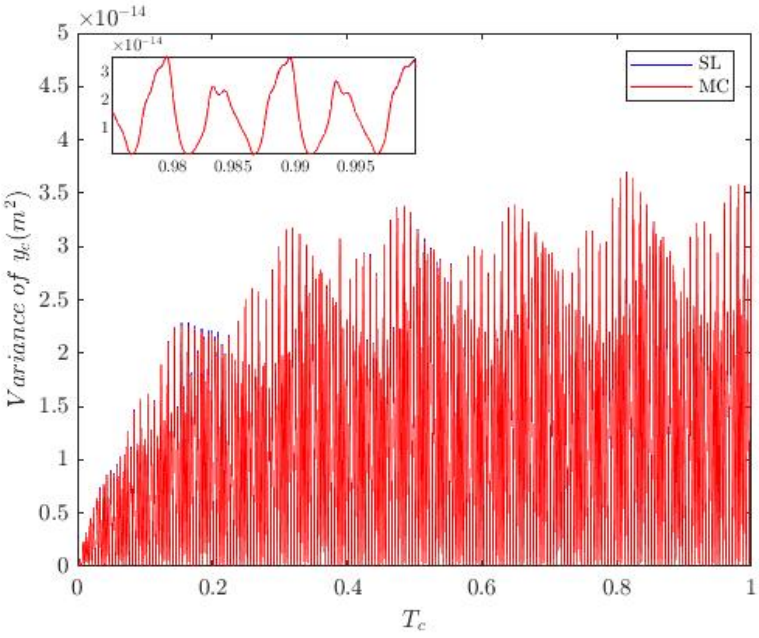

(b) Variance of displacement

Figure A.17: Displacement of carrier at y direction

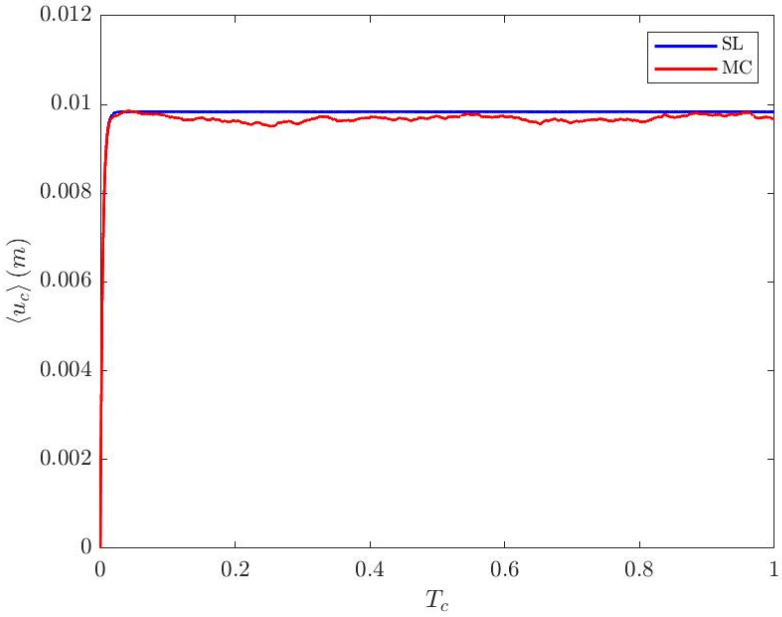

(a) Mean of displacement

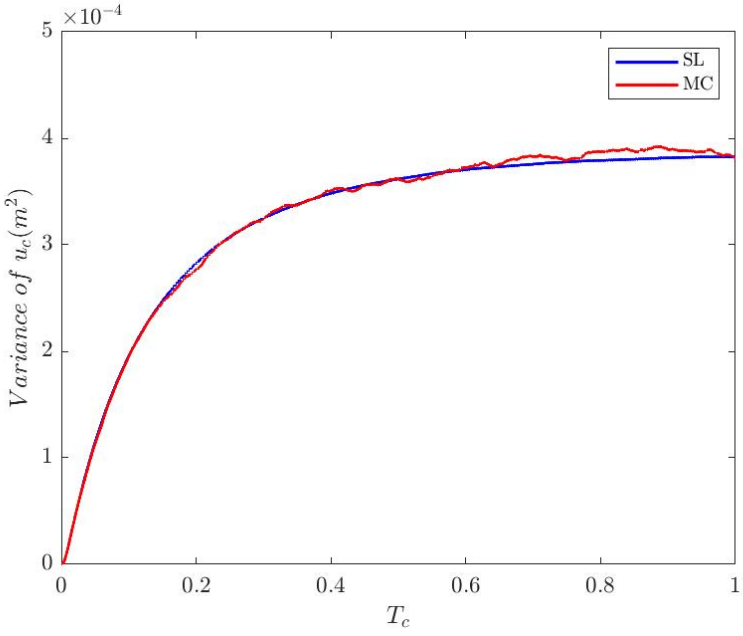

(b) Variance of displacement

Figure A.18: Displacement of carrier at θ direction